Barrier Dynamics of Nuclear Pore Complexes and Biomimetic Nanopores

Inauguraldissertation
zur
Erlangung der Würde eines Doktors der Philosophie
vorgelegt der
Philosophisch-Naturwissenschaftlichen Fakultät
der Universität Basel

von
Yusuke Sakiyama
aus Japan

Basel, 2020

Genehmigt von der Philosophisch-Naturwissenschaftlichen Fakultät
auf Antrag von

Prof. Dr. Roderick Lim
Prof. Dr. Birthe Fahrenkrog

Basel, den 26. Juni 2018

Prof. Dr. Martin Spiess
Dekan

Acknowledgements

I would like to express my appreciation to Switzerland and the Swiss Nanoscience Institute (SNI) for funding my entire PhD and the opportunities to get in touch with state-of-the-art nanoscience.

For their technical support, I appreciate all workshop and facility members at Biozentrum. To all members past and present in the Lim group including many civil service personnel and interns, I am grateful for their scientific and technical advice as well as the enjoyable time. I would like to thank Elena and RK for their support in thesis writing. Special thanks go to Lajko, Philipp, Adam and Larisa for their extensive help for writing, experiments, programming and life in general. I will learn more based on what you taught me. I would like to thank to my parents and my brother for understanding my selfishness and eagerness and always trusting me.

Finally, I am most grateful to Prof. Roderick Lim for his enormous patience and tolerance.

Abstract

Nuclear pore complexes (NPCs) mediate macromolecular traffic between the cytoplasm and the nucleus in eukaryotic cells. Tethered within each ~60 nm-diameter NPC lie numerous intrinsically disordered proteins that bear phenylalanine-glycine (FG) repeats known as FG nucleoporins (FG Nups). The FG Nups establish a selective barrier that impedes the passage of non-specific cargoes but rapidly yields to cargo-carrying transport receptors. However, the basic functional form of the FG Nups remains unresolved with respect to their spatiotemporal behaviour inside native NPCs. Here, we use high-speed atomic force microscopy (HS-AFM) to visualize nanoscopic FG Nup behaviour inside *Xenopus laevis* oocyte NPCs at near transport-relevant timescales. Our results show that the NPC channel is circumscribed by highly flexible, dynamically fluctuating FG Nups that elongate and retract in a stochastic manner consistent with the diffusive motion of tethered polypeptide chains. On this basis, extended FG Nups can momentarily interlink or coalesce into short-lived metastable condensates in the central channel, but do not cohere into a static meshwork that spans the entire pore. By resolving the time-dependent behaviour of FG Nups in the NPC, our findings bring consensus to barrier models that mainly disagree on static interpretations of how the FG Nups are spatially arranged in the pore. Furthermore, HS-AFM has been used to study the behavior of polyethylene glycol (PEG) polymer chains tethered inside of artificial nanopores. Our data shows that longer PEG chains serve are more effective in forming a barrier in pore than short PEG polymers. This serves as a strategy to design bio-mimetic nanopores with NPC-like functionality in the future.

Contents

List of Figures

List of Tables

Glossary

AD converter	Analog Digital converter
ADP	Adenosine Diphosphate
AFM	Atomic Force Microscopy
ATP	Adenosine Triphosphate
CAS	Cellular Apoptosis Susceptibility
CCC	Carrier Cargo Complex
CCD	Charge Coupled Device
CRM1	Chromosomal Maintenance 1
Cryo-ET	Cryo Electron Tomography
DNA	Deoxyribonucleic Acid
DOPC	1,2-dioleoyl-sn-glycero-3-phosphocholine
EBD	Electron Beam Deposition
EM	Electron Microscopy
FACT	Facilitates Chromatin Transcription
FD curve	Force Distance curve
FG	Phenylalanine Glycine
FRET	Fluorescence Resonance Energy Transfer
GDP	Guanosine Diphosphate
GFP	Green Fluorescence Protein
GTP	Guanosine Triphosphate
IDPs	Intrinsically Disordered Proteins
InvOLS	Inverse Optical Lever Sensitivity
HEAT	Huntingtin, elongation factor 3 (EF3), protein phosphatase 2A (PP2A) and yeast PI3-kinase TOR1
HS-AFM	High-Speed Atomic Force Microscopy
Kapβ1	Karyopherinβ1
LSB	Low Salt Buffer
Lz	Limit of Displacement
MDCK cell	Madin-Darby Canine Kidney cell
MBS	Modified Barth's Saline
mRNA	messenger Ribonucleic acid
MSD	Mean Square Displacement
NCC	Normalized Cross Correlation
NCT	Nuclear Cytoplasmic Transport
NE	Nuclear Envelope
NES	Nuclear Export Signal
NLS	Nuclear Localization Signal
NMR	Nuclear Magnetic Resonance
NPC	Nuclear Pore Complex
NTF2	Nuclear Transport Factor 2
NTR	Nuclear Transport Receptor
Nsp1	Nucleoskeletal-like protein
Nup	Nucleoporin

OmpF	Outer Membrane Protein F
PAA	Poly(acrylic acid)
PBS	Phosphate Buffered Saline
PEG	Poly(ethylene glycol)
PET	Poly(ethylene terephthalate)
PID	Proportional Integral Derivative
PLL	Poly-L-lysine
PMMA	Poly(methyl methacrylate)
PNIPAM	Poly-N-isopropylacrylamide
PVP	Poly (4-vinyl pyridine)
Ran	Ras-related Nuclear protein
Ran-GEF	Ran guanine exchange factor
RCA1	Standard set of wafer cleaning steps developed in Radio Corporation of America
RLC circuit	Resistor Inductor Capacitor circuit
RMS	Root Mean Square
RNP	Ribonucleoprotein
ROD	Reduction of Dimensionality
SEM	Scanning Electron Microscopy
SiN	Silicon Nitride
SPM	Scanning Probe Microscopy
ssDNA	Single-stranded DNA
STED	Stimulated Emission Depletion
STM	Scanning Tunneling Microscopy
TEM	Transmission Electron Microscopy
TIRFM	Total Internal Reflection Fluorescence Microscopy
Tpr	Translocated Promoter Region
UV	Ultraviolet
X.l.	*Xenopus laevis*

Chapter 1

Introduction

1 Introduction

1.1 The Nuclear Pore Complex

The nuclear envelope (NE) is composed of double lipid bilayers known as the outer nuclear membrane (ONM) and the inner nuclear membrane (INM), which separate the cytosol and nucleus [1]. Although there are several membrane proteins on the NE, the nuclear pore complex (NPC) is the primary gate for the nucleocytoplasmic traffic and regulates the bidirectional transport of macromolecules [2, 3]. For instance, mRNA can be transported only through the NPC. It is well known that several nuclear transport receptors (NTRs) are required to mediate such transport. Besides its role in mediating nucleocytoplasmic transport (NCT), the NPC is also involved in chromatin organization and the maintenance of nuclear architecture and shape together with the nuclear lamina. The focus of this thesis is the study of NPC structural dynamics in the context of NCT.

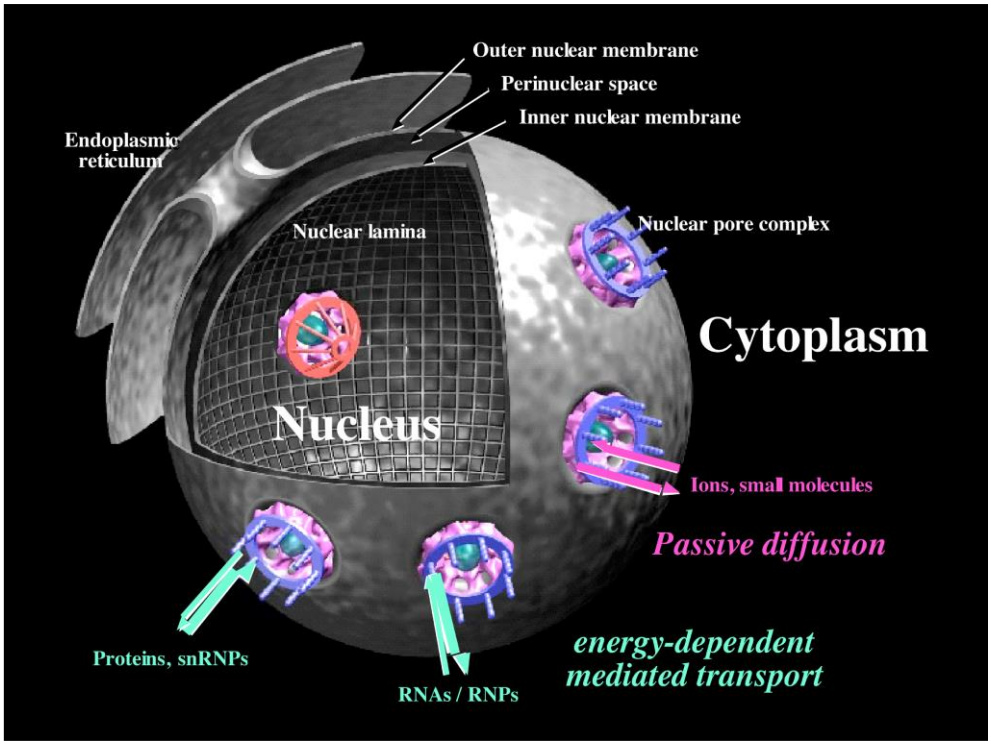

Figure 1.1: NPCs are embedded in the NE. mRNA, ribonucleoproteins (RNPs), ions, signal-specific proteins and NTRs are all transported through the NPC. The NPC is connected to the nuclear lamina network [4] [5], which shapes the nucleus. With permission from Daniel Stoffler and Ueli Aebi.

The average density of NPCs embedded in the NE depends on the species: in vertebrates it is ~10-20 pores per μm^2, in *Saccharomyces cerevisiae* (baker's yeast) nucleus ~12 pores per μm^2, in *Xenopus laevis (X.l.)* the oocyte nucleus it is unusually high with ~60 pores per μm^2

[6]. NPC density probably correlates with the NCT levels which may vary depending on the type of organism or tissue or cell type [7]. However, in the context of a large evolutionary gap, the overall architecture and structure of the NPC is conserved [8].

S. cerevisiae NPC has a molecular mass of ~66 MDa [9] and vertebrate NPC has a mass of ~125 MDa [10]. Each NPC consists of 30 different nucleoporins (Nups) that are homologous in yeast, vertebrates, and plants. It has not been possible to crystallize whole NPCs to reveal their structural elements, owing to their enormous size and the presence of several disordered proteins. Hence, crystallization studies have been limited to resolving the structure of NPC sub-complexes. These have contributed to the understanding that NPCs retain a simple fold composition and modular architecture, with the main structural motifs of Nups being alpha solenoid folds (38%), FG-repeats (29%), beta-propeller folds (16 %) and other fold types (5%) [11].

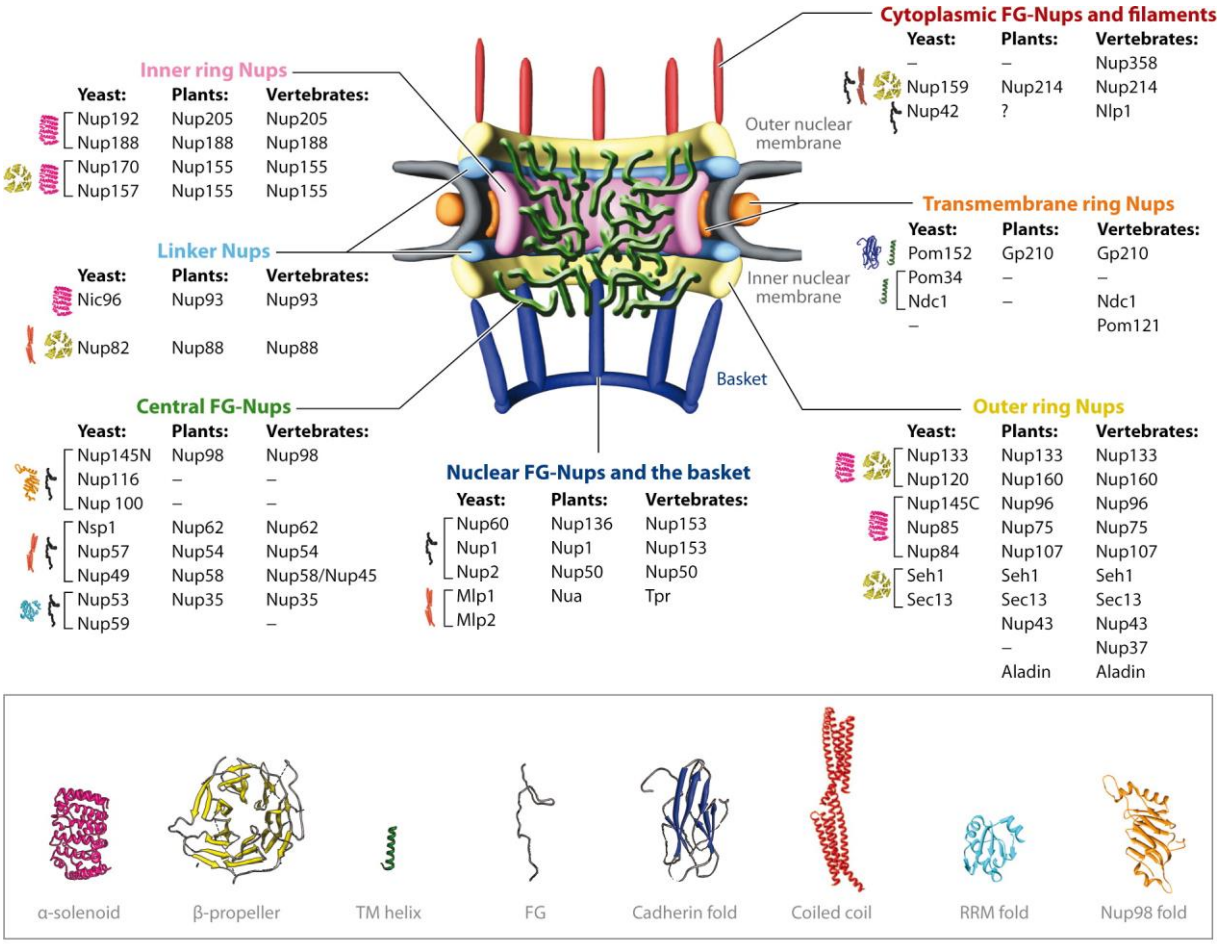

Fig. 1.2. Schematic of NPC showing transmembrane, scaffold, barrier, nucleoplasmic and cytoplasmic filaments. Channel is filled with FG Nups. Figure reproduced from Grossman *et al*. [6]

More recently, the overall NPC architecture has been characterized by cryo-electron microscopy (cryo-EM) [12, 13]. Tomographic reconstructions of the human NPC have been resolved to 23 Å using a direct electron detector [12]. Although the symmetry of its inner ring was revealed by fitting known crystal structures to tomographic reconstructions, the more flexible parts of the NPC, and in particular the intrinsically disordered FG Nups and nuclear basket, remain unresolved. Other techniques such as stimulated emission depletion (STED) microscopy [14] have also been used to resolve the eight-fold symmetry of the NPC by staining for GP210 – a transmembrane Nup - after chemical fixation. Likewise, FG Nups such as Nup214, Nup42, Nup98 and Nup153 have also been immunostained to visualize the central channel.

1.2. Structure of the NPC

1.2.1 Scaffold and Transmembrane Nucleoporins

Nups are categorized into transmembrane, scaffold, barrier, nucleoplasmic filaments and cytoplasmic filaments, based on their location and functionality within an NPC [15]. The scaffold Nups form the main NPC architecture and remain throughout the cell growth process [16]. 40 nm Y-shaped complex (Y-complex) was identified in scaffold [17]. Y-complex has two conformations; and the stem of Y-complex has two hinges, which rotate 40° [18]. Eight Y-complexes within the octagonal symmetry of the scaffold might expand the diameter of the central channel, thereby enabling large cargo such as ribonucleic proteins to pass through [19]. Pom34 and Ndc1 are transmembrane Nups with alpha-helical domains integrated into the nuclear envelope. These alpha-helices serve as anchoring points between the NPC and the NE [20]. Pom152 connects the INM and ONM and stabilize curvature of the pore membrane [3, 11].

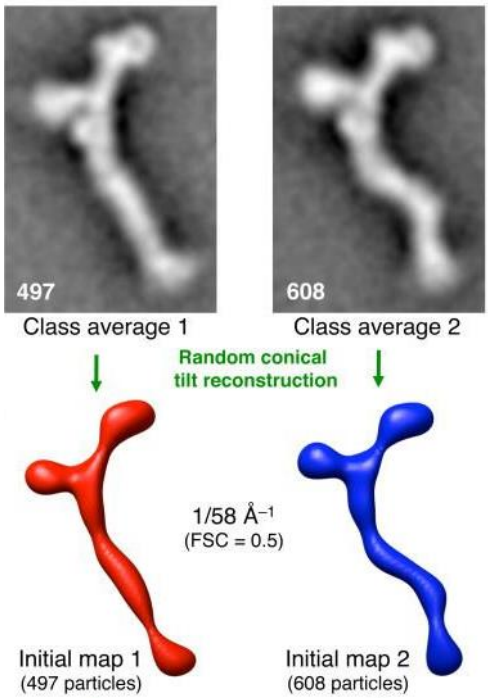

Fig. 1.3 Two conformations of Y-complex are shown by electron microscopy. The stem part has two conformations and two hinges change their angles. Eight Y-complexes form a ring in the scaffold. The scaffold expands when the step of the Y-complex is straight; the scaffold shrinks when the hinges are bent. Figure reproduced from Kampmann *et al*. [18]

1.2.2 Intrinsically Disordered Domains of FG Nups Form the NPC Transport Barrier

Barrier Nups are tethered in the central channel of the NPC and contain phenylalanine-glycine-rich domains (FG domains) that are intrinsically disordered [21]. Eleven of the 30 nucleoporins are FG Nups. Approximately 200-450 FG Nups or 3000-5000 FG repeats are present in each NPC. FG Nups occupy the central channel of the NPC and are thought to prevent the passage of large unspecific molecules [22]. FG Nups may be further categorized into four types, namely, GLFG, FxFG, PxFG or SxFG (where F is phenylalanine, G is glycine, L is leucine, P is proline, S is serine and x is any amino acid residue) [6, 21]. The central channel is mainly composed of Nup98, Nup62, Nup54, Nup58/45 and Nup35 [23]. For example, GLFG repeats of Nup98 have been located within 10 nm distance from the central axis and ~20 nm towards the cytoplasmic side of the central plane [24].

As mentioned above, FG Nups are intrinsically disordered proteins (IDPs). Generally, 10% of all proteins are fully disordered, furthermore 40% of eukaryotic proteins have at least one long (> 50 amino acids) disordered loop [25]. IDPs are involved in many important biological processes, such as the signaling, control and regulation of cellular function [26]. IDPs have a low mean hydrophobicity and a high net charge, which gives strong electrostatic repulsion

and a low propensity for compaction [27]. IDPs have some unique characteristics: fast binding kinetics, high specificity but low affinity, and multiple interaction sites [27-29]. Indeed, FG Nups share similar characteristics [27].

Nuclear transport receptors (NTRs), such as Karyopherin β1 (Kapβ1), are able to bypass the FG Nup barrier by binding to the FG-repeats, as shown by crystallography (Fig 1.4). Kapβ1 has 19 tandem 'HEAT' repeat sequences, that comprise α and β helices connected by a short turn [30-32]. Kapβ1 has multiple binding sites for FG Nups with ~10 binding pockets [33]. The interaction between single FG repeats and each Kapβ1 binding pocket (10 μs, millimolar range) has been shown by nuclear magnetic resonance (NMR) to be weak and rapid [34]. Since each FG Nup contains multiple FG repeats and NTRs have multiple binding pockets, the effective binding affinity between FG Nups and Kapβ1 is high (nano molar range). FG Nups exposed on the cytoplasmic or nucleoplasmic side of NPC are listed in Table 1.1.

Table 1.1. FG Nups and their location within the NPC [35, 36].

FG Nup	Number of FG repeats	Most abundant repeat motif	Location
hNup62	17	FxFG, FG	Central
hNup98	45	GLFG	Central
Nup358/RanBP2	21	FxFG, FG	Cytoplasmic filament
Nup153	39	FxFG, FG	Nuclear basket
Nup50	5	FG	Nuclear basket

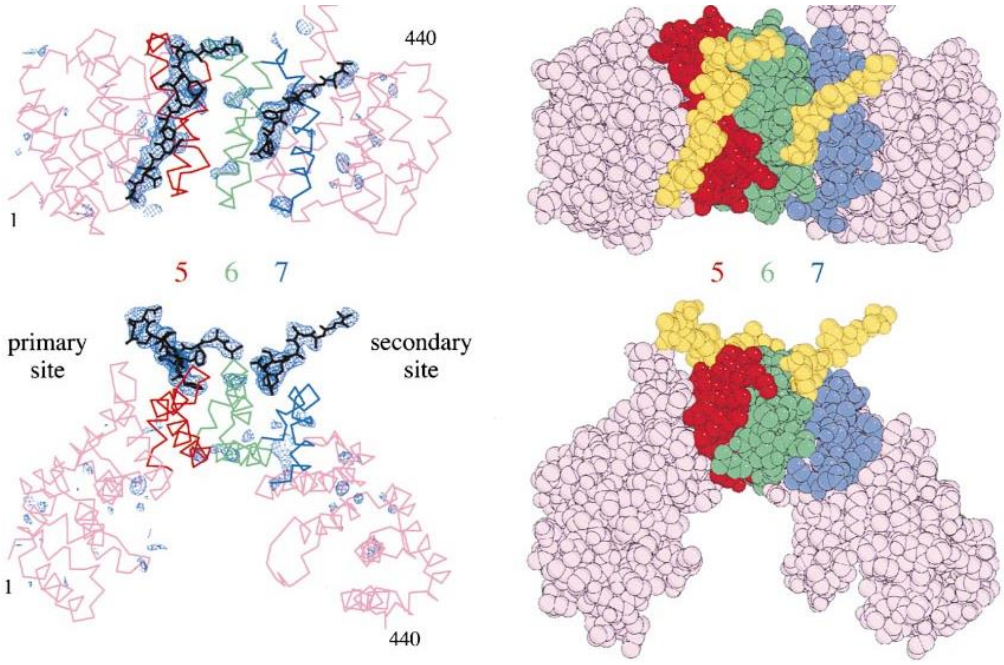

Figure 1.4: FxFG Nups bound to Kapβ1. Depicted are Kapβ1 binding pockets between HEAT repeats 5 (red), 6 (green) and 7 (blue), and FG Nups in black or yellow. Figure reproduced from Bayliss *et al*. [33].

1.2.3 Cytoplasmic Filament and Nuclear Basket

On the cytoplasmic side, cytoplasmic filaments may serve as the first docking sites for imported complexes. Additionally, they might also form final departure sites for exported mRNA [37].

The nuclear basket consists of eight spokes forming a distal ring extending into the nucleoplasm. Tpr forms the structural backbone with no FG Nups [38]. Vertebrate nuclear baskets are composed of Nup50, Nup153 and Tpr (for yeast, Nup1, Nup2, Nup60, Mlp1 and Mlp2). It is thought that Nup153 is linked at the distal ring [39]. From there, the FG domain of Nup153 could stretch from the nuclear basket to cytoplasm through the central pore [40]. In NPCs from *X.l.* oocytes, the nuclear basket is stabilized by interaction with lamina [41].

In the nuclear basket of *S. cerevisiae* NPCs, Nup2 interacts with NTRs for their efficient import [42]. In vertebrates, Tpr is involved in mRNA export, telomere organization and non-spliced RNA extension [43].

1.3. Nucleocytoplasmic Transport

Solutes or small molecules of less than 5 nm (or 40 kDa) diffuse freely through the NPC, but macromolecules larger than ca. 40 kDa require NTRs to translocate through the NPC. The

transport dwell time of Kapβ1 in the NPC is approximately 5 ms [44]. Unlike myosin driven by ATP hydrolysis, the passage of NTRs through the NPC is facilitated by Brownian motion [20]. However, the NTR transport through the NPC is 30 times faster than passive diffusion of similar unspecific molecules, such as is the case for Ran-GDP that is carried from the cytoplasm to nucleus by nuclear transport factor2 (NTF2) [45]. Such active transport of cargo molecules requires a high Ran-GTP concentration in the nucleus, which binds NTRs to release import cargoes in the nucleus. The Ran guanine nucleotide exchange factor (Ran-GEF) facilitates the exchange of GDP to GTP in the nucleus. Ran-GTP then returns to the cytoplasm in the complex with Kapβ1 or other exportins like CRM1 or CAS [46, 47]. Ran-GTP activating protein (Ran-GAP) located on the cytoplasmic filaments hydrolyzes Ran-GTP to Ran-GDP on the cytoplasmic side [48-50]. This leads to a high Ran-GTP concentration in the nucleus and Ran-GDP in cytoplasm. The cargo-complex will be rapidly dissociated by Ran-GTP at the nuclear side of the NPC and the NLS-cargo will not be able to return as quickly to the cytoplasm [51-53]. Additionally, Nup50 can also facilitate the NLS-cargo and Kapα release from the import complexes upon Ran-GTP binding to Kapβ1 [54].

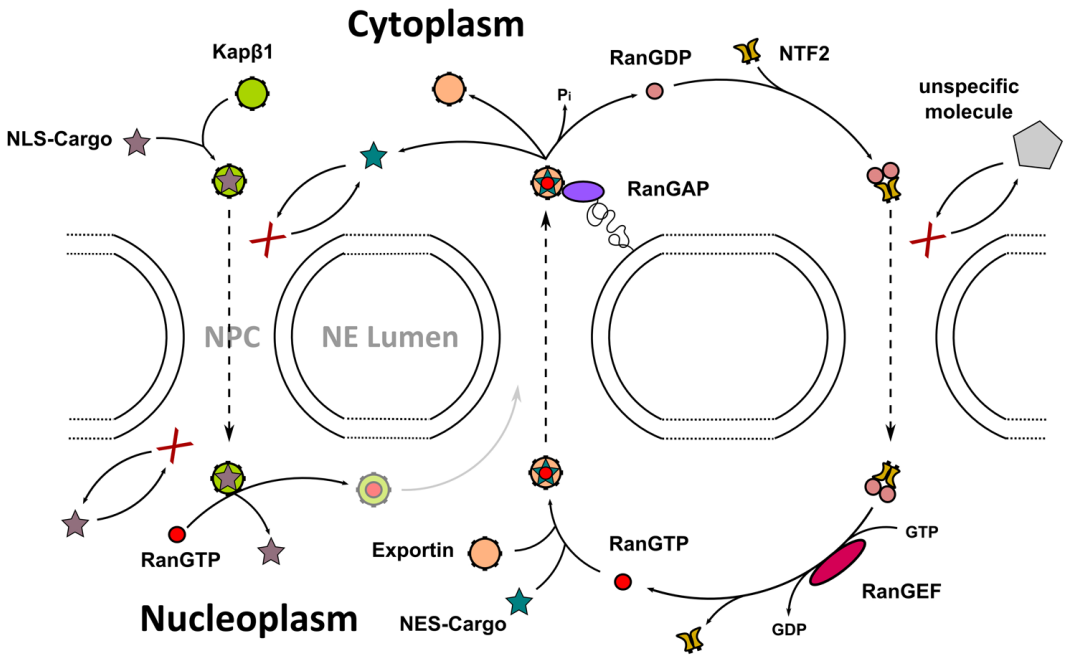

Fig. 1.5. Schematic of nucleocytoplasmic transport. Import complex made of Kapβ1 and NLS-cargo is transported from cytoplasm to nucleoplasm. NES-cargo complex with Ran-GTP and exportin is exported from nucleoplasm to cytoplasm. Reproduced from Fuxreiter *et al.* [55].

1.3.1 Transport Models

Approximately 100 MDa or 1000 molecules are translocated through each single NPC per second [56]. This is puzzling based on specific binding between NTRs and the FG nups, as

this should result in slower transport. Several models have been proposed to describe the role of the NPC in regulating such NCT, including the 'selective phase model', 'virtual gate' and 'polymer brush' models, 'reduction of dimensionality' (ROD), 'forest and trees' model and 'Kap-centric control'. These are summarized in Fig. 1.6. A short textual overview of these models is given below.

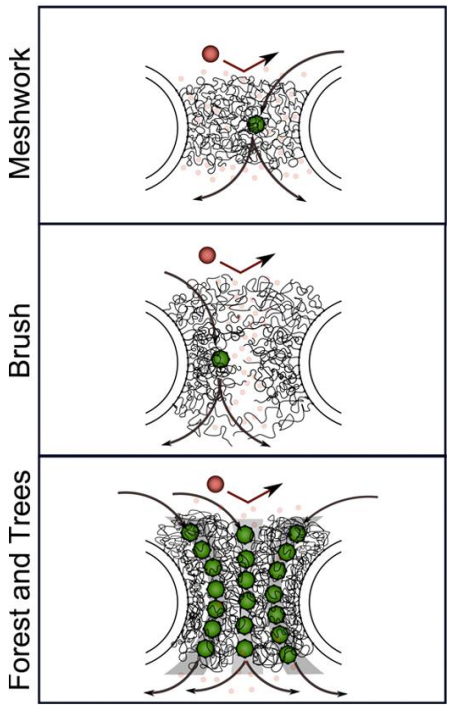

Fig 1.6 "FG-centric" models are listed from top to bottom 'selective phase model', 'virtual gating model', and 'forest and tree model' respectively. These models describe how tethered FG Nups may form and behave in the channel to regulate NTRs. The green balls represent NTRs and the brushes represent FG Nups. Reproduced from Fuxereiter *et al*. [55]

1.3.2 The Selective Phase Model

The selective phase model was proposed by Görlich *et al.* [56]. This model is also called the hydrogel model given that the FG Nups can be made to form macroscopic hydrogels [57]. In this model, it is suggested that FG Nups form a sieve-like meshwork which small molecules can permeate freely but which excludes larger molecules. However, NTRs can compete for binding with FG repeats and as such can translocate through the NPC with or without specific cargo by 'melting' this meshwork or widening it. It was shown experimentally that the FG-FG interactions are crucial for the hydrogel formation, because wild type Nsp1 was able to form hydrogel with much higher viscosity than its F-S mutant [57]. Transport assays mimic Kapβ1 translocation through the real NPC by transporting 1000 times faster than similar-sized molecules [58]. However, Milles *et al*. demonstrated, using scanning and transmission

electron microscopy, that at the nanoscopic level these hydrogels are constructed from amyloid-like fibers with holes of several tens of nanometers in diameter that resemble the size of the NPC central channel [59].

1.3.3 Virtual Gating and the Polymer Brush Model

The virtual gating model was proposed by Rout *et al*. [20]. FG Nups form an entropic barrier that prevents unspecific large cargoes from entering the pore. Such a virtual gate may be built by the dynamic motion of FG Nups. Here, the rapid motion of the FG Nups promotes the consecutive 'handing over' of individual NTRs to the next FG Nup inside the channel, hence accelerating NTR translocation. In other words, the pore is apparently closed for non-binding molecules but is open for the FG binding proteins. However, this model is not beyond hypothesis based on molecule kinetics. Experimental evidence of the fast binding and release rate between FG Nups and Kapβ1 was missing [60].

The polymer brush model proposed by Lim *et al.* [61] serves as experimental evidence to support the virtual gating model. In this, Nup153 was densely tethered to gold nanostructures and force spectroscopy was used to measure the collective repulsive forces emanating from the FG Nups. Although the hydrodynamic radius of Nup153 is 5.1 nm ± 3.2 nm, AFM cantilever detected repulsion ~40 nm above the gold nanostructures. This shows that FG Nups can extend when they are densely tethered.

Moreover, compaction of Nup153 with the addition of Kapβ1 and re-extension in the presence of RanGTP were also shown by AFM [62]. In the same study, FG Nup compaction and re-extension were also demonstrated by immunogold-labelling Nup153 in *X.l.* NPCs *in situ*. This shows the Ran-dependent activity of Nup153.

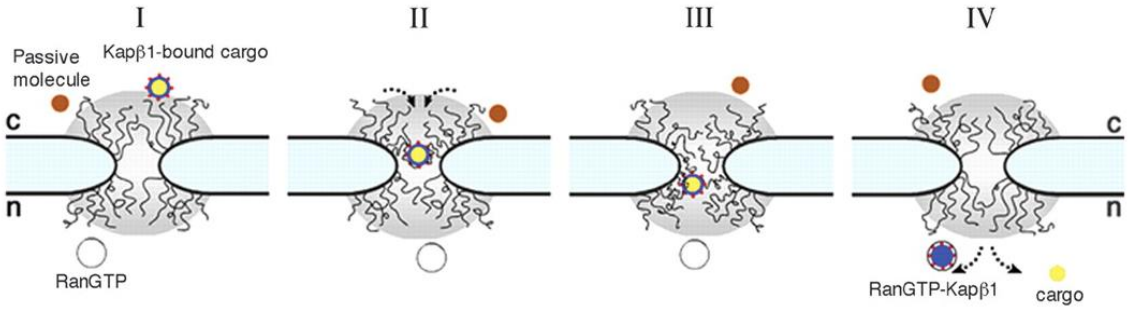

Fig 1.7 Cartoon to illustrate polymer brush model. Gray zone shows range of entropic barriers made of FG Nups. I, II, II shows FG Nups repel a passive molecule but Kapβ1-bound cargo can permeate. IV, Ran-GTP dissolves the cargo and Kapβ1 and FG Nups becomes free again. Reproduced from Lim *et al*. [62]

1.3.4 The Reduction of Dimensionality Model

The reduction of dimensionality model (ROD) was proposed by Peters *et al.* [63]. Inside a cell, the concentration of NTRs is fairly high (~10 μM Kapβ1), and FG repeats are most likely occupied by NTRs; thus FG Nups are bound by NTRs forming collapsed layers along the channel. On the other hand, free NTRs rapidly traverse the pore and exit. FG binding NTRs follow two-dimensional diffusion along the wall, while free NTRs diffuse three-dimensionally in the central area of the pore. Bound NTRs can penetrate and move laterally within the collapsed FG Nup layer owing to their hydrophobic, multivalent interactions with FG Nups. It was shown experimentally that the mobility of Kapβ1 on the FG layer increases at high concentrations of Kapβ1 and becomes less mobile at low Kapβ1 concentrations [64].

1.3.5 The Forest and Tree Model

The forest model was proposed by Yamada *et al.* [65]. This model is basically a combination of the three models discussed above. Yeast NPCs have more hydrophobic FG Nups than their vertebrate counterparts, allowing yeast FG Nups to form tight globules which are low in charge. Highly charged domains are extended and dynamic. For instance, in Nsp1 the N terminus has low charged amino acid residues (2%) and the FG domain has 36% of highly charged amino acid residues. Taken together, one side of the grafted Nsp1 has a compact globule on top and extended features in between. These features resemble trees. Inside the NPCs, densely populated low charged tight globules make stable inner and outer rings (Figure 1.8). The area between these two rings is dominated by extended and dynamic FG Nups. These areas are called zone 1, which is situated inside the inner ring, and zone 2, which is situated between the inner and outer rings. Both zones correspond to the transport paths although large cargoes can only go through zone 1. This static ring is predicted to be the same structure reported as ‘transporter’ or ‘central plug’, as seen by cryo-electron tomography [66] or negative stained transmission electron microscopy of the NPC of *X.l.* oocytes [67].

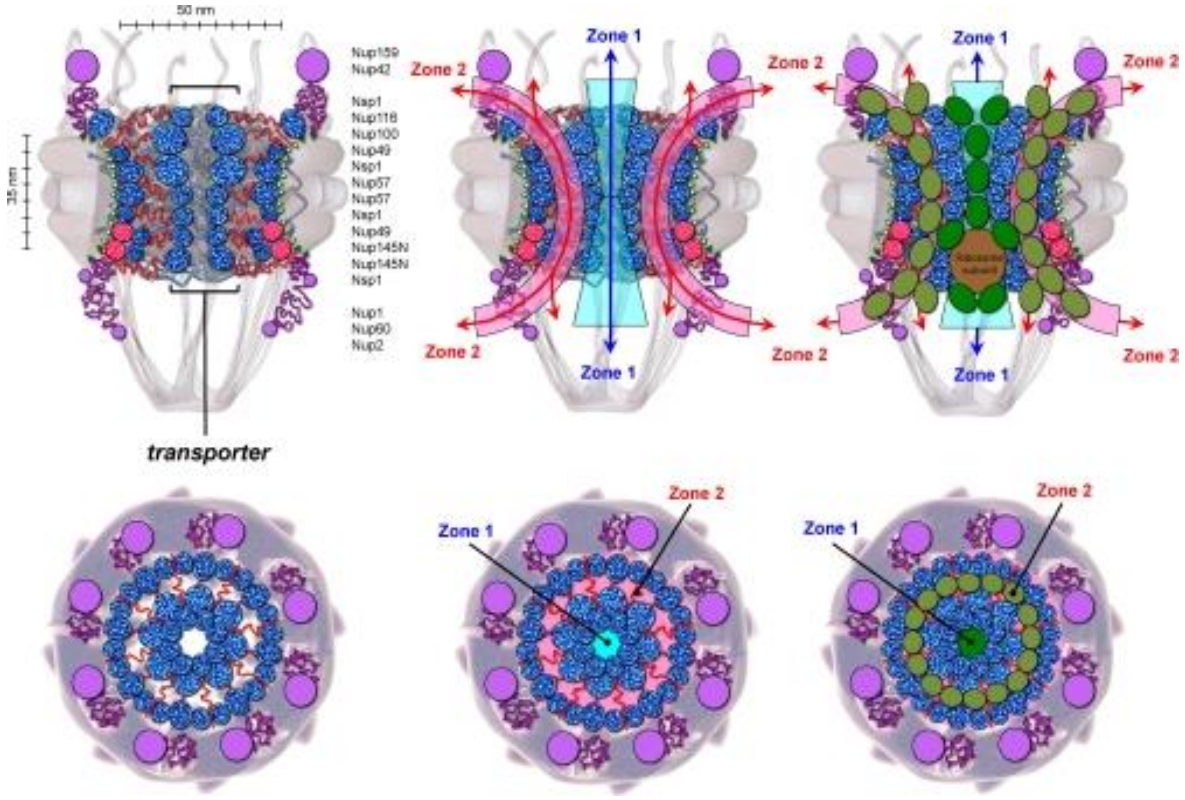

Fig 1.8, The forest/tree model. This model is based on the intrinsic characteristics of yeast FG Nups. Blue indicates the cohesive blobs of FG Nups and red chains indicate non-cohesive FG domains. Dark and light green show the path of Kaps. Reproduced from Yamada *et al*. [65]

1.3.6 The Kap-centric Model

In the Kap-centric control model it is suggested that the NPC central channel is not only occupied by FG Nups, but also crowded with NTRs [68]. This statement is based on the fact that Kapβ1 binds strongly to FG Nups (K_D < 1 μM) and therefore at the physiological Kap concentration (> 3 μM) it would lead to high Kap-occupancy in the NPC transport channel. At high concentration, the binding avidity of Kaps decreases (K_D > 10 μM) owing to reduced FG repeats available for binding within the crowded FG Nup layer. Similar conformational changes of the Kap-FG layer have also been observed in the NPCs of HeLa cells [44, 69]. Hence, it is postulated that Kap crowding in the central channel and reduction in the Kap binding avidity would facilitate rapid transport of the cargo-Kap complexes through the NPC. In fact, Kap depletion from the NPC also leads to the loss of NPC barrier selectivity and an increase in unspecific cargo leakage [70]. Therefore, this model considers Kaps as integral constituents of the NPC selective barrier which regulate its selectivity and permeability.

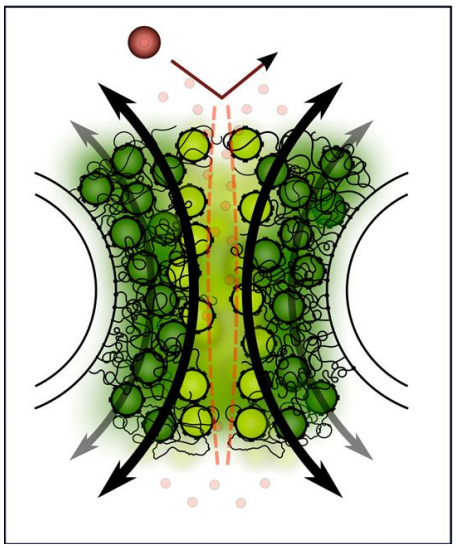

Fig 1.9 Kap-centric model. Dark green represents strongly bound Kapβ ($K_D \approx 10^{-7}$ M) and light green represents weakly bound Kapβ1. Weakly bound Kapβ1 translocates faster than strongly bound Kapβ1 ($K_D \approx 10^{-5}$ M). Channel is occupied by Kaps. Reproduced from Kapinos *et al*. [68]

1.4 Molecular Dynamics Simulation of Central Barrier

Molecular dynamics (MD) simulations are used extensively to shed light on the transport mechanism. The key question addressed by MD simulation is how the FG Nups assemble in a channel. Simulation was conducted over a time scale of micro seconds to determine how FG Nups stretch out and form rapid bundles of 2-6 FG Nups [71]. The FG Nups coil up into a globular structure to protect the hydrophobic region of FG Nups from being exposed to the aqueous environment. The dynamics of Nsp1 in three different initial states were studied. The states are as follows: (a) tethered, straight-chain conformations in a ring-like arrangement; (b) tethered, random-chain conformations in an array-like arrangement; and (c) untethered, random-chain conformations – simulating each system for 1 microsecond. All cases led to the formation of brush-like bundles linked by single Nsp1-FGs that cross in between the bundles. Interestingly, the frequency of crossings between bundles and the bundle thickness depend on the protein length, the geometry of the simulated volume, the degree of tethering and the initial conformations of Nsp1-FGs. Simulations of the NPC central channel suggest that near the periphery of the channel (where the tethering of Nups is dominant), the brush-like structure has just a few cross-linked bundles, but in the central region (where tethering loses its effect) there are more bundles with sieve-like structures with frequent cross-links. Hence, the FG repeats in these cross-linked regions allow more binding of NTRs to assist in cargo translocation [72, 73].

1.5 Aim of the Thesis

Previous efforts in the lab have strived to reconcile molecular kinetics and mechanics to improve our understanding of the NPC selectivity barrier [61, 62, 64, 68, 74, 75]. Mechanical changes in FG Nups stimulated by Kaps are experimentally demonstrated in *in vitro* experiments. However, these studies lack key elements: spatial confinement, temporal resolution and a nanoscopic view of individual molecules. Therefore, my thesis is aimed at studying FG Nup dynamics inside NPCs. Notably, this is the first time that FG Nup dynamics have been resolved inside native NPCs. Previously, Kramer *et al.* revealed by means of AFM and phase image, static features resembling hydrophobic meshwork in native NPCs [76]. Ma *et al*. demonstrate the localization of FG Nups and Kaps during translocation by single-point edge-excitation subdiffraction microscopy (SPEED) [44, 77]. Still, fluorescent-based approaches have limited resolution and can only show the fluorescent markers. Moreover, individual structural dynamics were not shown and, hence, the overall location of FG Nups and NTRs remains unanswered. Bestembayeva *et al.* also used AFM to resolve the nanomechanical stiffness of the permeability barrier within the NPC channel [78].

The objective of this thesis is to implement high-speed (HS)-AFM in order to resolve the dynamic behavior of the FG Nups in native NPCs. In Chapter 2, HS-AFM is introduced in order to understand its mechanism and its advantage over conventional AFM. Chapter 3 explains the application of HS-AFM to native NPCs as obtained from *Xenopus laevis* oocyte nuclei. Chapter 4 presents HS-AFM work to characterize biomimetic NPCs by tethering (i) Nup62 to gold nanorings and (ii) PEG to nano caves. Polymer dynamics in artificial systems are also shown which demonstrate barrier-like behavior. In the Outlook section, I explain how the lateral dynamics of FG Nups on a planar surface are studied by HS-AFM.

Chapter 2

High-Speed Atomic Force Microscopy

2.1 Atomic Force Microscopy

2.1.1 Basic Principle

Scanning probe microscopy (SPM) involves the use of a microscope composed of a stage, a probe, and a detector to investigate the surface of materials. Atomic force microscopy (AFM) and scanning tunneling microscopy (STM) are the two well-known SPMs. STM was developed in 1981 prior to AFM, and a good resolution is considered to be around 0.1 Å in Z axis and 1 Å in X-Y axis [79]. STM can only be used to study conductive materials, and cannot be used in electrolytic solutions because it uses a tunneling current through a potential barrier. On the other hand, AFM, which was invented in 1986, is more advantageous since it can be used in various environments, viz. in vacuums, air and solutions [80]. An AFM probe traces the surface of the material in three modes: contact, non-contact and tapping modes. Contact mode AFM, which was the first to be developed, was used mainly to investigate the surfaces of hard materials. During experiments employing contact mode AFM, the sample surface is scratched or distorted by the dragging force of the cantilever. This lateral force becomes especially high when the materials are topographically rough. To minimize the cantilever force, the height of the sample stage is adjusted to ensure that the difference between the expected cantilever deflection (set point) and read-out deflection is equal to zero. To further reduce the lateral force issue, tapping mode AFM was developed. In this mode, contact is limited to the tip end and sample because the tip oscillates vertically. Nowadays, tapping mode is the most frequently used method for bio-imaging.

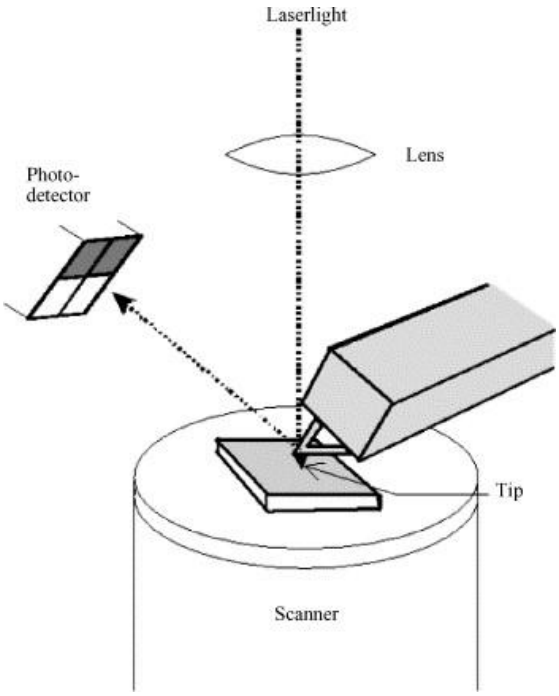

Fig 2.1: Illustration of AFM. The cantilever position is detected by a photo detector and a feedback loop control moves the piezo scanner vertically to keep the same distance between tip and sample. Figure reproduced from Butt *et al.* [81]

2.1.2 Force Distance Curve

As the name atomic force microscopy suggests, one of the main functions of AFM is the measurement of force. The force applied is calculated from the cantilever deflection as detected by the laser. Thus, force is calculated as

$$F = k_c ((V-V_0)\ \Omega^{-1}) \qquad (2.1)$$

where k_c, V and Ω are the spring constant, voltage detected by photodiode, and photodiode sensitivity, respectively. V_0 is the setpoint of voltage. Tip sample distance depends on piezo electric displacement Z, thus the tip-sample distance D is

$$D = (Z-Z_0) - (V - V_0)\Omega^{-1} \qquad (2.2)$$

These equations are described in Butt *et al*. [81]. A force curve is used to calibrate the cantilever deflection and piezo driving voltage. From the gradient indicated in Fig 2.2, inverse optical lever sensitivity (InvOLS) is calculated as 42.5 nm/V.

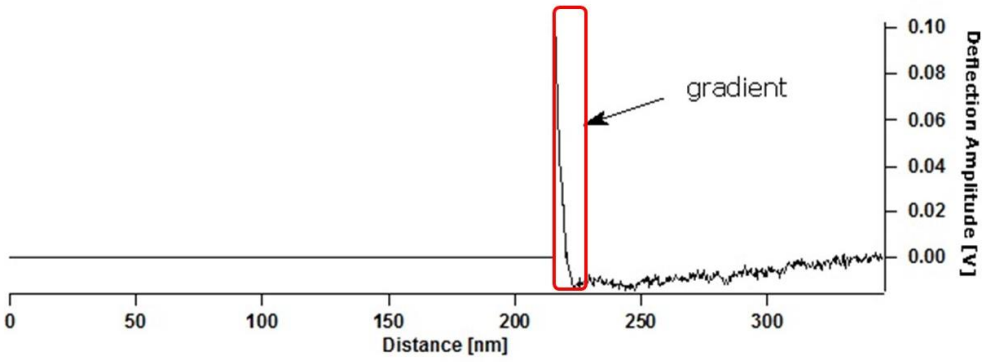

Fig 2.2: Force distance curve measured by AFM is highlighted by red circle. Oscillation sensitivity is 42.5 nm/V.

2.1.3 Application of the Force Distance Curve

AFM can detect sub-picoNewton forces and hence is used for molecular recognition events by measuring the force between ligands and receptors [82]; quantifying cell adhesion forces at the molecular level [83]; measuring single molecules binding to a target nucleic acid [84]; and mapping the distribution of cell-surface receptors etc. [85-88]. In the recent years, AFM has been explored to develop force distance (FD) curve imaging maps. FD curve imaging needs to measure forces at each pixel, which results in several thousands of FD curves required per image [89, 90]. Recently, FD curve AFM recorded 512 x 512 pixels, the resolution of which was close to 1 nm, but with a comparably slow frame rate of 15-30 min [89]. Each FD curve

quantifies physical properties such as elasticity and adhesion. AFM has also been used for measuring the mechanical responses of cells under different loading rates and obtaining stiffness measurements of cells or tissues [91-93].

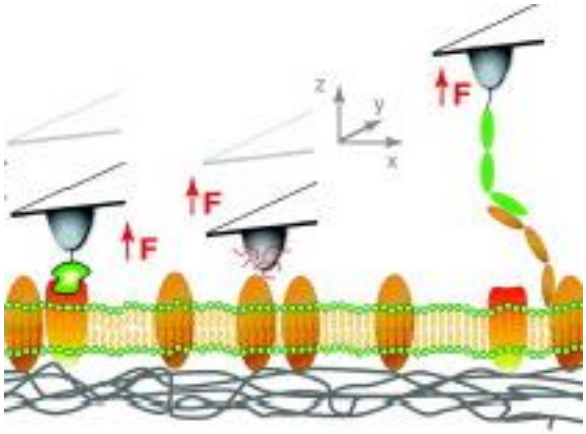

Fig 2.3: Schematic of FD curve recognition. Cantilever tip can be chemically (middle) or biologically (right) functionalized. Figure reproduced from Müller *et al*. [88]

2.2 High Speed Atomic Force Microscopy (HS-AFM)

2.2.1 Biological Process Imaging and Evolution of HS-AFM

In this section, I explain the historical background to the imaging of biological processes by means of HS-AFM, using myosin V as an example.

Historically, myosin V has been studied by electron microscopy, fluorescence imaging, X-ray crystallography and many biophysical and biochemical techniques, revealing various mechanisms of protein function. Myosin V is a motor protein that walks on actin filaments towards the barbed end (+ve end where the actin monomers are added) using ATP hydrolysis as the driving force. Its walking mechanism was an active topic of research in 1990s, which revealed sub fragment crystal structures of pre-stroke and post-stroke conformations [94-97]. These two conformations were also demonstrated by fluorescence resonance energy transfer (FRET) measurements [98]. Single-molecule fluorescence polarization provided evidence that myosin V walks on actin filament in a ‘hand-over-hand’ movement rather than an inchworm movement where one foot always leads [99]. Through the use of optical tweezers, it was shown that myosin V has a step size of ~36 nm which is the same as one helix of actin filaments. The release of the myosin V trailing head from actin is caused by ATP binding, which follows the release of bound-ADP [100, 101]. Snapshots of each walking behavior were captured by electron microscopy. Stretched and curved conformation of the leading head, and the detachment of the trailing head were seen in EM images [102]. While the

combination of these techniques provided insight into the walking behavior of myosin, none of these techniques provided direct visualization of the dynamics of this process.

Around the same period, AFM gained popularity for visualizing biological processes because of its applicability in solution and having a nanometer scale resolution. Indeed, the Hansma research group used contact mode AFM to visualize the polymerization of fibrin molecules to form a fibrin blood clot [103]. Tapping mode was also used to capture snapshots of RNA polymerase transcribing double-stranded DNA [104]. However, the scanning rate of conventional AFM is too low to capture dynamic processes. The Ando group in Kanazawa finally developed a high-speed-AFM (HS-AFM), which exhibits a fast scan rate and low sample disturbance, and hence can be used to record biological processes in space and time[105, 106].

Wiggling myosin V on mica surfaces was first captured at 80 ms/frame in 2001 and walking myosin V molecules on actin filaments were observed in 2010 [105, 107]. These HS-AFM images showed the hand-over-hand walking behavior as well as the trailing-head detachment caused by ADP to ATP exchange. This seminal study proved that HS-AFM is a powerful technique that allows for the direct visualization of protein dynamics. Since then, HS-AFM has revealed many protein dynamics.

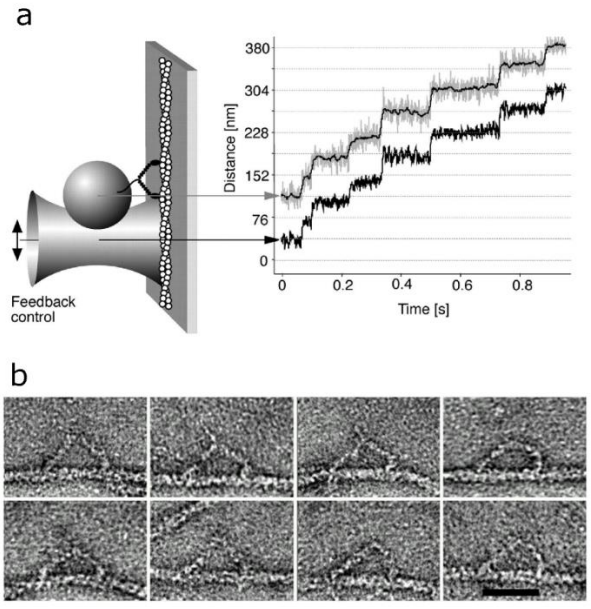

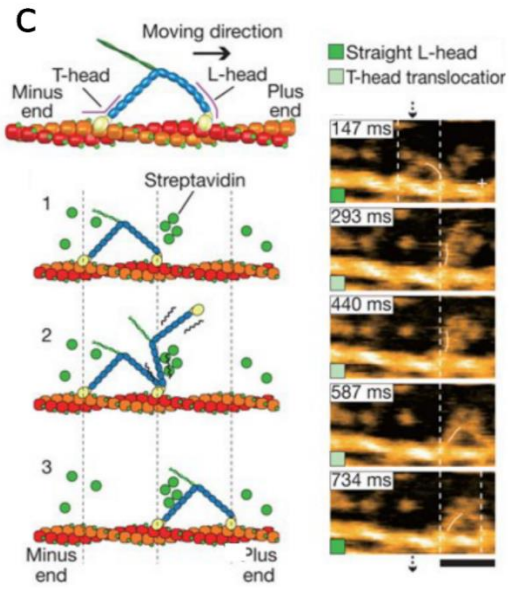

Fig 2.4: (a) Myosin V walking steps were shown by optical tweezer. Step size ≈ 36 nm. Figure reproduced from Rief *et al.* [100] (b) Snapshots of walking myosin V on an actin filament revealed by EM. Scale bar, 36 nm. Figure reproduced from Walker *et al.* [102] (c) HS-AFM images of walking myosin V on actin filament. Scale bar, 30 nm. Figure reproduced from Kodera *et al.* [107]

2.2.2 Technical Features of HS-AFM

In this section, I explain the technical features that allow for the high frame rate of HS-AFM.

2.2.2.1 Mechanics of the Cantilever

The cantilever, usually made of either silicon nitride or nanocrystal silicon, is the main factor that minimizes mechanical damage to a sample. Silicon nitride is used for soft cantilevers (spring constant: 6–400 pN/nm) and single crystal silicon is used for stiff cantilevers (spring constant: 1,000–70,000 pN/nm) [108]. Soft cantilevers are mainly used for protein observation. Here I describe the mechanical properties of a cantilever. Young's modulus, a measure of the stiffness of solid material, is given by

$$E = F/A \cdot (\Delta L/L_0)^{-1} \qquad (2.3)$$

where F, A, ΔL and L_0, are the force exerted on an object under tension, the area of the cross-section perpendicular to the applied force, the length changes, and the original length, respectively. Spring constant k_c and resonance frequency f_c in aqueous solution are given by the following formulas

$$k_c = Ewd^3/4L^3 \qquad (2.4)$$

$$f_c = 0.56\, d/L^2\, (E/12\rho)^{1/2} \qquad (2.5)$$

where L refers to length, w to width, d to thickness, E to Young's modulus and ρ to density of cantilever material. As seen from equations (2.4) and (2.5), a high resonance frequency and a

small spring constant are contradictory features: the longer and thinner the cantilever, the smaller both the spring constant and the resonance frequency become. Ultra-short and thin silicon nitride cantilevers are presumably the only possible combination to achieve a high resonance frequency and small spring constant simultaneously. Indeed, with a length of 9 μm, a width of 1 μm and a thickness of 140 nm, a silicon nitride cantilever (Olympus) has 1.5 MHz (air), 600 kHz (liquid) resonance frequency and a spring constant of 200 pN/nm (Fig 2.5 a, b). The spring constant can also be expressed as

$$k_c = k_B\, T / \langle x^2 \rangle \qquad (2.6)$$

where $\langle x^2 \rangle$, k_B and T are the mean square of deflection, Boltzmann constant and temperature, respectively. Maximum tapping force is expressed as

$$F_{max} = (k_c/Q_c) \times [A_0\,(1\text{-}r) + h_0 \sin(\theta/2)] \qquad (2.7)$$

where Q_c, A_0, r, h_0, θ are the quality factor in water, the free amplitude of oscillation, the reducing ratio of amplitude after tapping, the sample height and the phase shift, respectively [109]. Under conditions of Qc = 2, A_0 = 1 nm, r = 0.8-0.9, h_0 = 5 nm and θ = 20°, F_{max} is ≈100 pN. The mechanical energy of the cantilever is ≈ 24 k_BT where k_BT is 4.114 x 10^{-21} Nm. This amount is comparable to ATP hydrolysis ≈ 20 k_BT. The estimated energy loss for each tap is 2.3-4.4 k_BT [109].

At the free end of the cantilever, an electron beam deposition (EBD) tip is fabricated using phenol or ferrocine gas. Since the tip radius directly influences the image resolution, plasma etching is used to further sharpen the EBD tip [110].

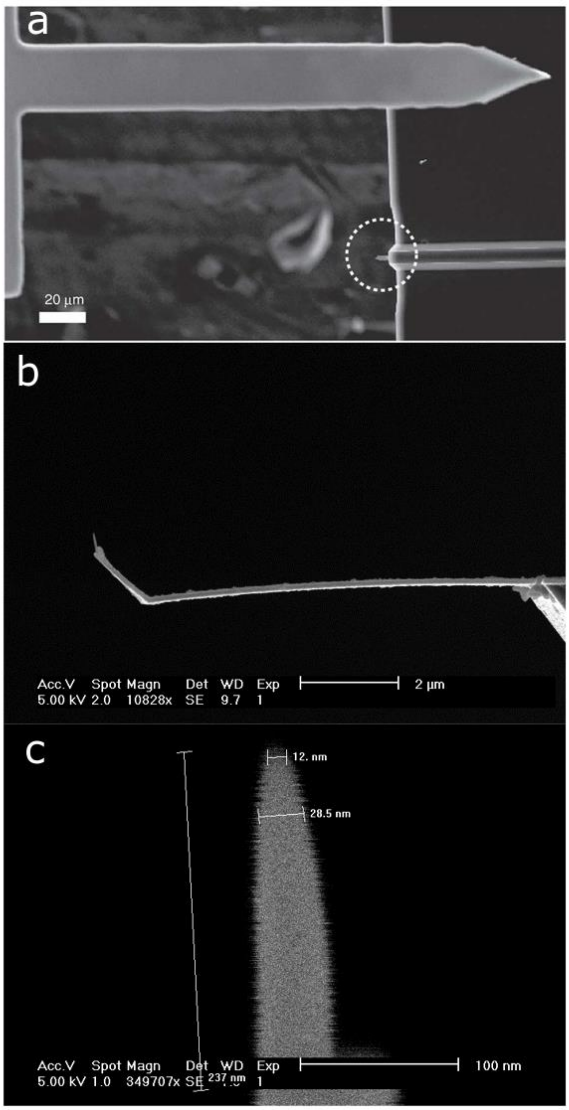

Fig 2.5: SEM image of a cantilever and an EBD tip. (a) Conventional AFM cantilever and HS-AFM cantilever. The HS-AFM cantilever is encircled by a broken line. Figure reproduced from Uchihashi *et al*.[110] (b) Side view of an SEM image of a HS-AFM cantilever (c) Magnified image of EBD tip. R_{tip} is estimated to be ≈ 6 nm.

2.2.2.2 Electronics of HS-AFM

So far, I have introduced the mechanical design of HS-AFM which is intuitively understandable. In this section, I introduce the electronics needed to enable video rate recording. There are three key elements: amplitude detection, active damping, and a dynamic PID controller.

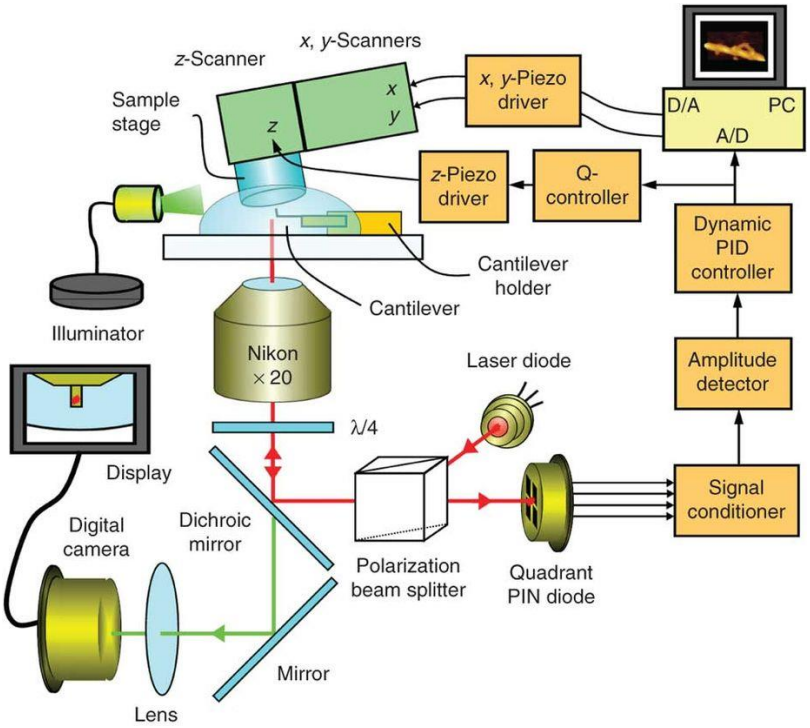

Fig 2.6: Schematic of HS-AFM. Amplitude detector, a dynamic PID controller and a Q-controller are three unique features of HS-AFM compared to conventional AFM. Figure reproduced from Uchihashi *et al.* [110]

Amplitude Measurement

When the cantilever is excited by a resonance frequency f_c ($=\omega/2\pi$), z axis displacement is

$$z_c = (A_0 - \varepsilon)\sin\omega_c t - 1/2(\cos(\omega_c-\omega)t + \cos(\omega_c-\omega)t) \quad (2.8)$$

ε, t, ω, ω_c, are the sample viscosity, time, the phase after contact to surface and the phase of the free oscillation, respectively. $A_0\sin\omega_c t$ is the free oscillation amplitude and $-\varepsilon\sin\omega_c t - 1/2\varepsilon(\cos(\omega_c-\omega)t + \cos(\omega_c-\omega)t)$ is the amplitude after contact to a surface.

For high-speed scans, a megahertz frequency needs to be detected in each cycle but the RMS of DC converters requires several cycles to measure the RMS values. For HS-AFM, the peak-hold method is used to detect amplitude [105]. A sinusoidal wave is split into two where one is shifted 90° by a phase shifter. Afterwards, timing signals are produced at the peak (V_{+p}) and bottom (V_{-p}) of the sinusoidal wave. Sample/hold circuits hold the other split sinusoidal wave, V_{+p} and V_{-p} output when timing signals arrive. The difference between V_{+p} and V_{-p} is calculated as the amplitude. The peak-hold method therefore detects the amplitude in a half cycle and can be extremely accurate even if phase or frequency are changed.

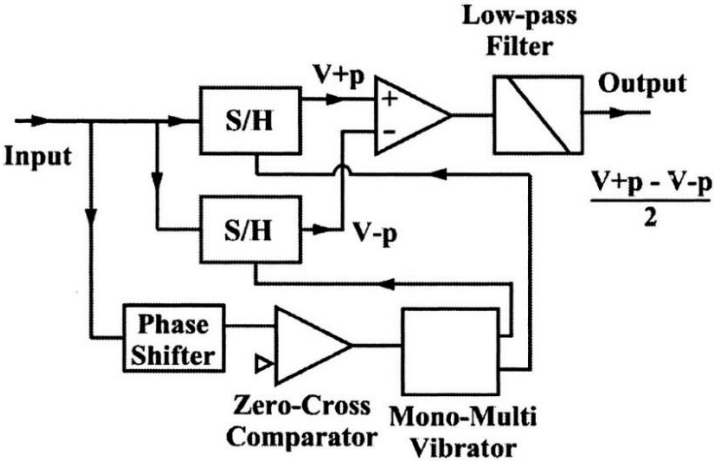

Fig 2.7: Circuit to measure fast amplitude by analog circuit. Figure reproduced from Ando *et al*. [105]

Nowadays, the Fourier method is used instead of the peak-hold method. A signal passes through an AD convertor, the Fourier amplitude method, and a DA convertor. Cantilever oscillations are expressed as

$$A_{sin}(t) = \omega(t)/\pi \int^{2\pi/\omega(t)}_0 d(t-\tau)\, \sin(u(t-\tau))d\tau \quad (2.9a)$$

$$A_{cos}(t) = \omega(t)/\pi \int^{2\pi/\omega(t)}_0 d(t-\tau)\, \cos(u(t-\tau))d\tau \quad (2.9b)$$

Amplitude is given by using $A_{sin}(t)$ and $A_{cos}(t)$,

$$A(t) = [A^2_{sin}(t) + A^2_{cos}(t)]^{1/2} \quad (2.10)$$

Using the Fourier method, maximum bandwidth is $f_c/8$, which is twice as high as the peak-hold method [111].

Active Damping

Since undesirable noise prevents smooth imaging for high-speed scanning, there needs to be an oscillation damping mechanism. Piezo actuators and cantilevers have quality factors with high peaks of mechanical vibration. A Q controller is used to compensate the Q-peak of the z scanner and cantilever electronically. Using the second-order transfer function, the mechanical response of the actuator is expressed by

$$G(s) = K\omega_p^2\, [s^2 + (\omega_p/Q_p)s + \omega_p^2]^{1/2} \quad (2.11)$$

where $\omega_p = 2\pi f_p$, Q_p, K and s are the resonance frequency, the quality factor of piezo, the ratio of displacement to voltage applied to piezo and the discrete time, respectively. From equation (2.11), response is distinctive in resonance frequency, thus a mock actuator is used to dampen the Q-peak [112]. An RLC circuit, which has $(LC)^{-1/2}=\omega_p$ and $(LR^{-2}C^{-1})^{1/2}=Q_p$, is used as the mock actuator. Q_p and ω_p are adjusted by using appropriate capacitors and resistors. After mock damping, the Q-peak disappears (Fig 2.8, broken line c).

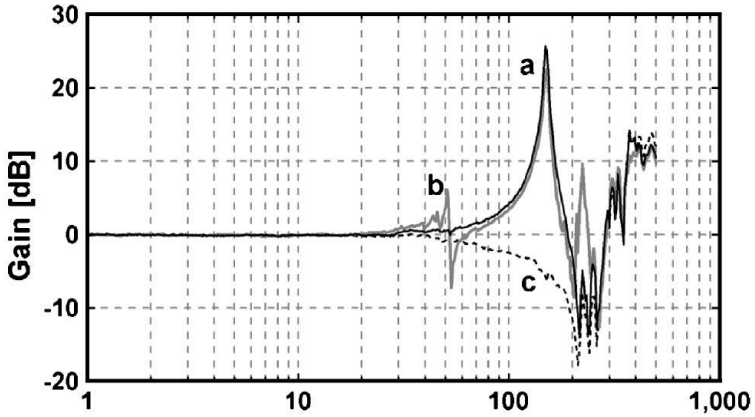

Fig. 2.8: Frequency response of piezo. X-axis indicates frequency (Hz). Line a: Q-peak of piezo actuator. Gray line b: mock actuator curve. Broken line c: sweep amplitude signal compensated by mock actuator. Q-peak is completely removed. Figure reproduced from Kodera *et al*. [112]

Dynamic Proportional-Integral-Derivative (PID) Controller

Parachuting is the effect probe losing contact to surface, therefore is a significant problem for SPM, especially for fast scanning. To avoid parachuting, one needs to adjust the gain used to drive the scanner piezo, depending on the sample height. Gain parameters are not, however, adjusted automatically by the conventional PID feedback circuit. The gain can become too large when the tip scans ascending and too small when the tip scans descending This problem may be tackled using a dynamic PID controller. The principle relies on compensating gain artificially to ascend and descend gradient [113]. Upper and lower thresholds, also called false error signals, are set as the starting point to apply this artificial gain. This false error is larger than the real error signal to adjust on steep uphill (Fig. 2.9). The upper threshold (A_{upper}) is set between set point (A_s) and free amplitude ($2A_0$). When the amplitude exceeds A_{upper}, the false error increases the amplitude further to overcome the obstacle. On the other hand, the false error reduces amplitude when it goes below A_{lower} to avoid parachuting. This dynamic PID control allows HS-AFM to scan sample protein gently in 5 frame per second.

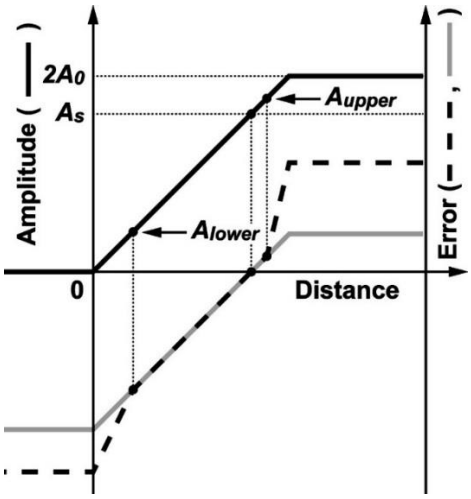

Fig. 2.9: Voltage applied in dynamic PID. Solid line refers to amplitude-distance, gray line to error signal in conventional PID, and broken line to an error signal in dynamic PID. Figure reproduced from Kodera *et al*. [113]

Fig. 2.10 explains how a false error signal is created electronically. By means of op-amp, the signal is split into upper and lower signals. From (ii) to (iv) in the figure, amplitude is multiplied by an amplifier, depending on its gain, and a diode passes the upper amplitude only (Fig. 2.10). At (vii) in the figure, upper and lower false error signals and the real error signal are summed.

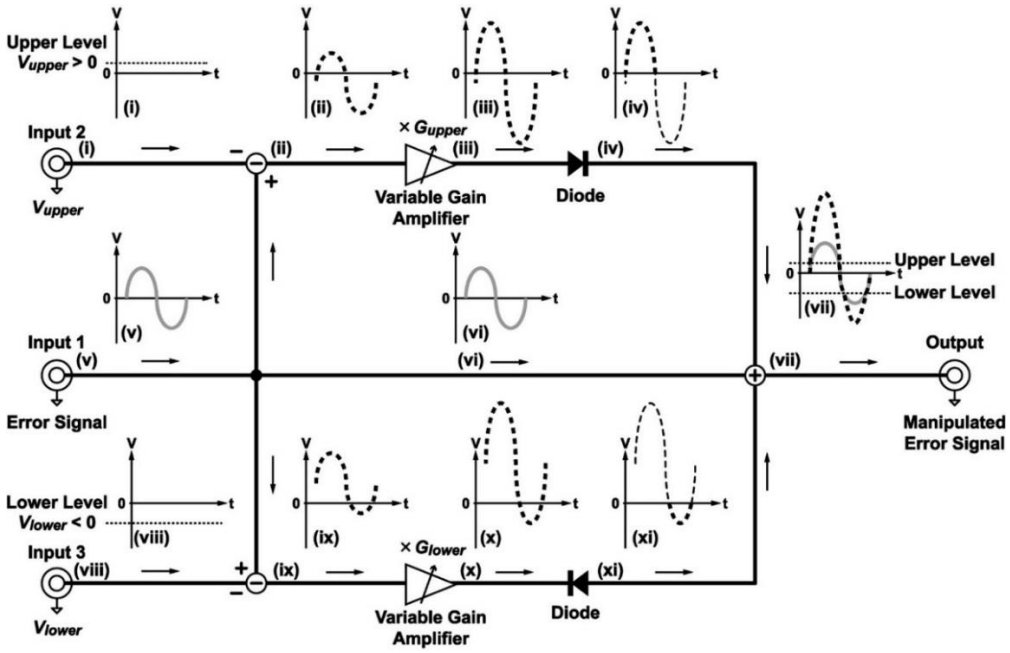

Fig. 2.10: Circuit to produce a false error signal for a dynamic controller. Figure reproduced from Kodera *et al*. [113]

2.2.3 Applications of HS-AFM

The HS-AFM was developed in 2008 and, as stated above, was used in 2010 to observe the walking mechanisms of myosin V on actin filaments [107]. The main challenge in using HS-AFM is the development of an appropriate surface that will allow for the interrogation of the surface at right angles. Positively charged mica by APTES was first used as the surface substrate for the myosin V study. Myosin, however, walks perpendicularly on the surface and a top-down HS-AFM tip was not able to visualize a myosin leg from the side view. In order to overcome this, researchers used a lipid bilayer to control the surface charge and to allow myosin to walk along the side of actin.

Subsequently, the rotary catalysis of F_1 ATPase and the photoreaction of bacterio-rhodopsin were also visualized using HS-AFM [114, 115]. Rotation of the β propeller of F_1 ATPase was shown in real time (Fig 2.11a). Subsequently, the intrinsically disordered region of FACT (facilitates chromatin transcription) proteins was visualized for the first time using HS-AFM by Miyagi *et al.* [107] (Fig 2.11b). HS-AFM presents a major breakthrough in appreciating the structures of intrinsically disordered proteins since, unlike X-ray crystallography and electron microscopy, HS-AFM allows for direct real-time visualization of disordered proteins and their dynamics.

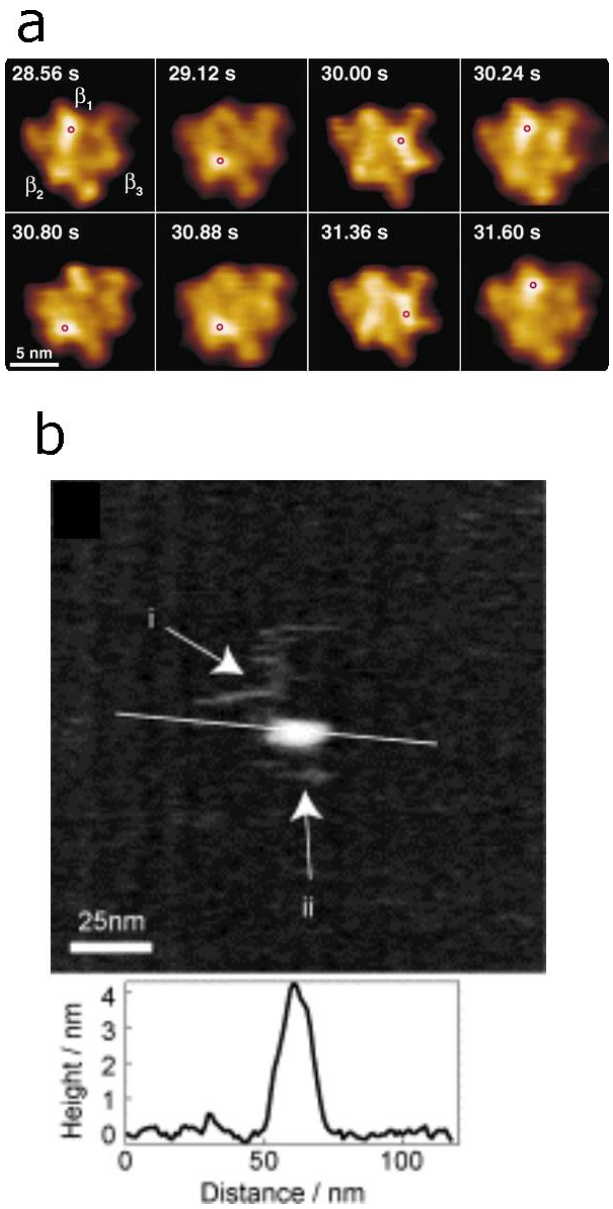

Fig. 2.11: (a) HS-AFM images of F_1 ATPase. Conformational changes of β propeller are seen. Figure reproduced from Uchihashi *et al*. [114] (b) HS-AFM images of FACT protein. Intrinsically disordered region is indicated by the arrow. Figure reproduced from Miyagi *et al*. [116].

2.2.4 Imaging Cell Surface using HS-AFM

Protein dynamics and functionality on *in vitro* systems, such as mica, lipid bilayer and protein 2D crystals, have been convincingly demonstrated by HS-AFM. The next challenge to be addressed involves capturing biological processes within native environments. AFM achieves sub-nanometer resolution on flat and solid surfaces but the resolution decreases on soft and micro-sized spheres such as cells. Current HS-AFM set-ups have two technical problems: the scan range of a standard scanner is too small (maximum 1x1 μm) and the resolution of the optical microscope is too low to capture a cell or a nucleus. In order to overcome these

limitations, I have built a HS-AFM with an ultra-large area scanner (100 μm of maximum XY scan range) and a fluorescence light source to position the cantilever on the object of interest (Fig 2.12a). Similar upgrades were also shown in the publications of Watanabe *et al*. [117] and Shibata *et al.* [118]. Using this new set-up, I interrogated the surface of fixed MDCK cells and observed spikes projecting from the cell surface (Fig 2.12c). The image produced by the ultra-wide area scanner is considerably distorted owing to the long-range piezo expansion, which causes a large hysteresis curve. This needs to be compensated for by a feed-forward method that will control the driving signal in a predefined way.

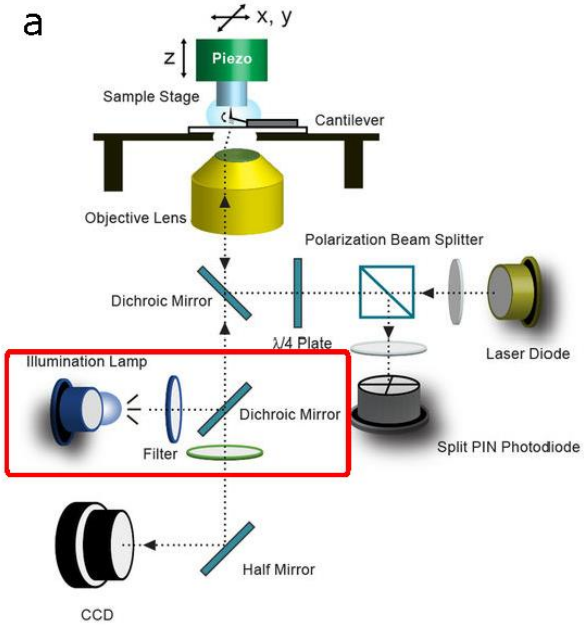

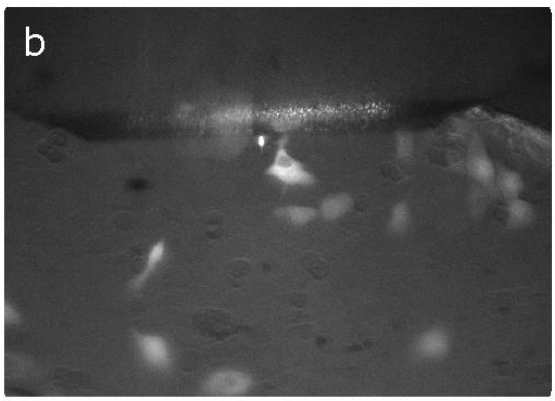

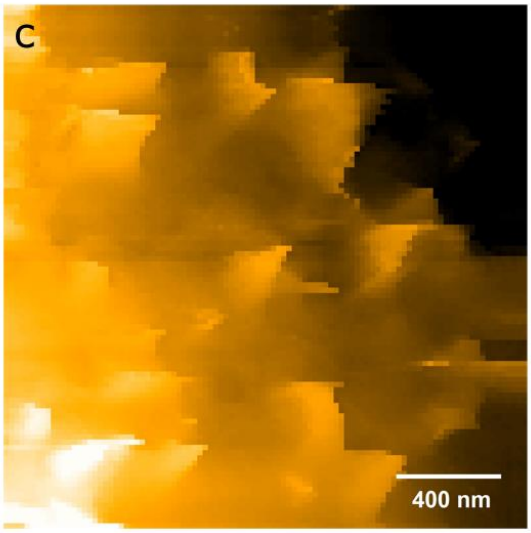

Fig 2.12: (a) Schematic of HS-AFM with an illumination lamp insertion. Inserted illumination lamp is highlighted in the red square. Figure reproduced from Shibata *et al.* [118]. (b) CCD camera image of MDCK cell and cantilever. The 12 o'clock position in the image shows the bright cantilever positioned next to an MDCK cell. (c) HS-AFM image of a 4% paraformaldehyde-fixed MDCK cell surface.

Chapter 3

Spatiotemporal dynamics of the NPC transport barrier resolved by HS-AFM

The chapter has been published in Sakiyama *et al.* 2016, Nature Nanotechnology

3.1 Abstract

Nuclear pore complexes (NPCs) are biological nanomachines that mediate the bidirectional traffic of macromolecules between the cytoplasm and nucleus in eukaryotic cells. This process involves numerous intrinsically disordered, barrier- forming proteins known as phenylalanine-glycine nucleoporins (FG Nups) that are tethered inside each pore. The selective barrier mechanism has so far remained unresolved because the FG Nups have eluded direct structural analysis within NPCs. Here, high-speed atomic force microscopy is used to visualize the nanoscopic spatiotemporal dynamics of FG Nups inside *Xenopus laevis* oocyte NPCs at timescales of ~100 ms. Our results show that the cytoplasmic orifice is circumscribed by highly flexible, dynamically fluctuating FG Nups that rapidly elongate and retract, consistent with the diffusive motion of tethered polypeptide chains. On this basis, intermingling FG Nups exhibit transient entanglements in the central channel, but do not cohere into a tightly crosslinked meshwork. Therefore, the basic functional form of the NPC barrier is comprised of highly dynamic FG Nups that manifest as a central plug or transporter when averaged in space and time.

3.2 Introduction

Nuclear pore complexes (NPCs) mediate the traffic of mRNA, pre-ribosomal proteins and other essential macromolecules between the cytoplasm and nucleus in eukaryotic cells [119]. After two decades of work, it is still debated how NPCs promote the selective transport of cargo-carrying transport receptors known as karyopherins but delay the passage of large non-specific molecules [120]. This problem stems from the fact that the intrinsically disordered, barrier-forming FG Nups [121] have never been directly visualized inside the pore. In marked contrast, the overall NPC structure has been refined by cryo-electron tomography (CET) [122, 123] to a resolution of ~20 Å [124]. Inevitably, *in vitro* experimentation has led to barrier models that postulate different spatial FG Nup arrangements in the NPC. Briefly, the virtual gating [125, 126] /polymer brush model [127, 128] predicts that incoming cargoes encounter an entropic barrier consisting of rapidly fluctuating FG Nups that extend away from their tether sites due to confinement and crowding. The selective phase model claims that the FG Nups span the pore as a tightly cross-linked meshwork based on cohesive hydrophobic interactions between FG-repeats. The size limit to passive diffusion is then determined by the static mesh size [129, 130]. Finally, the Forest model [121] proposes that cohesive and non-cohesive FG Nup regions can assemble into a structure known as the "central plug" or "transporter" [122, 123, 131] (abbreviated as CP/T).

To be precise, nucleocytoplasmic transport *in vivo* proceeds through NPCs in a matter of milliseconds [132]. Therefore, it is the dynamic spatiotemporal behaviour of the FG Nups rather than their static time-independent properties that governs the NPC selective barrier. Yet, very little is known about FG Nup dynamics given the lack of techniques that can first of all visualize and then probe their time-dependent behaviour inside NPCs. Electron microscopy-based approaches require vacuum conditions and sample freezing/fixation which precludes dynamic observation although immunogold labels [133] can provide static snapshots of FG Nup localization. The atomic force microscope (AFM) can provide time-lapse imaging of native NPCs [134] and also stiffness measurements [135] by invasively indenting into the pore. However, AFM data are typically slow to acquire (on the order of minutes) and lack the spatial resolution required to resolve the FG Nups [136]. On the other hand, FG Nup motion can be studied using green fluorescent protein tags [137], or inferred from the localization of fluorescently labelled FG segments, karyopherins and other transport substrates [138, 139]. However, it is important to bear in mind that the FG Nups themselves remain structurally invisible in fluorescence-based studies.

Several key features make high-speed AFM (HS-AFM) advantageous for observing NPCs in action. First, stable tapping mode imaging is possible in aqueous environments at low piconewton forces using short cantilevers and non-linear feedback [106]. Second, the tapping force is applied in microsecond pulses, which minimizes disturbances to the FG Nups since the transfer momentum or impulse is very small [140]. Third, at the most rapid scanning speeds, HS-AFM movies are able to capture dynamic nanoscale movements at ~100 ms frame rates, as has been shown for myosin V [107], the F1-ATPase [141], and intrinsically disordered proteins [116]. Fourth, each cantilever presents a high-aspect-ratio, electron beam-deposited (EBD) amorphous carbon nanofiber tip [140] that is ideal for probing the NPC. In this work, each homegrown EBD tip is 420 ± 141 nm long and has a tip radius of 5.5 ± 0.9 nm (Supplementary Information).

3.3 Results

3.3.1 Examining native NPCs directly

Figure 1a shows a 400 x 400 nm^2 scan obtained at 1.8 frames per second of the cytoplasmic-facing, outer nuclear membrane with several NPCs in view (Supplementary Movie 1). As usual [122-124, 134], we observe considerable pore-to-pore variability, where approximately 40% of all NPCs show large “plug-like” features. We note that these do not represent the CP/T (see below), but are cargoes caught in transit [134] (see Supplementary Information). As their presence would obscure the central channel, we focused on pores that lacked such ‘plugs’. Figure 1b shows an individual NPC averaged over 68 frames recorded at 0.74 frames per second (Supplementary Movie 2). This scan rate, which is moderate for HS-AFM but still far exceeds conventional AFM speeds, facilitates structural averaging by the successive capture of several image frames. This reveals eight cytoplasmic filaments that are 13.7 ± 2.9 nm high, denoting that the eight-fold rotational symmetry of the NPC is consistent with CET measurements [124] (Figure 1c). From here the central channel diameter measures ~40 nm from the full width at half-maximum (FWHM) of opposite facing filaments, whereas the overall NPC diameter is 80 nm when measured from their maxima.

Separate recordings of the inner nuclear membrane reveal the presence of nuclear baskets that decorate the NPCs on their nucleoplasmic end (Figure 1d; Supplementary Movie 3). A single nuclear basket structure, averaged over eight images recorded at 1.5 frames per second, shows eight clearly resolved nuclear filaments that assemble into the so-called distal ring [122, 123] (Figure 1e; Supplementary Movie 4). We note that dynamic movements were observed in the

nuclear filaments and distal ring, however, because this sample was pre-fixed with 2.5% gluteraldehyde only the overall structure of the nuclear basket is analysed. The entire nuclear basket has a diameter of ~120 nm whereas the distal ring is ~40 nm in diameter [122] and ~20 nm thick, judging from where individual nuclear filaments separate (Figure 1f).

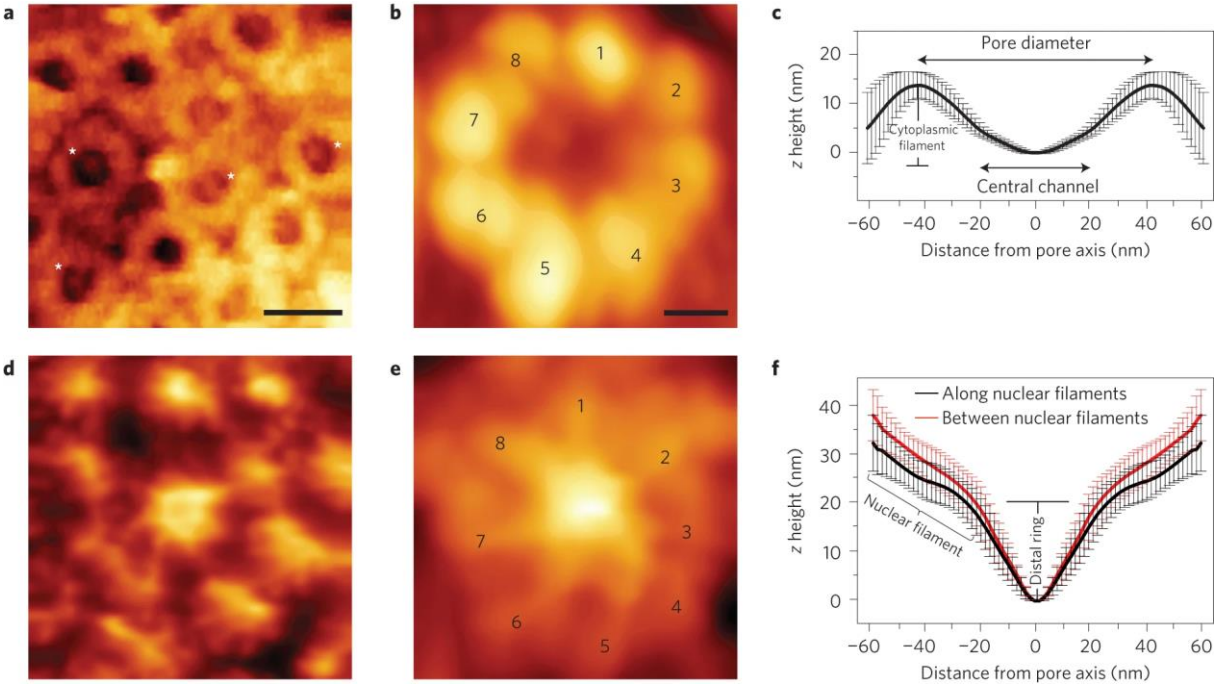

Fig. 3.1: Observing native NPCs by HS-AFM. **(a)** Numerous NPCs decorate the cytoplasm-facing outer nuclear membrane. Pore-to-pore variability shows vacant NPCs as well as NPCs that are clogged with large cargoes-in-transit (indicated by ★). Scale bar = 100 nm. **(b)** Average projected structure of a vacant NPC as seen from its cytoplasmic face. Eight cytoplasmic filaments surround a central pore. Scale bar = 25 nm. **(c)** Average cross-sectional height profile of (B) showing that the height of a single cytoplasmic filament is ~13 nm. Error bars denote standard deviation. The overall pore diameter is ~80 nm when measured from the maxima of opposing filaments while the central channel diameter is ~40 nm. **(d)** Nuclear baskets protrude away of the inner nuclear membrane. Same scale as (a). **(e)** Average structure of a nuclear basket showing eight distinct nuclear filaments (numbered) that fuse into a distal ring. Same scale as (b). **(f)** Average cross-sectional height profile of (e) showing that the nuclear basket is ~40 nm-tall and ~120 nm-wide. At the bottom of the structure, ~45 nm-long nuclear filaments fuse into a distal ring that is ~40 nm-wide and ~20 nm-thick. The nuclear basket corss-section in (f) is inverted with respect to (e) so as to conform to the orientation of the NPC as defined in (c).

3.3.2 Dynamic disorder underpins FG Nup barrier function

To resolve FG Nup behaviour, we focused a 50 x 50 nm^2 scan area squarely on the entrance of the aqueous central channel surrounded by the cytoplasmic filaments (same NPC as Figure 1b), and increased the scan rate to 5.6 frames per second (i.e., 180 ms per frame; fast). A post-experiment image registration algorithm was used to align consecutive frames in the XY plane and correct for drift in the Z direction (Supplementary Information). Subsequent playback shows remarkable dynamic behaviour within the pore (Supplementary Movie 5). Further implementing basic image filtering (Supplementary Information) reveals the flailing motion of polypeptide chains being the FG Nups that repeatedly extend into and retract from the central channel (Supplementary Movie 6). This is similar to the diffusive motion of a different intrinsically disordered protein previously observed by HS-AFM[116], and evokes the characteristics of virtual gating [125, 126], where the FG Nups collectively bristle, whip and writhe in a brush-like manner from their tethering points [128].

Figure 2a shows successive snapshots of the same region, highlighting sequential changes in FG Nup motion under the elapsed time of 180 ms per frame. First and foremost, the FG Nups emanate from eight apparent tether points that seem to be unchanged from one frame to the next, although their positions deviate from an eightfold rotational symmetry. Typically, not all eight FG Nups are present in a single frame as HS-AFM has difficulty resolving the ones that protrude into or out of the XY-plane – this is consistent with the dynamics of Nup153 at the nuclear basket [137]. Yet, their dynamic behaviour is unmistakable in that no two frames share the same features and the pore is never devoid of FG Nups for more than the elapsed time between frames. Although their exact identity is unclear, we speculate that the FG Nups represent either Nup214 or Nup62 due to their location close to the cytoplasmic entrance [142]. The average extension length of the FG Nups is 15.1 ± 3.9 nm, which exceeds the in-solution hydrodynamic diameter (~9 nm) of several metazoan FG Nups including Nup214, Nup62, Nup98 and Nup153 [143]. Cross-sectional height analyses further shows that the average FG Nup thickness is 0.48 ± 0.12 nm (Supplementary Information), which is consistent with the persistence length of an FG Nup [128]. The lateral width substantially exceeds this value due to tip convolution effects, which is well-known in AFM [144] (Supplementary Information).

Interestingly, the FG Nups can adopt dynamic spatial conformations that recall static descriptions of the NPC barrier [121, 125-131] (Figure 2b). In particular, extended FG Nups

that coincide and intermingle in the central channel give the appearance of a sieve-like conformation. Nevertheless, this entanglement is short-lived as the FG Nups detach within two or three frames (less than 500 ms). Therefore, any resemblance to the formation of a tightly cross-linked, pore-spanning meshwork [129, 130] is coincidental although charged or hydrophobic inter-FG repeat interactions might factor into this behavior. Still, it is striking that the FG Nups can radiate inwardly from their tether points to form a radial arrangement of polypeptide chains, even appearing to straighten under tension [128]. Overall, these transient entanglements are considerably smaller in size (i.e., 1.71 ± 0.39 nm) than the hydrodynamic diameters of a karyopherin (karyopherinβ1 ~ 10 nm) [143] or large cargo (> 5 nm) and should not be mistaken for cargoes caught in transit [122, 123, 134] (Supplementary Information).

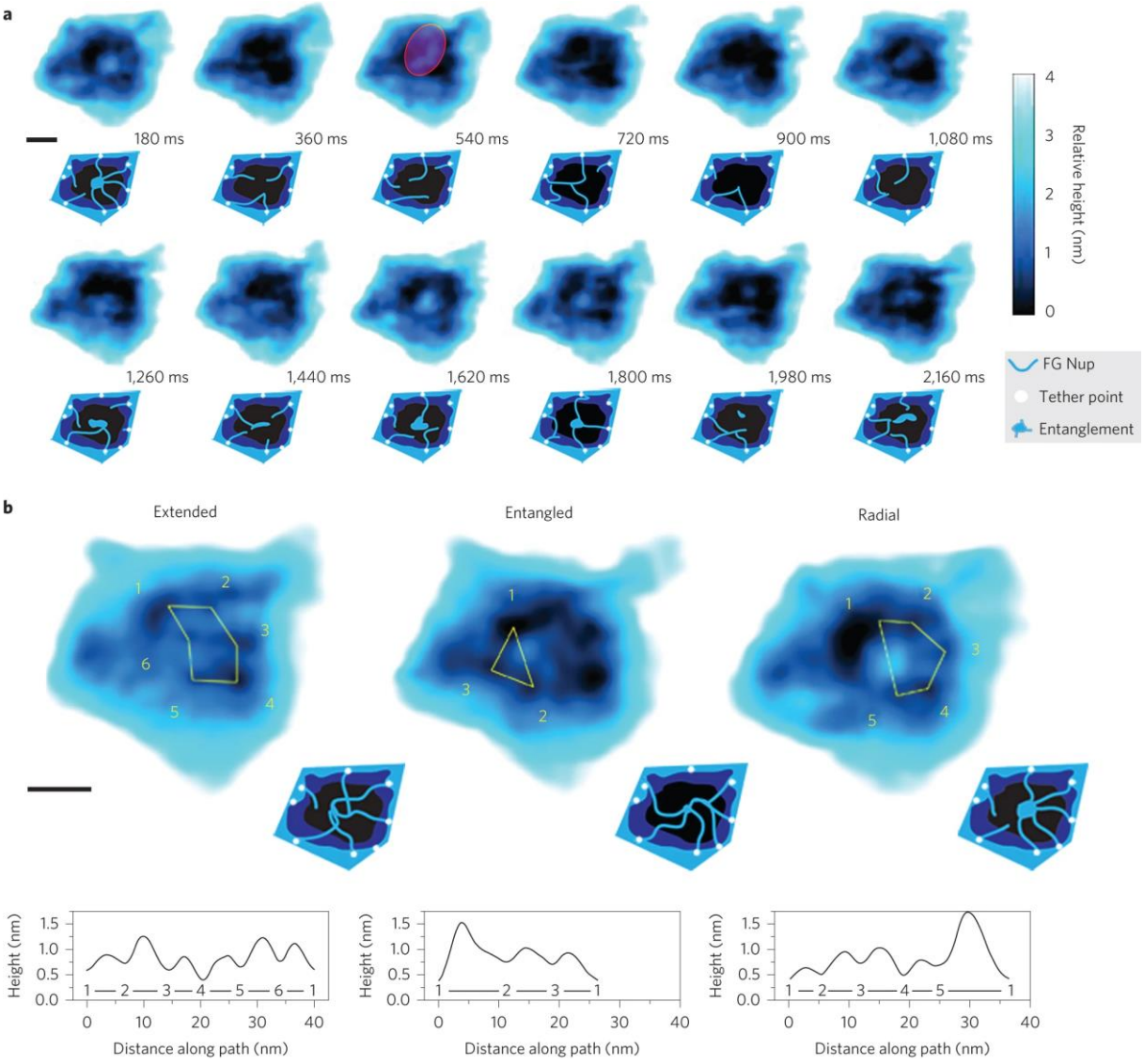

Fig. 3.2: HS-AFM resolves dynamic FG Nup behaviour inside an individual NPC. **(a)** Successive frames reveal the spatiotemporal behaviour of the FG Nups. The accompanying

illustrations and legend emphasize the key features in each frame corresponding to the FG Nups including eight apparent tethering points that remain unchanged even though no two frames are the same. The time elapsed between frames is 180 ms. A representative FG Nup is highlighted (red) at 540 ms. Scale bar = 10 nm. **(b)** Dynamic FG Nups that coincide and intermingle in the central channel can manifest transient arrangements. Represented are "extended", "entangled" and "radial" conformations. The height profiles correspond to cross-sectional features encountered along the path demarcated by a polygon (yellow). Each number corresponds to the corner of a polygon. The accompanying illustrations highlight the observed FG Nup behavior in each frame. Scale bar = 10 nm.

3.3.3 Exposing the identity of the central plug/transporter

Molecular fluctuations occur under microsecond timescales [145], therefore the exact trajectories of individual FG Nups remain inaccessible at the current HS-AFM scan speeds. To gain insight into collective FG Nup motion, we plot their Z-directional mean-square-displacement (MSD_Z) as a function of time in Fig. 3a (Supplementary Information) comparing values obtained at the pore edge and centre. In contrast to free diffusion, within one second both MSDs reach saturation, in agreement with the restricted diffusion of a tethered polypeptide chain [146]. This gives a maximum Z-diffusional limit [147] L_Z (where $MSD_Z \propto L_Z^2/6$) of 0.9 nm and 1.6 nm at the pore edge and centre, respectively (Supplementary Information), providing that larger fluctuations are not being supressed or undetected by the HS-AFM tip. Evidently surface tethering plays a key role in constraining the FG Nups to the NPC wall whereupon their intrinsically disordered domains emanate and diffuse into the central channel. Hence, a lack of such physical tethers could facilitate the unconstrained aggregation of free-floating FG Nups in solution [148] because their mobility is no longer spatially restricted to their anchoring sites. This calls into question the static properties of the FG Nups at equilibrium timescales inside the NPC. Figure 3b simulates the effect of scanning slowly at 1800 ms per frame by averaging over every ten successive frames 180 ms apart. Effectively all dynamic motion is lost and replaced by a static structure resembling the CP/T [121, 131, 135, 149] (Supplementary Movie 7).

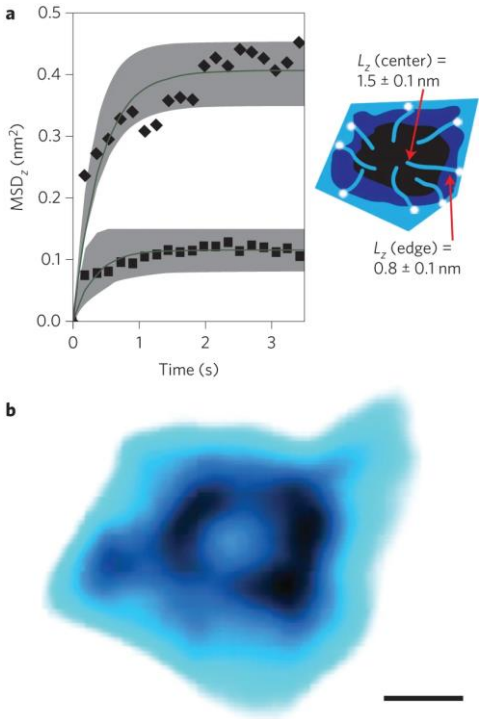

Fig. 3.3: Spatiotemporal averaging of FG Nup behaviour. **(a)** A plot of Z-directional mean-square-displacement (MSD_Z) as a function of time shows saturating behaviour consistent with the restricted diffusion of tethered polypeptide chains. The Z-diffusional limit L_Z shows that FG Nup diffusion is more constrained close to their tethering points at the pore edge than their fluctuations at the pore center. **(b)** The average projection of ten successive frames at 180 ms apart simulates the time-independent outcome of an ensemble-averaged measurement (i.e., 1800 ms). Effectively all dynamic FG Nup structure is lost and replaced by a central condensate-like structure resembling the so-called central plug/transporter. Scale bar = 10 nm.

3.3.4 Entropic exclusion operates in space and time

Based on the above analysis, static "time-averaged" interpretations of the NPC barrier mechanism provide only limited insight, bearing in mind that karyopherins import in ~5 ms [132], while larger mRNAs export in ~200 ms [150]. Clearly, transport-relevant FG Nup behavior is underpinned by constraints in both space (e.g., surface tethering) and time (e.g., translocation speed). In this respect, aspects of their spatial arrangement [149, 151-153] and chain dynamics [154-156] have been explored theoretically and in computational studies ranging from atomistic to coarse-grained molecular dynamics simulations. However, a consensual view of transport-relevant phenomena has yet to emerge. This is due in part to differences in parameterization, structural detail and simulation time. Our findings indicate that different cargoes probably experience varying degrees of entropic exclusion depending on their size, (size-dependent) diffusion times and biochemical interactions with the FG Nups.

This alludes to the presence of a spatiotemporal barrier as shown in Figure 4, defined as the number of FG Nup fluctuations that collide with a particle in space to delay it in time. Thus, a small cargo with a short diffusion time (i.e., fast) encounters a low barrier and has a high probability of entry. In contrast, a large particle with a long diffusion time (i.e., slow) experiences a high barrier and is more effectively hindered from entering the pore. Indeed, the resilience of the FG Nups against the HS-AFM tip, which oscillates with a mechanical energy of ~$20k_BT$ [157] (k_B: Boltzmann constant, T: temperature), further underscores the effectiveness of entropic exclusion against macromolecular diffusion (i.e., k_BT), contrary to recent claims [130, 158]. This barrier is lowered [153] for large cargo-carrying karyopherins that exert fast binding kinetics with the FG Nups [34, 143, 159] and retract dynamically [127, 143] into a more malleable form. Importantly, these scenarios are consistent with the finding that entry into the NPC does not pose a rate-limiting step for selective transport [150]. More generally, this underscores the "fuzzy" dynamics [160] that intrinsically disordered proteins or domains might confer to regulating protein-protein interactions [161].

3.4 Discussion

To conclude, we have used HS-AFM to resolve FG Nup behavior approaching the spatiotemporal resolution of coarse-grained computer simulations. This uniquely addresses the spatiotemporal "no-man's-land" that lies between time-averaged measurements and atom-resolved molecular dynamics. In surpassing static measurements of "averaged out" behavior, HS-AFM can be of particular use in studying highly dynamic and disordered systems. By observing the pore at transport-relevant timescales, we have obtained the first direct physical proof of the NPC barrier mechanism, which comprises highly dynamic FG Nups. Importantly, this brings consensus and clarity to barrier models, which mainly disagree on their static arrangements in the pore. Nevertheless, whether and how such dynamic FG Nup behavior changes under authentic trafficking conditions within a cellular milieu remains to be ascertained. In particular, the question of how cargo-carrying karyopherins rapidly negotiate the central channel and whether large cargoes perturb the overall NPC structure await further study.

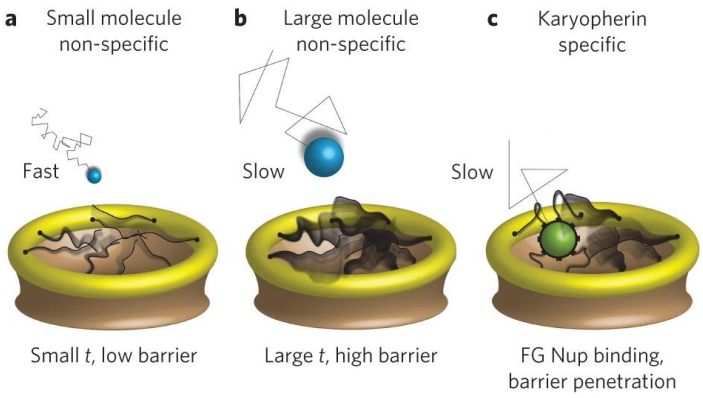

Fig. 3.4: Entropic exclusion works in both space and time. **(a)** A small molecule undergoing fast diffusion is more likely to enter the NPC because it "sees" the FG Nups moving in "slow motion". **(b)** When diffusion is slow, large particles are effectively hindered by repeated collisions with the rapidly fluctuating FG Nups that envelop more space. **(c)** Cargo-carrying karyopherins penetrate the spatiotemporal barrier by exerting fast binding kinetics with the FG Nups. *t*, time. Darker shades emphasize spatiotemporal motion.

3.5 Methods

Nuclear envelope preparation

All samples were prepared as described previously [134]. Mature oocytes were surgically removed from female *Xenopus laevis* and kept in Modified Barth`s saline (MBS) (88 mM NaCl, 1 mM KCl, 0.82 mM $MgSO_4$, 0.33 mM $Ca(NO_3)_2$, 0.41 mM $CaCl_2$, 10 mM Hepes, pH 7.5, and 100 U/ml of penicillin-streptmycin) for up to 3 days. Nuclei were ejected from needle-punctured oocytes in low salt buffer (LSB) (1 mM KCL, 0.5 mM MgCl2, 10 mM Hepes, pH 7.5) within 20 min. Yolk particles and other debris were removed by pipette aspiration. Nuclei were transferred into a clean Petri dish filled with LSB and adsorbed onto a poly-L-lysine (PLL)-coated HS-AFM glass sample stage without further chemical treatments. Glass capillaries were used to spread the nuclear envelope on the sample stage, followed by a 2 hour incubation in LSB to remove chromatin and other debris. HS-AFM experiments proceeded in 60 µl of LSB without further fixation to facilitate structural comparisons with cryo-electron tomography studies [123, 124] noting that salt concentrations increased over time due to evaporation at room temperature. Subsequent nuclear basket experiments included a prefixation step using 2.5% gluteraldehyde in LSB before HS-AFM. Dynamic light scattering (Zetasizer Nano, Malvern Instruments Ltd, Worcestershire, United Kingdom) shows that FG Nup hydrodynamic size (i.e., conformation) is not significantly impacted in LSB compared to other buffers (Supplementary Information).

High-speed atomic force microscopy

All experiments were conducted using a commercial HS-AFM 1.0 system (RIBM, Japan) featuring a standard scanner with a maximum scan speed of 80 ms per frame. Electron beam deposited (EBD) carbon tips were grown onto commercial BL-AC10DS-A2 (Olympus) cantilever tips. The supplier-provided specifications of these cantilevers are: spring constant = 0.02 – 0.2 Nm^{-1}; resonance frequency in water = 300 – 700 kHz; quality factor in water = ~2. Overall, more than one hundred nuclear envelopes were scanned. While visualizing NPCs is routine, image resolution can vary depending on tip quality, stability, and sample roughness. The FG Nup data shown here is representative of our most highly resolved data. Typical experiments commenced with a coarse "zoom out" scan of the nuclear envelope, followed by zooming into an individual NPC, and finally a high-speed scan of the pore opening. HS-AFM movies of the FG Nups were recorded using setpoints that corresponded to a maximum tapping force of ~100 pN. The time for each tap, which is 2.5 μs ensures that the impulse [106], or momentum transferred to the FG Nups is small thereby ensuring that any disturbance to the FG Nups is minimized (Supplementary Information).

Image and data analysis

All data were analysed using custom written code in Python and Fiji image analysis package as described in the Supplementary Information.

3.6 Supplementary Information

1. Electron Beam Deposited (EBD) carbon tip preparation

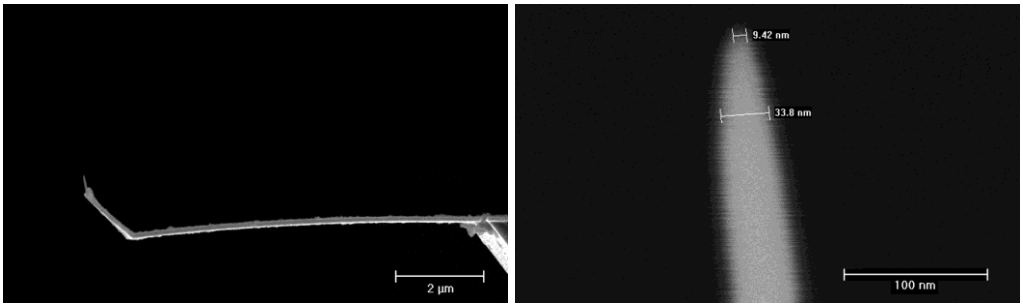

This protocol has been described previously [140]. An amorphous carbon nanofiber tip was grown by electron beam deposition (EBD) onto the pre-existing tip of a commercial HS-AFM cantilever (BL-AC10DS-A2; Olympus). The EBD process was carried out in-house inside a scanning electron microscope (SEM) (FEI XL30 ESEM-FEG). This involved evaporating phenol in the chamber surrounding the cantilever at low pressure (10^{-6} mBar). Using a small aperture of 30 μm and accelerating voltage (5 kV) typically ensured that EBD tips were

grown with average lengths of 420 ± 141 nm and tip radii of 5.5 ± 0.9 nm. Each EBD tip was grown with a 10° tilt from the normal of the cantilever base to compensate for a 10° tilt in the glass sample stage. HS-AFM cantilevers were recycled by using a focused ion beam instrument (Helios NanoLab 650) to remove used EBD tips.

2. Image alignment

HS-AFM movies were converted, processed and analyzed using in-house software written in Python using numerical libraries: NumPy, SciPy, scikit-image, Matplotlib and SimpleITK [162-166]. Because HS-AFM is prone to intrinsic drift in the XY-plane and in the Z direction, the acquired movies were aligned before further analysis using an image registration algorithm. In the first step, a reference frame was selected from each movie, and all the remaining frames were adjusted by translation in the XY-plane. The optimal translation vector was obtained by maximization of a normalized cross correlation (NCC) coefficient between the frame being translated and the reference frame. The movies were cropped to regions, which contained data for all frames. These calculations were performed using image registration routines implemented in SimpleITK library. To correct Z-drift, the frames were shifted to the reference frame by minimizing their mean square difference. Furthermore, each movie was uniformly translated in Z to attain a minimum value of 0 nm. The XY and Z aligned movies were averaged using Fiji software [167], which was also used to extract details of structural features (Fig. 1b and 1e).

3. Image processing

In general, a 3 pixel median filter was applied along the Y-axis to remove horizontal stripes (i.e., X-axis; the fast scan direction). Next, a 2D Gaussian filter with 1 pixel standard deviation was applied to improve signal to noise ratio. Subsequently, we applied a 3 times scaling factor in XY with bicubic interpolation to further reduce pixilation. However, the exact image processes used differ between movies and are explicitly listed below.

4. Cross-sectional analysis

Feature sizes were obtained from cross-sectional height profiles of selected frames. A well-known problem in AFM (and HS-AFM) is that the lateral feature dimensions are convoluted by the size and curvature of the tip [144]. Therefore, Z heights provide the highest accuracy with a resolution of ~0.15 nm [140]. Indeed, by scanning an atomically flat mica surface we

determined the intrinsic noise level of the HS-AFM to be ~0.15 nm at the same scan control parameters used when imaging NPCs. Scale bar = 10 nm.

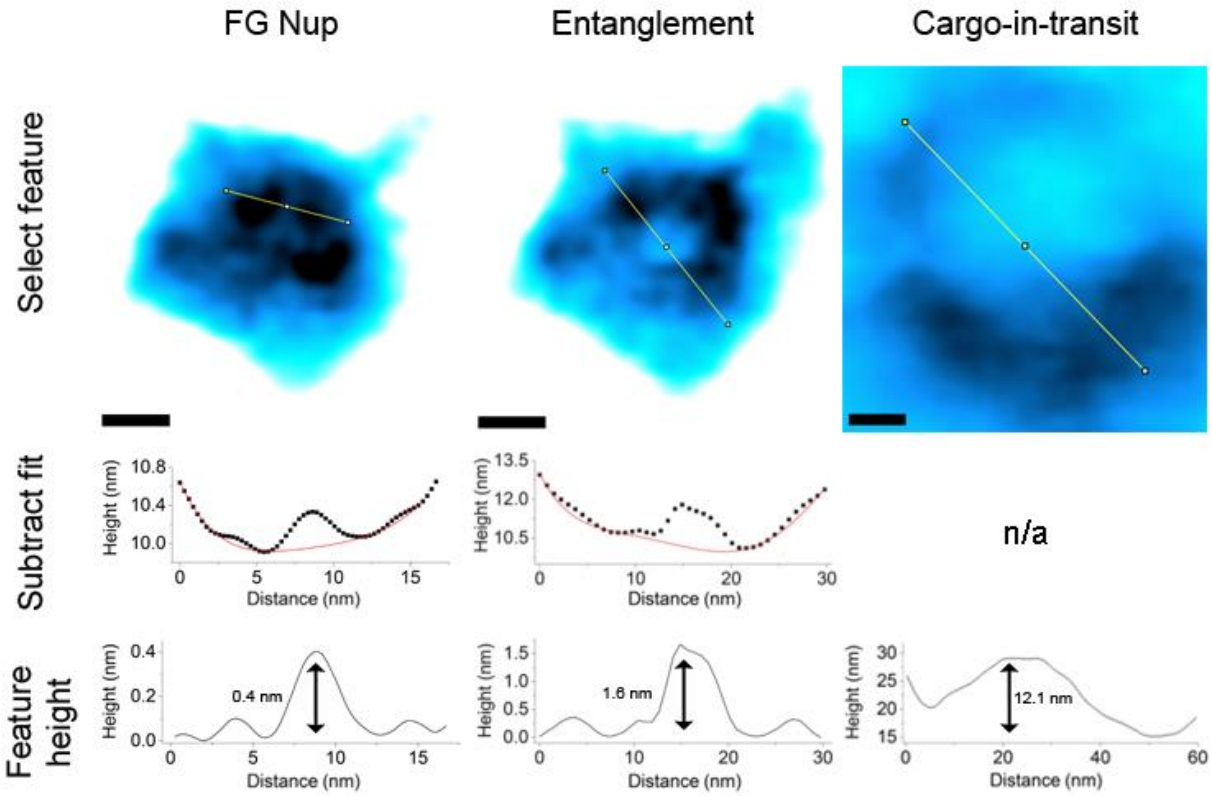

Heights of individual FG Nups and FG Nup entanglements were obtained by subtracting from each line section (black dots) a polynomial fit (red line) to compensate for curvature in the cross-sectional pore geometry. The average heights were found to be 0.48 ± 0.12 nm and 1.71 ± 0.39 nm for an individual FG Nup (N = 20) and entangled FG Nups (N= 19), respectively. The heights of "cargoes-in-transit" were directly measured from the line section being substantially larger at ~10 nm in size.

5. Lateral tip convolution

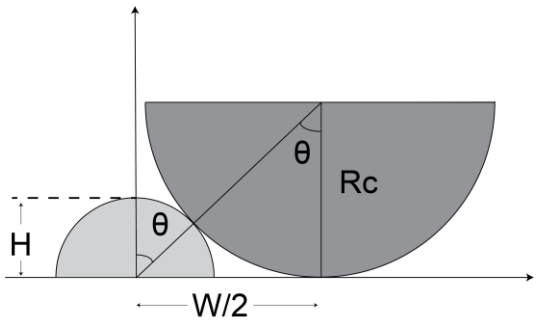

The extent of lateral tip convolution can be estimated [144] using

$$W^2 \approx 8R_cH$$

where W, R_c, H represent the convoluted width of object, tip radius, and object height, respectively.

Knowing W and H allows one to verify the influence of lateral tip convolution during HS-AFM by solving for R_c. Indeed, by averaging over the lateral widths of 1.0 nm-thick features, we obtain an average tip radius of 7.8 ± 4.83 nm, which is consistent with the SEM-obtained value of 5.5 ± 0.9 nm (N = 20).

6. MSD analysis

Mean square displacements in the Z-direction (MSD_Z) were computed to assess collective FG Nup dynamic in the NPC using

$$MSD_z(n \cdot \Delta t) = \frac{1}{N-n-1} \sum_{j=0}^{N-n-1} \big(z(j\Delta t + n\Delta t) - z(j\Delta t)\big)$$

where N is the total number of frames and n = 0, …, $N/2$. The $MSD_z(\tau)$ profiles were calculated separately for each pixel of the movie.

Furthermore, a model of restricted diffusion [147] was used to characterize the amplitude and timescale of the dynamic processes. Within this model, MSD curves were fitted to yield the diffusion limit L_z and diffusion coefficient D_z.

$$MSD_z(\tau) = \frac{L_z^2}{6} - \frac{16L_z^2}{\pi^4} \sum_{n=1,3,5,\dots}^{\infty} \frac{1}{n^4} \exp\left(-\frac{n^2\pi^2 D_z}{L_z^2}\tau\right)$$

Due to the fast dynamics of the individual FG Nup chains, the MSD curves are very steep for the first time step (Fig. 3a). This behavior leads to high uncertainty of the diffusion coefficient D_z values, as some of the underlying processes are faster than the sampling rate. Nevertheless, the limit of the restricted diffusion L_z can be extracted from the plateau value of $MSD_z(\tau) \propto \frac{L_z^2}{6}$. For the same reason, the higher order terms (n > 1) of the sum in the equation above were negligible, and therefore not evaluated. The MSD calculations and fittings were performed using in-house Python routines.

7. Dynamic Light Scattering

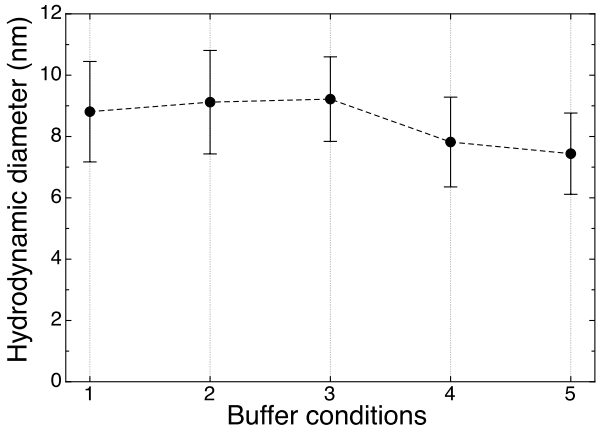

Dynamic light scattering demonstrates that low salt buffer does not significantly influence the conformation (i.e., hydrodynamic size) of Nup62, in comparison to other buffers:

1 - Low salt buffer: 1 mM KCL, 0.5 mM $MgCl_2$, 10 mM Hepes, pH 7.5

2 - Low salt buffer x 2

3 - Nuclear isolation medium [168]: 90 mM KCl, 10 mM NaCl, 2 mM $MgCl_2$, 10 mM HEPES, 0.09 mM $CaCl_2$, 1.1 mM EGTA, pH 7.3

4 - Stoffler *et al* [134]: 10 mM HEPES, 100 mM KCl, pH 7.5

5 - Phosphate buffered saline: 1.54 mM KH_2PO_4, 155.17 mM NaCl, and 2.71 mM Na_2HPO_4-$7H_2O$ pH 7.2

8. High-Speed AFM

The HS-AFM tapping force F_{max} can be expressed by [107, 141]

$$F_{max} = \left(\frac{k_c}{Q_c}\right) \times \left[A_0(1-r) + h_0 \sin\left(\frac{\theta}{2}\right)\right]$$

where k_c is the cantilever spring constant, Q_C is the quality factor, A_0 is the free oscillation amplitude, r is the setpoint, h_0 is the feature height, and θ is the phase shift. The supplier-provided specifications are k_c = 0.1 $N{\cdot}m^{-1}$, fc = 400 kHz, Q_c = 2 for the HS-AFM cantilevers (BL-AC10DS-A2; Olympus). Using A_0 = 6 - 7 nm, r = 0.8 – 0.7, FG nup height h_0 = 0.5 nm and phase shift θ = 28.7°, we estimate the maximum tapping force F_{max} to be 110 pN in all NPC experiments. However, in HS-AFM the impulse (= *Force x* time) is a more meaningful mechanical quantity [140] because this describes the momentum transfer in the short time it takes the tip to make a single tap, which in the present study is 2.5 μs. Therefore, the anticipated impact on the NPC is very small thereby ensuring that any disturbance to the FG Nups is minimized. However, for this reason we avoided probing further into the NPC.

3.7 Supplementary Movies

Supplementary movies are available online at DOI:10.1038/NNANO.2016.62

3.7.1 Supplementary Movie Details

Supplementary Movie 1a: 400 × 400 nm^2 area of a nuclear envelope featuring several NPCs filmed at 550 ms per frame (1.8 frames per second) with 100 × 100 pixels. Each frame was processed using a 3 pixel median filter followed by a 3x scaling factor with bicubic interpolation. The movie is played back in real time. Scale bar = 100 nm. Fig. 3.1a is an individual frame taken from this sequence.

Supplementary Movie 1b: This movie was cropped from an original 150 × 150 nm^2 scan of an individual NPC filmed at 1360 ms per frame (0.74 frames per second) with 100 × 100 pixels. Each frame was processed using a 3 pixel median filter, a 2D Gaussian filter with 1 pixel standard deviation and a 3x scaling factor with bicubic interpolation. The movie is played back at 3 frames per second (sped up roughly by 4 times). Scale bar = 25 nm. The NPC structure shown in Fig. 3.1b is an average of all frames in this sequence.

Supplementary Movie 1c: 400 × 400 nm^2 scan of several nuclear baskets filmed at 800 ms per frame (1.25 frames per second) with 120 × 120 pixels. Each frame was processed using a 3 pixel median filter, a 2D Gaussian filter with 1 pixel standard deviation and a 3x scaling factor with bicubic interpolation. The movie is played back in real time. Scale bar = 100 nm. This sample was pre-fixed in 2.5% gluteraldehyde. Fig. 3.1d is an individual frame taken from this sequence.

Supplementary Movie 1d: 130 × 130 nm^2 scan of an individual nuclear basket filmed at 670 ms per frame (1.5 frames per second) with 80 × 80 pixels. Each frame was processed using a 3 pixel median filter, a 2D Gaussian filter with 1 pixel standard deviation and a 3x scaling factor with bicubic interpolation. The movie is played back in real time. Scale bar = 25 nm. The nuclear basket structure shown in Fig. 3.1e is an average of eight frames from this sequence. This sample was pre-fixed in 2.5% gluteraldehyde.

Supplementary Movie 2a: This “raw” movie was cropped from an original 69 × 69 nm^2 scan taken at the cytoplasmic orifice of the NPC. It was filmed at 180 ms per frame (5.6 frames per second) with 80 × 80 pixels. Each frame was processed using a 3x scaling factor with bicubic interpolation. The movie is played back in real time. Scale bar = 10 nm.

Supplementary Movie 2b: This is the same recording of the NPC cytoplasmic orifice shown in Supplementary Movie 2A except with additional filtering using a 3 pixel median filter and a 2D Gaussian filter with 1 pixel standard deviation. The movie is played back in real time

(5.6 frames per second). Scale bar = 10 nm. The frames shown in Fig. 3.2a and 3.2b are taken from this sequence.

Supplementary Movie 3: This takes the movie of the NPC cytoplasmic orifice shown in Supplementary Movie 2b but makes an average image out of every 10 consecutive frames for all frames. Playback is at 0.56 frames per second. The image shown in Fig. 3.3b is taken from this sequence.

Chapter 4

HS-AFM Analysis of Artificial Nanopore Systems

Parts of this chapter were published in Emilsson *et al*. (2018), Nanoscale

4.1 Introduction of Artificial Nanopores

4.1.1 Emergence of Biomimetic Nanopores

Membranes perforated with single or multiple nano-sized pores are employed as biosensors, nanofluidic devices and molecular filters [169-172]. The simplest filtration mechanisms are dependent on size, density and shape of the pore. There is significant interest to integrate biological nanopores with biomimetic devices to add regulatory mechanisms that widen the range of possible usage. For example, ion channels for electrical signaling in nerves, muscles and synapses make use of particular electrochemical effects (voltage-gated) or ligands (ligand-gated) to trigger structural changes [173-175]. Pore forming proteins from the superfamily of porins represent another major class of biological nanopores [176]. Unlike ion channels that undergo structural transitions, porins regulate their permeability by ionizable residues in the center of their pore rendering them sensitive towards pH. For example, the outer membrane protein F (OmpF) from *Escherichia coli* allows a higher ion inflow in alkaline solutions than under acidic conditions [177]. On the other hand, NPCs that regulate nucleocytoplasmic transport contain intrinsically disordered protein domains that act as a permeability barrier. These examples indicate the variety of gating strategies found within biological nanopores. Biological nanopores, however, exhibit limited stability and are challenging to study. Therefore, major efforts have been taken to mimic biological nanopores to either prolong the lifetime or recapitulate the functionality in both physiological and non-physiological settings. Engineering desired properties within solid-state pores *ex vivo* thereby opens access to natural occurring mechanisms for industry and medical applications. Since structural changes are restricted, solid-state nanopores are mainly functionalized with stimuli-responsive polymers reminiscent to those present in the NPC. Therefore, investigating bio-mimetic, stimuli-responsive, solid-state nanopores can be insightful for understanding the working principles of transport within a cell.

Such functionalized nanopores have been studied by many methods including fluorescence microscopy, ion conductance measurements and electron microscopy. While these methods have provided further insights into the underlying mechanism of nanopore transport, they only look at a “snap shot” of the transport and provide indirect clues.

4.1.2 Stimuli Responsive Nanopores

Stimuli-responsive nanopores modulate their permeability based on external triggers. Because of their sensitivity to electro-chemical reactions, pH responsive nanopores have been the most

extensively studied and characterized. There are two major design principles to reconstitute pH sensitivity in transport through solid-state nanopores: surface charge and functionalization with pH responsive polymers.

The former takes advantage of the protonation state of polymeric solid-state material. When the pH of the used electrolyte is higher than the isoelectric point of the polymer surface the surface will be negatively charged [178], thereby rectifying positive ion flow due to an attractive electrostatic force. For lower pH values the surface is protonated, thereby positive ions can pass freely due to repulsive force.

The latter makes use of pH responsive polymers such as Poly (4-vinyl pyridine) (PVP) and Poly (acrylic acid) (PAA) grafted on to the pore surface [179, 180]. E.g. a PVP brush swells by gaining protons in acidic milieus, while PAA swells in a basic environment and collapses under acidic conditions.

Next to pH, another accessible trigger is temperature. Poly-N-isopropylacrylamide (PNIPAM) is currently being used to design, temperature responsive nanopores [181, 182]. PNIPAM chain lengths can vary depending on polymerization time and this can influence the properties of the designed nanopores. Short brush layers created by short polymerization times collapse at temperatures higher than ca. 29 °C causing the inner diameter of the nanopore to enlarge. Long PNIPAM polymers created by longer polymerization times can cover the nanopore and possibly form cross-links. At higher temperatures, long PNIPAM layers become dehydrated [181]. One interesting observation is that PNIPAM can go through pores of sizes that are less than the polymer's hydrodynamic diameter due to attractive interactions between PNIPAM and the pore wall. 50 nm diameter artificial nanopores functionalized by PNIPAM were used to study DNA translocation [183]. PNIPAM functionalized nanopores and PNIPAM functionalized carrier molecules are used because of their homopolymer interaction. Bare single stranded DNA cargo (bare cargo) and PNIPAM functionalized cargo (carrier cargo complex, CCC) are used for transport. Accumulation rates of CCC through PNIPAM grafted membrane is 2.6 times higher than bare cargo at 25 °C, indicating that attractive interactions accelerate transport.

4.1.3 Artificial Nanopores that Mimic NPCs

As described in Chapter One, NPCs perforate the nuclear envelope and are the sole regulators of the nucleocytoplasmic transport. It can therefore be perceived that the nuclear envelope resembles a filter which extracts only macromolecules of interest (e.g. NTR, mRNA, RNP). On this basis, a number of stimuli responsive nanopores mimicking the NPC have been developed.

Jovanovic-Tailsman and colleagues coated polycarbonate membranes with yeast FG Nups Nsp1 and Nup100 to create biomimetic NPCs (Fig 4.1a). Nuclear transport factor 2 (NTF2), which binds the FG Nups, translocates through the biomimetic nanopore 3 times faster than bovine serum albumin (BSA), a non-specific protein. Kap95-GFP, a fluorescently labeled yeast homolog of Kapβ1, transports two times faster than GFP alone. Moreover, Kap95, which has higher affinity to FG Nups than NTF2 transports more efficiently [184]. These results indicate that binding between transport receptors and grafted FG Nups are essential to facilitate transport, resembling the native situation.

Solid-state nanopores, which more accurately recapitulate the dimensions of native NPCs were developed into artificial NPCs by Kowalczyk and colleagues [185]. Size controlled perforation (40 nm) in a silicon nitride (SiN) membrane was achieved by means of a focused transmission electron microscope (TEM) beam. Subsequently, ionic current measurements showed that Kapβ1 exhibits a dwell time of approximately 5 ms in artificial NPCs functionalized with either Nup98 or Nup153 (Fig 4.1b) [190] These measurements further suggest that the FG Nup layer covers up to 25 nm of the pore diameter but cannot cover the pore fully. The density of Nups is estimated to be 1 Nup per 50 nm^2 but grafting is random.

Ion conductance measurements have also been used to study DNA translocation across synthetic nanopores [186]. Since DNA is highly charged, it is driven linearly through the nanopore by an electric field. Single stranded DNA (ssDNA) can translocate through small nanopores (≈2 nm) whereas double stranded DNA (dsDNA) is blocked. While ion conductance measurements have provided numerous insights into the mechanisms of transport, they also have technical limitations. Structural information is missing and the ion current provides indirect information [187].

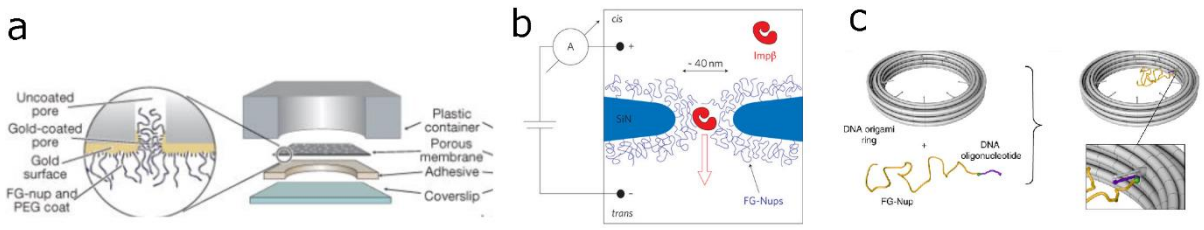

Fig 4.1 Schematic of porous membrane nanopore. (a) Figure reproduced from Jovanovic-Tailsman *et al*. [184] (b) Schematic of SiN Nanopore measured by ion conductance. Figure reproduced from Kowalczyk *et al*. [185] (c) Schematic of DNA origami nanopore. Figure reproduced from Ketterer *et al*. [188].

The number and position of grafted FG Nups can be precisely controlled through the use of oligonucleotide or thiol-maleimide linkage between FG Nups and DNA origami ring [188, 189] (Fig 4.1c). The number of grafted FG Nups are increased step by step and they are projecting inwardly. FG Nups behavior was then studied by electron microscopy (EM), ion-conductance measurements, molecular dynamics simulation and AFM. Central feature made of hydrophobic FG repeats and empty pore of hydrophilic mutant Nsp1-5S are shown by cryo-EM and negative staining TEM [189] (Fig 4.2a). Molecular dynamics simulation provided density distribution of FG Nups (Fig 4.2b). AFM shows FG Nups rearrangements but frame rate 1.6 seconds are not enough to capture dynamics [189]. Cryo-EM, TEM and AFM can therefore provide limited structural or indirect information.

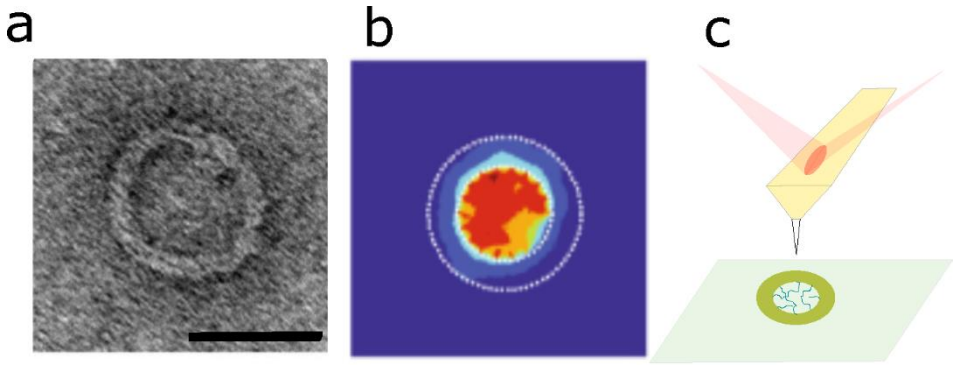

Fig 4.2 DNA nano ring containing Nsp1. (a) Negative staining TEM of DNA nano ring with Nsp1. Scale bar, 50 nm Figure reproduced from Fisher *et al*. [189] (b) Time-averaged mass densities inside of DNA ring obtained by MD simulation. Nsp1 are used for simulation. Figure reproduced from Ketterer *et al*. (c) Schematic of HS-AFM probing nanopore

As shown in Chapter Three, HS-AFM resolves FG Nup behavior within native NPCs and likewise can be used to monitor confined polymer dynamics directly in nanopores. Here, I employ HS-AFM to artificial nanopore-like geometries (Fig 4.2c). In section 4.3, PEG grafted

nanocave which mimic NPC was studied. In section 4.4, FG repeats of Nup62 grafted gold nanorings were studied.

4.2 Theory and Background

4.2.1 Free Polymers in Solution

In polymer physics, polymer chains are divided in subunits called Kuhn monomers, which can contain multiple chemical subunits. For example, Vovk *et al.* [190] define FG Nup Kuhn monomers as 0.4 – 1.6 nm (up to four amino acids) long segments. A chain is thought to be made of correlation blobs containing *n* number of Kuhn monomers of length *b* (total number of Kuhn monomers of the entire FG Nup is N). The radius of gyration R of a free polymer depends on the solubility of the polymer in the solvent.

In a good solvent, the overall repulsion between monomers is larger than their attraction and the polymers are swollen. According to the Flory theory, R in a good solvent is given by

$$R_{good} \approx b(v/b^3)^{2\nu-1} N^{\nu} \approx b(v/b^3)^{0.18} N^{0.588} \qquad (4.1)$$

where ν is the Flory parameter (ν = 3/5 for a good solvent).

In a Theta solvent, the attraction between monomers is identical to interaction between monomers and solvents and the polymers behave like ideal random coils. The radius can then be written

$$R_{theta} \approx bN^{\nu} \approx bN^{0.5} \qquad (4.2)$$

In a poor solvent, attraction between monomers becomes larger than the repulsion, thus polymer chains are collapsed and the radius is given as

$$R_{poor} \approx |v|^{-1/3} b^2 N^{1/3} \qquad (4.3)$$

Note that energy in single blob is small but the cumulative interaction is larger than thermal energy that alter the overall conformation [191].

4.2.2 End Grafted Polymers in Solution

End grafted polymer chains change their conformation depending on the grafting density σ. Polymers form a half-spherical conformation (Fig 4.3a) when the grafting distance g is larger than twice their radius (g > 2R). When g becomes smaller than twice the radius (g<2R), the polymers repel each other and extend. In this extended brush-like conformation, the diameter of each blob is essentially the same as the grafting distance between single polymer chains (Fig. 4.3b). The free energy of a polymer depends on the conformation of the polymer chain. The total free energy of a polymer chain in a densely grafted brush is then given by the sum of

the free energy of all blobs F_{all} and the energy due to overlapping blobs, the excluded volume interaction $F_{ev.}$

The number of blobs in chain is $N_b = h/g$ and the free energy per blob is k_BT. h is the height of monomer. Therefore, the free energy of all blobs is

$$F_{all} \approx k_BTN_b = k_BThg^{-1} \qquad (4.4)$$

The number of blobs is the number of Kuhn monomers in the entire chain divided by number of Kuhn monomers in one blob ($N_b = Nn^{-1}$). The n segments within a blob are assumed to behave like ideal random coils and therefore

$$g \approx bn^{0.5}$$

The number of Kuhn monomers in one blob is hence given by

$$n \approx g^2b^{-2}$$

Therefore, the height h can be written as

$$h \approx gN_b = gNn^{-1} \approx Nb^2g^{-1} \qquad (4.5)$$

By inserting (4.5) into (4.4) we obtain the free energy of all blobs

$$F_{all} = k_BTh^2N^{-1}b^{-2} \qquad (4.6)$$

Excluded volume contributes extra energy for each blob. The occupied volume

$$\varphi \approx N\sigma h^{-1}v^{-1} \quad (4.7)$$

Probability of a second monomer in the excluded volume of first monomer is $v\varphi$. The excluded energy is

$$F_{ev} \approx k_BTNv\varphi \approx k_BTvN^2\sigma h^{-1} \quad (4.8)$$

Thereby total energy of entire polymer is

$$F_{total} = F_{all} + F_{ev}$$

$$\approx k_BT(h^2N^{-1}b^{-2} + vN^2\sigma h^{-1}) \qquad (4.9)$$

With lower grafting distance, polymer chain becomes higher. Thus, polymer chain height is density dependent,

$$h_s / h_0 = \sigma^n \qquad (4.10)$$

For example, in the case of poly(methyl methacrylate) (PMMA), $n \approx 0.33$ in moderate density and $n \approx 0.60$ in high density [192].

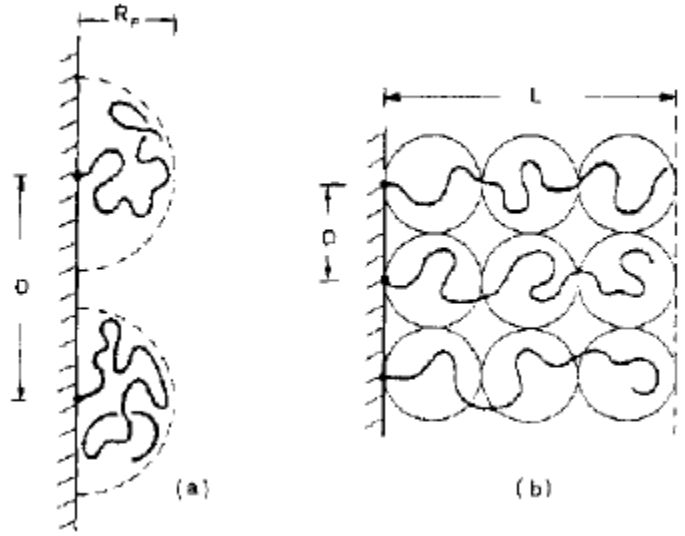

Fig 4.3 Schematics of end grafted polymer in a good solvent. (a) Polymers grafted sparsely forming a mushroom. (b) Densely grafted polymer forming a brush layer. Figure reproduced from de Gennes [193]

4.3 Nano cave with PEG

4.3.1 Result

Confined PEG in nano cave in PBS is observed by HS-AFM. Data shows that 20 kDa PEG form barrier over the cave but 2 kDa PEG only form barrier around rim of the cave. Bare ring shows entirely empty hole (Fig 4.4 a). This may be explained by the contour length of PEG, which is 13-15 nm in the 2 kDa case and 128-150 nm in the 20 kDa case [194]. For the quantitative analysis, z axis MSD are calculated at center, edge and rim (edge2) of the cave. From the fitted curve, limit of displacement Lz are calculated (Fig 4.4 b,c). 20 kDa PEG has higher Lz and Lz increases when it is close to the edge of cave due to higher density of grafted PEG.

Table 4.1: Mean square displacement limit in the z axis.

	center	edge	Edge2	Plane
Bare (nm)	0.447	0.563	0.519	0.831
2kDa (nm)	0.664 ± 0.0492	1.14 ± 0.122	1.20 ± 0.189	2.19 ± 0.502
20kDa (nm)	0.791 ± 0.346	0.855 ± 0.469	1.09 ± 0.532	1.34 ± 0.375

For a more quantitative comparison, a z axis displacement from mean value of central area (10 x 10 pixels) is shown by histogram. Gaussian fits for each histogram give $\sigma_{2kDa} = 0.40$ and $\sigma_{20kDa} = 0.57$. This also suggests that 20 kDa PEG forms a firmer barrier that interferes with

the cantilever oscillation at central area than 2 kDa PEG. In comparison, 2 kDa PEG has firmer barrier at the channel edge.

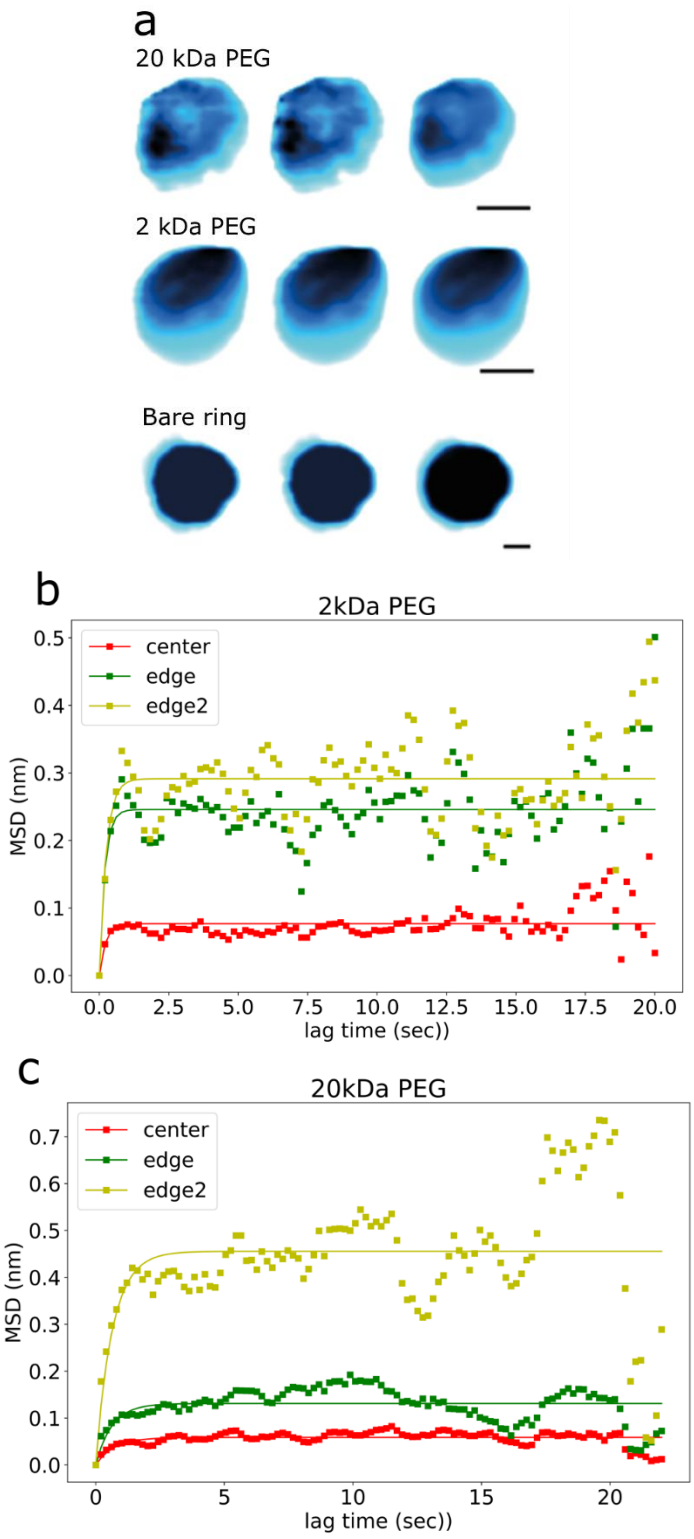

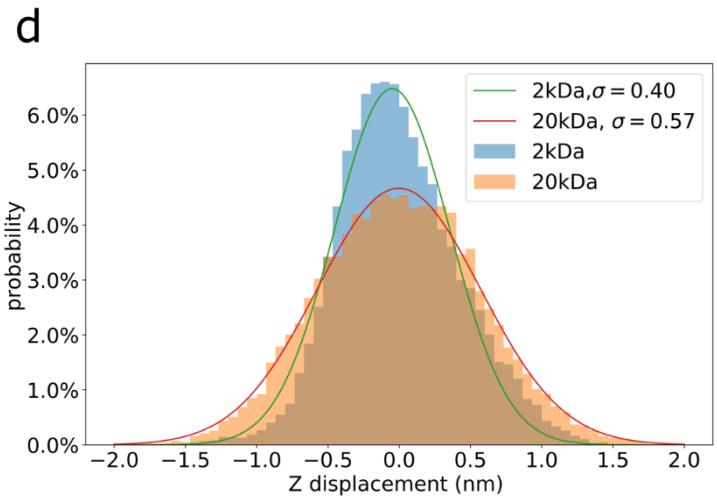

Fig 4.4 HS-AFM images of nanocaves. (a) High speed AFM data of nanocaves with 20 kDa PEG, 2 kDa PEG or no PEG. Characteristic line profiles (averaged in bold) are shown together with snapshot and time averaged images. Scale bars are 30 nm. (b) MSDz curve of 2 kDa PEG (c) MSDz curve of 20 kDa PEG (d) Histogram of displacement of z axis, 2 kDa and 20 kDa.

4.4 Nanorings with FG Nups

4.4.1 Characterization of Surface Roughness

Gold nanorings, which have similar diameter as NPCs, were used to investigate dynamics of Nup62 brushes confined to 3D nanoscale objects. Height of bare gold ring and Nup62 grafted gold ring from glass substrate are 18.9 ± 1.81 nm and 22.4 ± 3.54 nm respectively. 9 different gold rings are counted. Height difference due to Nup62 is 3.54 nm, which shows similar value to hydrodynamics radius of Nup62 3.7 ± 1.7 nm [68]. On bare gold ring, sputtered gold blobs are clearly seen but Nup62 grafted nanoring becomes hairy.

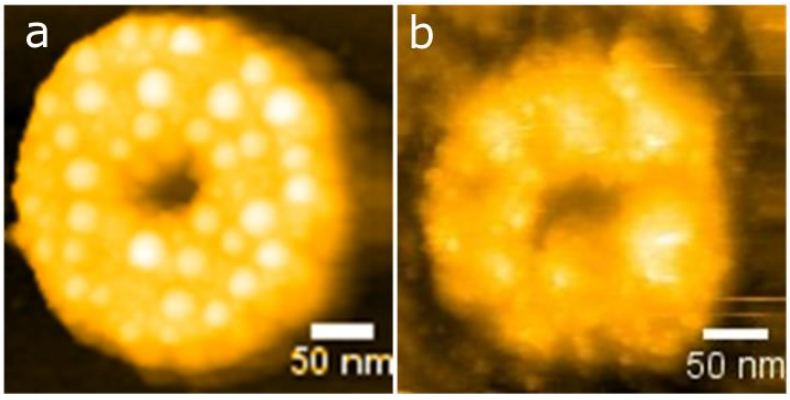

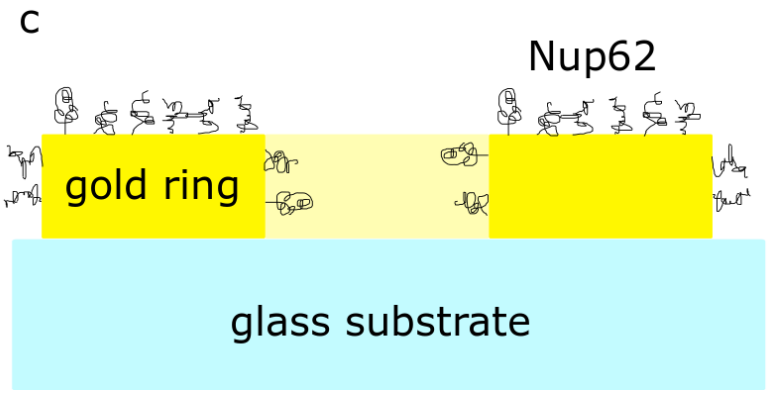

Fig 4.5 HS-AFM image of representative gold ring. (a) Bare gold ring. (b) Gold ring with Nup62. (c) Cartoon illustrating gold ring and end-grafted Nup62

4.4.2 Mean Square Displacement of FG Nups in Z axis

Interestingly, HS-AFM shows similar FG Nup behavior within the nanoring as compared to native NPCs (see Chapter Three). Indeed, the FG Nups are dynamic and form metastable entanglements in sub hundred milliseconds (Fig 4.6a). For the quantitative analysis of FG Nups dynamics, mean square displacement in z axis is calculated. Area used for MSDz calculation is shown in Fig 4.6b. MSDz curve is shown (Fig 4.6c, d). MSD curve is very steep in the beginning due to the fast dynamics of FG Nups. Limit of displacement is the smallest in center and larger on the edge. This suggests that FG Nups are more dense and cantilever oscillation is more disturbed on the edge of the pore.

Table 4.2: Z axis displacement limit of Nup62 in gold nanorings.

	center	edge	Edge2
Lz (nm) Nup62	1.12 ± 0.305	1.21 ± 0.294	1.38 ± 0.35
Lz (nm) Bare ring	1.29	N/A	N/A

4.4.3 Z axis displacement dependent on FG Nups barrier

Histogram of displacement is given for direct comparison. z axis displacement from mean value around central area is calculated over 200 frames. Standard deviations of Bare ring and Nup62 grafted ring are 0.46 and 0.62 respectively (Fig 4.6d). Nup62 makes barrier, which interfere cantilever oscillation.

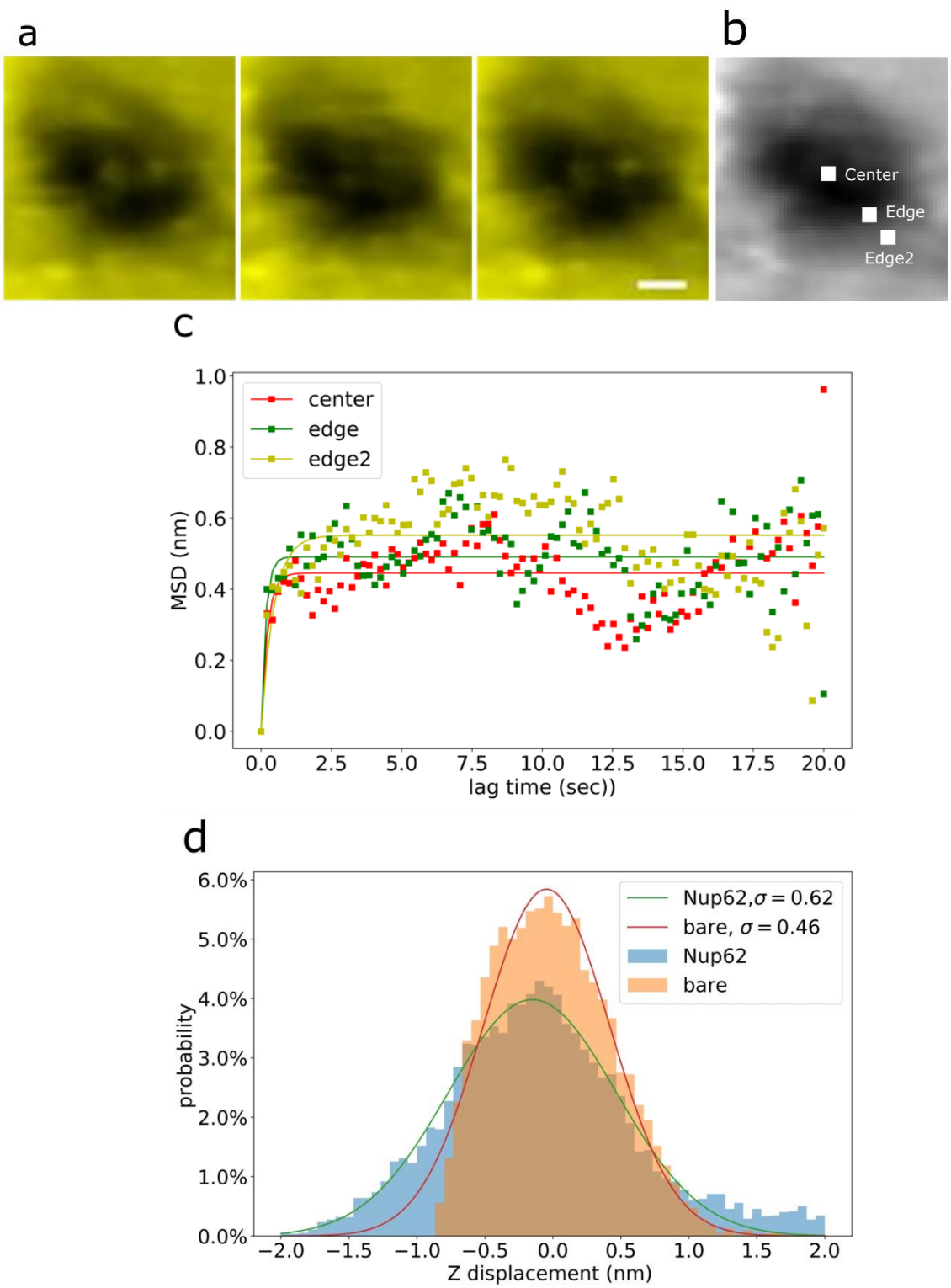

Fig 4.6 HS-AFM images of gold nanoring of Nup62. (a) HS-AFM sequential images. Fluctuation of Nup62 are seen inside of gold ring. Scale bar: 10 nm (b) Area used for MSDz analysis is highlighted by square. (c) MSDz curves (dotted line) and its fitting curve (line). Lz value is calculated from plateau. (d) Histogram of z axis displacement.

4.5 Discussion

20 kDa PEG Lz at center (1.05 nm) is relatively high because stretched PEG chains repel the motion of cantilever. On the other hand, 2 kDa PEG Lz at center is low because contour

length of 2 kDa PEG is only 13 – 15 nm and cantilever oscillation is nearly free oscillation. At the edge of the cave, 2 kDa PEG Lz is higher than 20 kDa PEG Lz because grafting density of 2 kDa is higher.

In conclusion, both confined FG Nups and PEG show barrier behavior inside of channel. Barrier depends on the diameter of the channel, polymer length and density as explained in comparison of 2 kDa and 20 kDa PEG. Nup62 shows comparable behavior to PEG and its size is identical to 20 kDa PEG.

4.6 Materials and Method

4.6.1 Nup62

A 23 kDa cysteine-modified full length FG domain of Nup62 (aa 1-240) with a reported hydrodynamic radius of 3.7 ± 1.7 nm was cloned, expressed and purified as described previously [143].

4.6.2 Poly(ethylene glycol) PEG

Thiol-terminated 2 kDa and 20 kDa poly(ethylene glycol) were used in this experiment. 2 kDa PEG and 20 kDa PEG are expressed as $H(OCH_2CH_2)_{44}OH$ and $H(OCH_2CH_2)_{455}OH$ respectively. The contour lengths are 13-15 nm and 128-150 nm for 2kDa and 20 kDa respectively [194]. Hydrodynamic radii are 1.15 ± 0.150 nm and 4.65 ± 1.20 nm for 2 kDa and 20 kDa respectively.

4.6.3 Nano Cave Fabrication

Nanocave was prepared by Gustav Emilsson (Chalmers University of Technology, Sweden) as described in [194]. Briefly, colloidal self-assembly was used to produce a short-range ordered monolayer on silica, where each colloid forms the template for each pore. A structure referred to as “nanocaves” is obtained by dipping the sample in buffered oxide etch (15% HF) for ~40 s in order to isotopically etch ~100 nm of the underlying glass, thereby creating a suspended gold film [194, 195]. Colloidal self-assembly was used to produce a short-range ordered monolayer on different supports, where each colloid in the end gives rise to one pore. Oxygen plasma was then used to tune the diameter as previously described. Next, 30 nm gold and 20 nm alumina was deposited and the colloids were removed by rubbing the surface in liquid. Diameter of nano cave used for further analysis is 72.8 (± 4.99) nm [196].

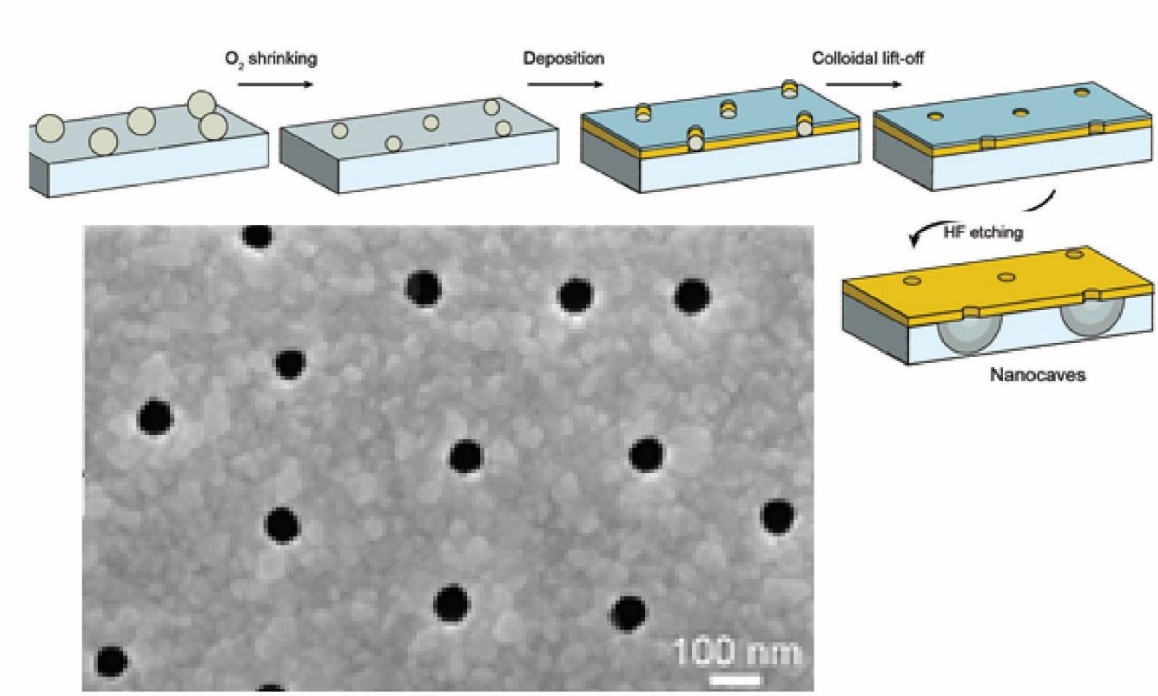

Fig 4.7 Procedure to make nano cave. SEM images of gold plane with nano cave. Image reproduced from Emilsson *et al.* (2018) [194].

4.6.4 Sample Cleaning and Nanostructure Functionalization

Sample is first cleaned by RCA1 solution. When goldring is still covered by debris, it needs to be cleaned further by cleaning1. RCA1 solution is made of 5:1:1 = H_2O:NH_4OH(30%):H_2O_2(30%) [197]. H_2O mixed with NH_4OH is first heated to 65°C, afterward H_2O_2 is added. RCA1 solution start bubbling after a few minutes, samples are immersed for 10 minutes.

Cleaning1 is step washing process using acidic and basic solution. Sample is sonicated in listed solutions for 10 minutes each accordingly. 1 M NaOH, 1 M HCl, 1 M NaOH, 1 M HCl, 100% ethanol. Afterward, sample surface is dried by nitrogen blow and exposed to UV Ozone for 45 minutes. At last, sample is again sonicated in 100% ethanol for 10 minutes and dried by nitrogen blow. Sample needs to be functionalized immediately after cleaning.

Clean gold ring sample is incubated in 1 μM Nup62 in PBS for one hour. Before HS-AFM observation, sample surface is rinsed with 10 μl PBS. FG Nups are tethered to gold surface due to its conductivity.

4.6.5 Data Analysis

Before the dynamics analysis, XYZ drift compensation is computed. XY drift compensation is described in chapter 3. For the Z axis drift compensation, lowest heights in each frame are

brought to zero. Every pixel in the frame moved same pixels in Z axis accordingly. 16 pixels (4x4 square) are selected for the mean square displacement calculation. MSD_z of selected area are calculated using

$$MSD_z = 1/(N-1) \sum^{N}_{n=1} (z[n:N] - z[0:N-n])^2 \quad (4.11)$$

Where N is the total frame numbers for displacement, z is displacement vector. MSD curve are fitted using

$$MSD_z(t) = L_z^2 /6 - 16L_z^2\pi^{-4} \sum^{N}_{n=1,3,5} n^{-4} \exp(-n^2 \pi^2 D_z t L_z^{-2}) \quad (4.12)$$

Where L_z is limit of displacement and D_z is diffusion coefficient. L_z value is extracted from plateau value of $MSD_z = L_z^2/6$. Z axis displacement at the center are counted and shown by histogram. Normalized value is shown as percentage at Y axis.

Z axis displacements of center area (10 x 10 pixels square) are calculated and plotted as histogram. 200 frames 100 pixels are used. All calculations are performed by custom Python script. I wrote the script based on the script from Adam Mazur.

Chapter 5

Conclusions and Outlook

5 Conclusions and Outlook

5.1 Conclusions

Overall, this thesis provides novel insights into the NPC and biomimetic nanopore systems as visualized by HS-AFM. In chapter 2, I explained how HS-AFM was able to capture protein dynamics and, in chapter 3, I showed how we applied HS-AFM to study FG-Nup dynamics within native *Xenppus laevis* NPCs. Extensions of the HS-AFM application to cells or nuclei can be implemented by installing fluorescent blue light to illuminate GFP-tagged kapβ1 [118].

Indeed, there has been a long-standing debate over the NPC-gating mechanism and several models have been proposed primarily based on *in vitro* analysis. By directly visualizing the dynamics of FG-Nups, we have found that the FG Nups fluctuate dynamically while still forming metastable entanglements within the central channel. In doing so, this work allows us to build a more accurate model of NPC function, which is in line with virtual gating and the polymer brush model. These results provide further insight as to how biomimetic NPCs may be built from FG Nups or synthetic polymers.

5.2 Outlook

Although the dynamics of polymers confined in the nanopore may be investigated using HS-AFM, their lateral motion along channel walls remained inaccessible. Further experimentation could include examining FG Nup dynamics on planar surfaces such as mica. For example, we formed a DOPC-based lipid bilayer and Nsp1 was grafted using Ni-NTA and His-tag (Fig. 5.1). The quantification of lateral diffusion was challenging and to overcome this, I developed a novel analysis method, which is described below. First, distinct Nsp1 “blobs” found in the first frame that are larger than 5x5 pixels were selected (Fig 5.2a). Blobs that were positioned in the same 9 pixels square area in the next frame were recognized as the same blob and their trajectory was drawn (Fig 5.2b) [198]. The diffusion distance of each blob over time was then plotted (Fig 5.2c). Trajectories were categorized depending on their lag time (Fig 5.2 d,e). Our data showed that most of the FG Nups diffuse out of the scan range after 30 frames, whereas 18% of blobs stayed at the same position. Overall, we have developed new analytical methods to study the dynamic properties of FG Nups in native NPC structures using HS-AFM. We envision that further developments of HS-AFM (in combination with fluorescence

microscopy) will allow us to expand our findings to cells and tissues. Furthermore, the tools presented here should also be applicable for studying other polymers.

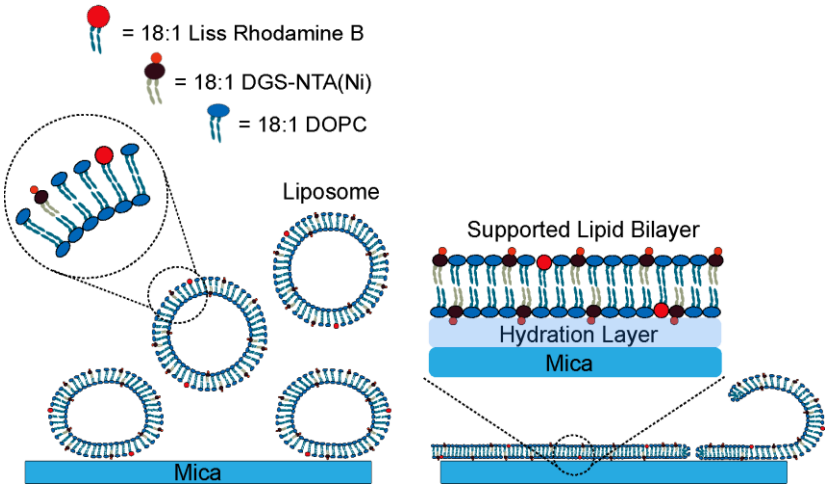

Fig 5.1 Schematic of lipid bilayer on the mica surface.

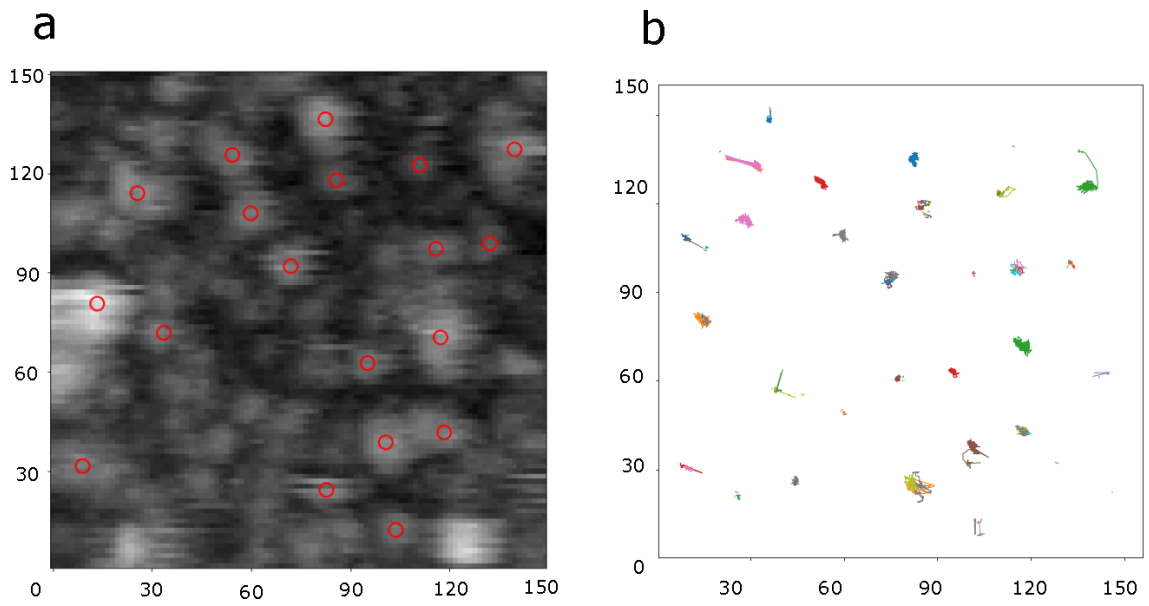

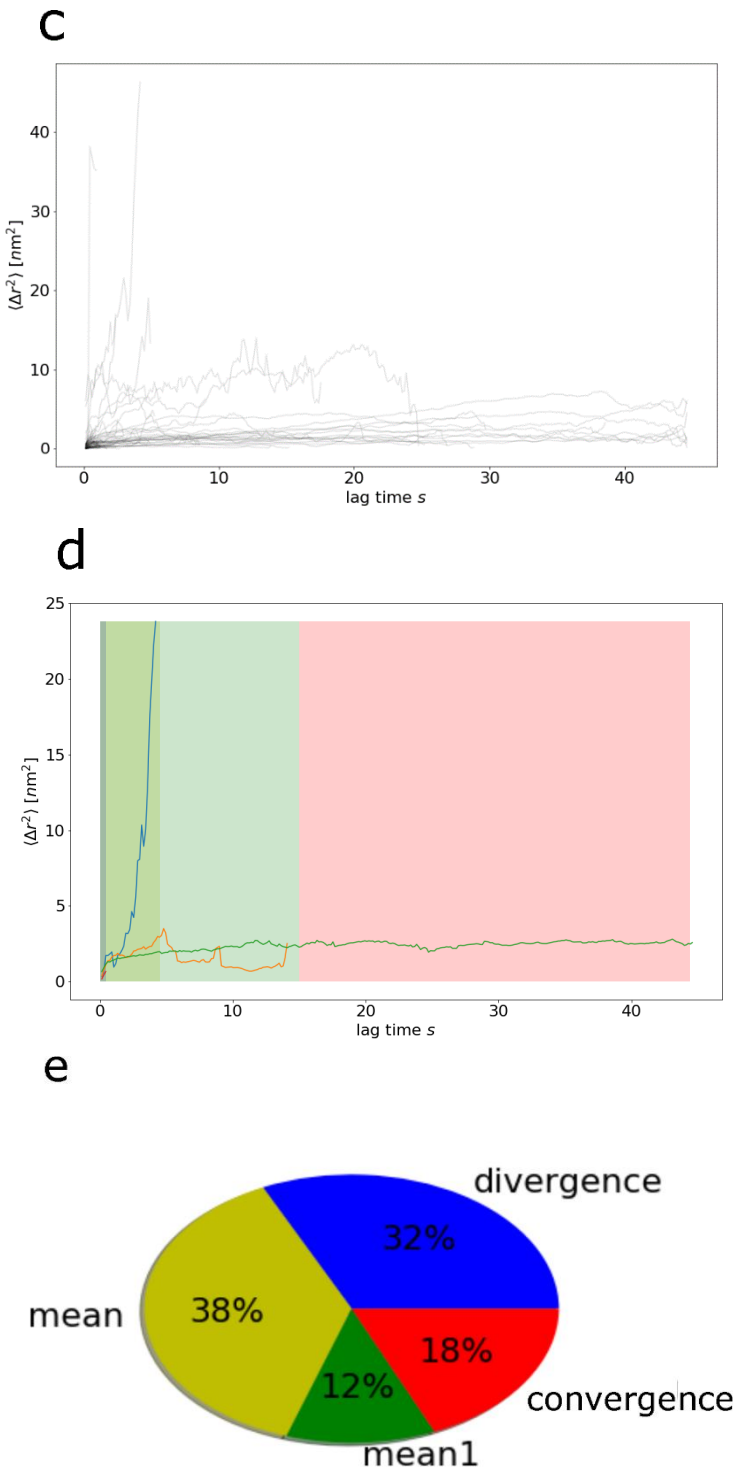

Fig 5.2 (a) Blobs are picked up by the red circles later used for trajectory calculation. Scale in nm for both the axes. (b) Trajectory map over 300 frames. (c) Diffusing distance of each blob is plotted over lag time. (d, e) Diffusing blobs are categorized into four groups: divergence 0-2 frames, mean 3-29 frames, mean 30-99 frames and convergence 100 frames.

References

1. Grunwald, D., R.H. Singer, and M. Rout, *Nuclear export dynamics of RNA-protein complexes.* Nature, 2011. **475**(7356): p. 333-41.
2. Goldfarb, D.S., et al., *Synthetic peptides as nuclear localization signals.* Nature, 1986. **322**(6080): p. 641-4.
3. Wente, S.R. and M.P. Rout, *The nuclear pore complex and nuclear transport.* Cold Spring Harb Perspect Biol, 2010. **2**(10): p. a000562.
4. Aebi, U., et al., *The nuclear lamina is a meshwork of intermediate-type filaments.* Nature, 1986. **323**(6088): p. 560-4.
5. Kiseleva, E., et al., *RNP export is mediated by structural reorganization of the nuclear pore basket.* J Mol Biol, 1996. **260**(3): p. 304-11.
6. Grossman, E., O. Medalia, and M. Zwerger, *Functional architecture of the nuclear pore complex.* Annu Rev Biophys, 2012. **41**: p. 557-84.
7. Gorlich, D. and U. Kutay, *Transport between the cell nucleus and the cytoplasm.* Annu Rev Cell Dev Biol, 1999. **15**: p. 607-60.
8. Strambio-De-Castillia, C., M. Niepel, and M.P. Rout, *The nuclear pore complex: bridging nuclear transport and gene regulation.* Nat Rev Mol Cell Biol, 2010. **11**(7): p. 490-501.
9. Rout, M.P. and G. Blobel, *Isolation of the yeast nuclear pore complex.* J Cell Biol, 1993. **123**(4): p. 771-83.
10. Reichelt, R., et al., *Correlation between structure and mass distribution of the nuclear pore complex and of distinct pore complex components.* J Cell Biol, 1990. **110**(4): p. 883-94.
11. Devos, D., et al., *Simple fold composition and modular architecture of the nuclear pore complex.* Proc Natl Acad Sci U S A, 2006. **103**(7): p. 2172-7.
12. von Appen, A., et al., *In situ structural analysis of the human nuclear pore complex.* Nature, 2015. **526**(7571): p. 140-143.
13. Eibauer, M., et al., *Structure and gating of the nuclear pore complex.* Nat Commun, 2015. **6**: p. 7532.
14. Göttfert, F., et al., *Coaligned Dual-Channel STED Nanoscopy and Molecular Diffusion Analysis at 20 nm Resolution.* Biophysical Journal, 2013. **105**(1): p. L01-L03.
15. Onischenko, E. and K. Weis, *Nuclear pore complex-a coat specifically tailored for the nuclear envelope.* Curr Opin Cell Biol, 2011. **23**(3): p. 293-301.
16. D'Angelo, M.A., et al., *Age-dependent deterioration of nuclear pore complexes causes a loss of nuclear integrity in postmitotic cells.* Cell, 2009. **136**(2): p. 284-95.
17. Siniossoglou, S., et al., *Structure and assembly of the Nup84p complex.* J Cell Biol, 2000. **149**(1): p. 41-54.

18. Kampmann, M. and G. Blobel, *Three-dimensional structure and flexibility of a membrane-coating module of the nuclear pore complex.* Nat Struct Mol Biol, 2009. **16**(7): p. 782-8.
19. Alber, F., et al., *The molecular architecture of the nuclear pore complex.* Nature, 2007. **450**(7170): p. 695-701.
20. Rout, M.P., et al., *The yeast nuclear pore complex: composition, architecture, and transport mechanism.* J Cell Biol, 2000. **148**(4): p. 635-51.
21. Denning, D.P., et al., *Disorder in the nuclear pore complex: the FG repeat regions of nucleoporins are natively unfolded.* Proc Natl Acad Sci U S A, 2003. **100**(5): p. 2450-5.
22. Timney, B.L., et al., *Simple rules for passive diffusion through the nuclear pore complex.* J Cell Biol, 2016. **215**(1): p. 57-76.
23. Solmaz, S.R., et al., *Molecular architecture of the transport channel of the nuclear pore complex.* Cell, 2011. **147**(3): p. 590-602.
24. Chatel, G., et al., *Domain topology of nucleoporin Nup98 within the nuclear pore complex.* J Struct Biol, 2012. **177**(1): p. 81-9.
25. Tompa, P., *Intrinsically unstructured proteins.* Trends in Biochemical Sciences, 2002. **27**(10): p. 527-533.
26. Dunker, A.K., et al., *Function and structure of inherently disordered proteins.* Curr Opin Struct Biol, 2008. **18**(6): p. 756-64.
27. Uversky, V.N. and A.K. Dunker, *Multiparametric analysis of intrinsically disordered proteins: looking at intrinsic disorder through compound eyes.* Anal Chem, 2012. **84**(5): p. 2096-104.
28. Huang, Y. and Z. Liu, *Kinetic advantage of intrinsically disordered proteins in coupled folding–binding process: a critical assessment of the "fly-casting" mechanism.* Journal of molecular biology, 2009. **393**(5): p. 1143-1159.
29. Zhou, H.-X., *Intrinsic disorder: signaling via highly specific but short-lived association.* Trends in Biochemical Sciences, 2012. **37**(2): p. 43-48.
30. Cingolani, G., et al., *Structure of importin-beta bound to the IBB domain of importin-alpha.* Nature, 1999. **399**(6733): p. 221-9.
31. Chook, Y.M. and G. Blobel, *Structure of the nuclear transport complex karyopherin-beta2-Ran x GppNHp.* Nature, 1999. **399**(6733): p. 230-7.
32. Vetter, I.R., et al., *Structural view of the Ran-Importin beta interaction at 2.3 A resolution.* Cell, 1999. **97**(5): p. 635-46.
33. Bayliss, R., T. Littlewood, and M. Stewart, *Structural basis for the interaction between FxFG nucleoporin repeats and importin-beta in nuclear trafficking.* Cell, 2000. **102**(1): p. 99-108.
34. Milles, S., et al., *Plasticity of an ultrafast interaction between nucleoporins and nuclear transport receptors.* Cell, 2015. **163**(3): p. 734-45.

35. Cronshaw, J.M., et al., *Proteomic analysis of the mammalian nuclear pore complex.* J Cell Biol, 2002. **158**(5): p. 915-27.
36. Peleg, O. and R.Y. Lim, *Converging on the function of intrinsically disordered nucleoporins in the nuclear pore complex.* Biol Chem, 2010. **391**(7): p. 719-30.
37. Fernandez-Martinez, J., et al., *Structure and Function of the Nuclear Pore Complex Cytoplasmic mRNA Export Platform.* Cell, 2016. **167**(5): p. 1215-1228.e25.
38. Jeudy, S. and T.U. Schwartz, *Crystal structure of nucleoporin Nic96 reveals a novel, intricate helical domain architecture.* J Biol Chem, 2007. **282**(48): p. 34904-12.
39. Krull, S., et al., *Nucleoporins as components of the nuclear pore complex core structure and Tpr as the architectural element of the nuclear basket.* Mol Biol Cell, 2004. **15**(9): p. 4261-77.
40. Fahrenkrog, B., et al., *Domain-specific antibodies reveal multiple-site topology of Nup153 within the nuclear pore complex.* Journal of structural biology, 2002. **140**(1-3): p. 254-267.
41. Smythe, C., H.E. Jenkins, and C.J. Hutchison, *Incorporation of the nuclear pore basket protein nup153 into nuclear pore structures is dependent upon lamina assembly: evidence from cell-free extracts of Xenopus eggs.* Embo j, 2000. **19**(15): p. 3918-31.
42. Matsuura, Y., et al., *Structural basis for Nup2p function in cargo release and karyopherin recycling in nuclear import.* Embo j, 2003. **22**(20): p. 5358-69.
43. Frosst, P., et al., *Tpr is localized within the nuclear basket of the pore complex and has a role in nuclear protein export.* J Cell Biol, 2002. **156**(4): p. 617-30.
44. Ma, J. and W. Yang, *Three-dimensional distribution of transient interactions in the nuclear pore complex obtained from single-molecule snapshots.* Proc Natl Acad Sci U S A, 2010. **107**(16): p. 7305-10.
45. Siebrasse, J.P. and R. Peters, *Rapid translocation of NTF2 through the nuclear pore of isolated nuclei and nuclear envelopes.* EMBO Rep, 2002. **3**(9): p. 887-92.
46. Neville, M. and M. Rosbash, *The NES-Crm1p export pathway is not a major mRNA export route in Saccharomyces cerevisiae.* Embo j, 1999. **18**(13): p. 3746-56.
47. Sun, C., et al., *Choreography of importin-alpha/CAS complex assembly and disassembly at nuclear pores.* Proc Natl Acad Sci U S A, 2013. **110**(17): p. E1584-93.
48. Mahajan, R., et al., *A small ubiquitin-related polypeptide involved in targeting RanGAP1 to nuclear pore complex protein RanBP2.* Cell, 1997. **88**(1): p. 97-107.
49. Fried, H. and U. Kutay, *Nucleocytoplasmic transport: taking an inventory.* Cell Mol Life Sci, 2003. **60**(8): p. 1659-88.
50. Hutten, S., et al., *The nuclear pore component Nup358 promotes transportin-dependent nuclear import.* J Cell Sci, 2009. **122**(Pt 8): p. 1100-10.

51. Gorlich, D., et al., *Identification of different roles for RanGDP and RanGTP in nuclear protein import.* Embo j, 1996. **15**(20): p. 5584-94.
52. Cingolani, G., et al., *Molecular basis for the recognition of a nonclassical nuclear localization signal by importin beta.* Mol Cell, 2002. **10**(6): p. 1345-53.
53. Moroianu, J., G. Blobel, and A. Radu, *Nuclear protein import: Ran-GTP dissociates the karyopherin alphabeta heterodimer by displacing alpha from an overlapping binding site on beta.* Proc Natl Acad Sci U S A, 1996. **93**(14): p. 7059-62.
54. Matsuura, Y. and M. Stewart, *Nup50/Npap60 function in nuclear protein import complex disassembly and importin recycling.* Embo j, 2005. **24**(21): p. 3681-9.
55. Fuxreiter, M., et al., *Disordered proteinaceous machines.* Chem Rev, 2014. **114**(13): p. 6806-43.
56. Ribbeck, K. and D. Gorlich, *Kinetic analysis of translocation through nuclear pore complexes.* Embo j, 2001. **20**(6): p. 1320-30.
57. Frey, S., R.P. Richter, and D. Gorlich, *FG-rich repeats of nuclear pore proteins form a three-dimensional meshwork with hydrogel-like properties.* Science, 2006. **314**(5800): p. 815-7.
58. Frey, S. and D. Gorlich, *A saturated FG-repeat hydrogel can reproduce the permeability properties of nuclear pore complexes.* Cell, 2007. **130**(3): p. 512-23.
59. Milles, S., et al., *Facilitated aggregation of FG nucleoporins under molecular crowding conditions.* EMBO reports, 2013. **14**(2): p. 178-183.
60. Macara, I.G., *Transport into and out of the nucleus.* Microbiol Mol Biol Rev, 2001. **65**(4): p. 570-94, table of contents.
61. Lim, R.Y., et al., *Flexible phenylalanine-glycine nucleoporins as entropic barriers to nucleocytoplasmic transport.* Proc Natl Acad Sci U S A, 2006. **103**(25): p. 9512-7.
62. Lim, R.Y., et al., *Nanomechanical basis of selective gating by the nuclear pore complex.* Science, 2007. **318**(5850): p. 640-3.
63. Peters, R., *Translocation through the nuclear pore complex: selectivity and speed by reduction-of-dimensionality.* Traffic, 2005. **6**(5): p. 421-7.
64. Schleicher, K.D., et al., *Selective transport control on molecular velcro made from intrinsically disordered proteins.* Nature Nanotechnology, 2014. **9**: p. 525.
65. Yamada, J., et al., *A bimodal distribution of two distinct categories of intrinsically disordered structures with separate functions in FG nucleoporins.* Mol Cell Proteomics, 2010. **9**(10): p. 2205-24.
66. Akey, C.W., *Interactions and structure of the nuclear pore complex revealed by cryo-electron microscopy.* J Cell Biol, 1989. **109**(3): p. 955-70.

67. Unwin, P.N. and R.A. Milligan, *A large particle associated with the perimeter of the nuclear pore complex.* J Cell Biol, 1982. **93**(1): p. 63-75.
68. Kapinos, L.E., et al., *Karyopherin-centric control of nuclear pores based on molecular occupancy and kinetic analysis of multivalent binding with FG nucleoporins.* Biophys J, 2014. **106**(8): p. 1751-62.
69. Ma, J., et al., *Self-regulated viscous channel in the nuclear pore complex.* Proc Natl Acad Sci U S A, 2012. **109**(19): p. 7326-31.
70. Kapinos, L.E., et al., *Karyopherins regulate nuclear pore complex barrier and transport function.* J Cell Biol, 2017. **216**(11): p. 3609-3624.
71. Miao, L. and K. Schulten, *Transport-related structures and processes of the nuclear pore complex studied through molecular dynamics.* Structure, 2009. **17**(3): p. 449-59.
72. Gamini, R., et al., *Assembly of Nsp1 nucleoporins provides insight into nuclear pore complex gating.* PLoS Comput Biol, 2014. **10**(3): p. e1003488.
73. Osmanovic, D., et al., *Bistable collective behavior of polymers tethered in a nanopore.* Phys Rev E Stat Nonlin Soft Matter Phys, 2012. **85**(6 Pt 1): p. 061917.
74. Schoch, R.L., L.E. Kapinos, and R.Y.H. Lim, *Nuclear transport receptor binding avidity triggers a self-healing collapse transition in FG-nucleoporin molecular brushes.* Proceedings of the National Academy of Sciences, 2012. **109**(42): p. 16911-16916.
75. Wagner, Raphael S., et al., *Promiscuous Binding of KaryopherinΒ1 Modulates FG Nucleoporin Barrier Function and Expedites NTF2 Transport Kinetics.* Biophysical Journal, 2015. **108**(4): p. 918-927.
76. Kramer, A., et al., *Atomic force microscopy visualises a hydrophobic meshwork in the central channel of the nuclear pore.* Pflugers Arch, 2008. **456**(1): p. 155-62.
77. Ma, J., A. Goryaynov, and W. Yang, *Super-resolution 3D tomography of interactions and competition in the nuclear pore complex.* Nat Struct Mol Biol, 2016. **23**(3): p. 239-47.
78. Bestembayeva, A., et al., *Nanoscale stiffness topography reveals structure and mechanics of the transport barrier in intact nuclear pore complexes.* Nat Nanotechnol, 2015. **10**(1): p. 60-64.
79. Binning, G., et al., *SURFACE STUDIES BY SCANNING TUNNELING MICROSCOPY.* Physical Review Letters, 1982. **49**(1): p. 57-61.
80. Binnig, G., C.F. Quate, and C. Gerber, *Atomic force microscope.* Physical review letters, 1986. **56**(9): p. 930.
81. Butt, H.-J., B. Cappella, and M. Kappl, *Force measurements with the atomic force microscope: Technique, interpretation and applications.* Surface science reports, 2005. **59**(1-6): p. 1-152.

82. Evans, E.A. and D.A. Calderwood, *Forces and bond dynamics in cell adhesion.* Science, 2007. **316**(5828): p. 1148-1153.
83. Helenius, J., et al., *Single-cell force spectroscopy.* J Cell Sci, 2008. **121**(11): p. 1785-91.
84. Oesterhelt, F., et al., *Unfolding pathways of individual bacteriorhodopsins.* Science, 2000. **288**(5463): p. 143-6.
85. Grandbois, M., et al., *Affinity imaging of red blood cells using an atomic force microscope.* J Histochem Cytochem, 2000. **48**(5): p. 719-24.
86. Gad, M., A. Itoh, and A. Ikai, *Mapping cell wall polysaccharides of living microbial cells using atomic force microscopy.* Cell Biol Int, 1997. **21**(11): p. 697-706.
87. Chtcheglova, L.A., et al., *Nano-scale dynamic recognition imaging on vascular endothelial cells.* Biophys J, 2007. **93**(2): p. L11-3.
88. Muller, D.J. and Y.F. Dufrene, *Atomic force microscopy: a nanoscopic window on the cell surface.* Trends Cell Biol, 2011. **21**(8): p. 461-9.
89. Dufrêne, Y.F., et al., *Multiparametric imaging of biological systems by force-distance curve–based AFM.* Nature methods, 2013. **10**(9): p. 847.
90. Radmacher, M., et al., *Mapping interaction forces with the atomic force microscope.* Biophysical journal, 1994. **66**(6): p. 2159-2165.
91. Herruzo, E.T., A.P. Perrino, and R. Garcia, *Fast nanomechanical spectroscopy of soft matter.* Nature communications, 2014. **5**: p. 3126.
92. Medalsy, I.D. and D.J. Müller, *Nanomechanical properties of proteins and membranes depend on loading rate and electrostatic interactions.* ACS nano, 2013. **7**(3): p. 2642-2650.
93. Plodinec, M., et al., *The nanomechanical signature of breast cancer.* Nature nanotechnology, 2012. **7**(11): p. 757.
94. Rayment, I., et al., *Three-dimensional structure of myosin subfragment-1: a molecular motor.* Science, 1993. **261**(5117): p. 50-8.
95. Dominguez, R., et al., *Crystal structure of a vertebrate smooth muscle myosin motor domain and its complex with the essential light chain: visualization of the pre-power stroke state.* Cell, 1998. **94**(5): p. 559-71.
96. Houdusse, A., A.G. Szent-Gyorgyi, and C. Cohen, *Three conformational states of scallop myosin S1.* Proc Natl Acad Sci U S A, 2000. **97**(21): p. 11238-43.
97. Smith, C.A. and I. Rayment, *X-ray structure of the magnesium(II).ADP.vanadate complex of the Dictyostelium discoideum myosin motor domain to 1.9 A resolution.* Biochemistry, 1996. **35**(17): p. 5404-17.
98. Shih, W.M., et al., *A FRET-based sensor reveals large ATP hydrolysis-induced conformational changes and three distinct states of the molecular motor myosin.* Cell, 2000. **102**(5): p. 683-94.

99. Forkey, J.N., et al., *Three-dimensional structural dynamics of myosin V by single-molecule fluorescence polarization.* Nature, 2003. **422**(6930): p. 399-404.
100. Rief, M., et al., *Myosin-V stepping kinetics: a molecular model for processivity.* Proc Natl Acad Sci U S A, 2000. **97**(17): p. 9482-6.
101. Mehta, A.D., et al., *Myosin-V is a processive actin-based motor.* Nature, 1999. **400**(6744): p. 590-3.
102. Walker, M.L., et al., *Two-headed binding of a processive myosin to F-actin.* Nature, 2000. **405**: p. 804.
103. Drake, B., et al., *Imaging crystals, polymers, and processes in water with the atomic force microscope.* Science, 1989. **243**(4898): p. 1586-1589.
104. Kasas, S., et al., *Escherichia coli RNA Polymerase Activity Observed Using Atomic Force Microscopy.* Biochemistry, 1997. **36**(3): p. 461-468.
105. Ando, T., et al., *A high-speed atomic force microscope for studying biological macromolecules.* Proc Natl Acad Sci U S A, 2001. **98**(22): p. 12468-72.
106. Ando, T., T. Uchihashi, and T. Fukuma, *High-speed atomic force microscopy for nano-visualization of dynamic biomolecular processes.* Progress in Surface Science, 2008. **83**(7-9): p. 337-437.
107. Kodera, N., et al., *Video imaging of walking myosin V by high-speed atomic force microscopy.* Nature, 2010. **468**(7320): p. 72-6.
108. Ando, T., et al., *High-speed AFM and nano-visualization of biomolecular processes.* Pflugers Arch, 2008. **456**(1): p. 211-25.
109. Ando, T., *High-speed atomic force microscopy.* Microscopy (Oxf), 2013. **62**(1): p. 81-93.
110. Uchihashi, T., N. Kodera, and T. Ando, *Guide to video recording of structure dynamics and dynamic processes of proteins by high-speed atomic force microscopy.* Nature Protocols, 2012. **7**: p. 1193.
111. Kokavecz, J., et al., *Novel amplitude and frequency demodulation algorithm for a virtual dynamic atomic force microscope.* Nanotechnology, 2006. **17**(7): p. S173-7.
112. Kodera, N., H. Yamashita, and T. Ando, *Active damping of the scanner for high-speed atomic force microscopy.* Review of Scientific Instruments, 2005. **76**(5).
113. Kodera, N., M. Sakashita, and T. Ando, *Dynamic proportional-integral-differential controller for high-speed atomic force microscopy.* Review of Scientific Instruments, 2006. **77**(8).
114. Uchihashi, T., et al., *High-speed atomic force microscopy reveals rotary catalysis of rotorless F(1)-ATPase.* Science, 2011. **333**(6043): p. 755-8.
115. Shibata, M., et al., *High-speed atomic force microscopy shows dynamic molecular processes in photoactivated bacteriorhodopsin.* Nat Nanotechnol, 2010. **5**(3): p. 208-12.

116. Miyagi, A., et al., *Visualization of intrinsically disordered regions of proteins by high-speed atomic force microscopy.* Chemphyschem, 2008. **9**(13): p. 1859-66.
117. Watanabe, H., et al., *Wide-area scanner for high-speed atomic force microscopy.* Review of Scientific Instrumts, 2013. **84**(5): p. 053702.
118. Shibata, M., et al., *Long-tip high-speed atomic force microscopy for nanometer-scale imaging in live cells.* Sci Rep, 2015. **5**: p. 8724.
119. Grünwald, D., R.H. Singer, and M. Rout, *Nuclear export dynamics of RNA-protein complexes.* Nature, 2011. **475**(7356): p. 333-341.
120. Popken, P., et al., *Size-dependent leak of soluble and membrane proteins through the yeast nuclear pore complex.* Molecular Biology of the Cell, 2015. **26**(7): p. 1386-1394.
121. Yamada, J., et al., *A bimodal distribution of two distinct categories of intrinsically disordered structures with separate functions in FG nucleoporins.* Mol Cell Proteomics, 2010. **9**: p. 2205-2224.
122. Beck, M., et al., *Nuclear pore complex structure and dynamics revealed by cryoelectron tomography.* Science, 2004. **306**(5700): p. 1387-1390.
123. Stoffler, D., et al., *Cryo-electron tomography provides novel insights into nuclear pore architecture: Implications for nucleocytoplasmic transport.* Journal of Molecular Biology, 2003. **328**(1): p. 119-130.
124. Eibauer, M., et al., *Structure and gating of the nuclear pore complex.* Nature Communications, 2015. **6**: p. 7532.
125. Rout, M.P., et al., *Virtual gating and nuclear transport: the hole picture.* Trends in Cell Biology, 2003. **13**(12): p. 622-628.
126. Rout, M.P., et al., *The yeast nuclear pore complex: Composition, architecture, and transport mechanism.* Journal of Cell Biology, 2000. **148**(4): p. 635-651.
127. Lim, R.Y.H., et al., *Nanomechanical basis of selective gating by the nuclear pore complex.* Science, 2007. **318**(5850): p. 640-3.
128. Lim, R.Y.H., et al., *Flexible phenylalanine-glycine nucleoporins as entropic barriers to nucleocytoplasmic transport.* Proc Natl Acad Sci USA, 2006. **103**(25): p. 9512-9517.
129. Frey, S. and D. Görlich, *A saturated FG-repeat hydrogel can reproduce the permeability properties of nuclear pore complexes.* Cell, 2007. **130**(3): p. 512-523.
130. Hülsmann, B.B., A.A. Labokha, and D. Görlich, *The permeability of reconstituted nuclear pores provides direct evidence for the selective phase model.* Cell, 2012. **150**(4): p. 738-751.
131. Akey, C.W., *Visualization of transport-related configurations of the nuclear-pore transporter.* Biophysical Journal, 1990. **58**(2): p. 341-355.

132. Dange, T., et al., *Autonomy and robustness of translocation through the nuclear pore complex: A single-molecule study.* J Cell Biol, 2008. **183**(1): p. 77-86.
133. Fahrenkrog, B., et al., *Domain-specific antibodies reveal multiple-site topology of Nup153 within the nuclear pore complex.* J Struct Biol, 2002. **140**(1-3): p. 254-267.
134. Stoffler, D., et al., *Calcium-mediated structural changes of native nuclear pore complexes monitored by time-lapse atomic force microscopy.* J Mol Biol, 1999. **287**(4): p. 741-52.
135. Bestembayeva, A., et al., *Nanoscale stiffness topography reveals structure and mechanics of the transport barrier in intact nuclear pore complexes.* Nature Nanotechnology, 2015. **10**(1): p. 60-64.
136. Kramer, A., et al., *Atomic force microscopy visualises a hydrophobic meshwork in the central channel of the nuclear pore.* Pflugers Archiv-European Journal of Physiology, 2008. **456**(1): p. 155-162.
137. Cardarelli, F., L. Lanzano, and E. Gratton, *Capturing directed molecular motion in the nuclear pore complex of live cells.* Proc Natl Acad Sci USA, 2012. **109**: p. 9863-9868.
138. Ma, J., et al., *Self-regulated viscous channel in the nuclear pore complex.* Proc Natl Acad Sci USA, 2012. **109**(19): p. 7326-7331.
139. Ma, J., A. Goryaynov, and W. Yang, *Super-resolution 3D tomography of interactions and competition in the nuclear pore complex.* Nature Structural and Molecular Biology, 2016. **23**: p. 239-247.
140. Uchihashi, T., N. Kodera, and T. Ando, *Guide to video recording of structure dynamics and dynamic processes of proteins by high-speed atomic force microscopy.* Nature Protocols, 2012. **7**(6): p. 1193-1206.
141. Uchihashi, T., et al., *High-speed atomic force microscopy reveals rotary catalysis of rotorless F-1-ATPase.* Science, 2011. **333**(6043): p. 755-758.
142. Chatel, G., et al., *Domain topology of nucleoporin Nup98 within the nuclear pore complex.* Journal of structural biology, 2012. **177**(1): p. 81-9.
143. Kapinos, L.E., et al., *Karyopherin-centric control of nuclear pores based on molecular occupancy and kinetic analysis of multivalent binding with FG nucleoporins.* Biophysical Journal, 2014. **106**(8): p. 1751-1762.
144. Vesenka, J., et al., *Colloidal gold particles as an incompressible atomic-force microscope imaging standard for assessing the compressibility of biomolecules.* Biophysical Journal, 1993. **65**(3): p. 992-997.
145. Chattopadhyay, K., E.L. Elson, and C. Frieden, *The kinetics of conformational fluctuations in an unfolded protein measured by fluorescence methods.* Proceedings of the National Academy of Sciences of the United States of America, 2005. **102**(7): p. 2385-2389.

146. Windisch, B., D. Bray, and T. Duke, *Balls and chains - A mesoscopic approach to tethered protein domains.* Biophysical Journal, 2006. **91**(7): p. 2383-2392.
147. Kusumi, A., Y. Sako, and M. Yamamoto, *Confined lateral diffusion of membrane receptors as studied by single particle tracking (nanovid microscopy). Effects of calcium-induced differentiation in cultured epithelial cells.* Biophysical Journal, 1993. **65**(5): p. 2021-2040.
148. Schmidt, H.B. and D. Görlich, *Nup98 FG domains from diverse species spontaneously phase-separate into particles with nuclear pore-like permselectivity.* Elife, 2015. **4**: p. e04251.
149. Osmanovic, D., et al., *Bistable collective behavior of polymers tethered in a nanopore.* Physical review. E, Statistical, nonlinear, and soft matter physics, 2012. **85**(6 Pt 1): p. 061917.
150. Grünwald, D. and R.H. Singer, *In vivo imaging of labelled endogenous b-actin mRNA during nucleocytoplasmic transport.* Nature, 2010. **467**: p. 604-609.
151. Ando, D., et al., *Nuclear pore complex protein sequences determine overall copolymer brush structure and function.* Biophysical Journal, 2014. **106**(9): p. 1997-2007.
152. Ghavami, A., et al., *Probing the disordered domain of the nuclear pore complex through coarse-grained molecular dynamics simulations.* Biophysical Journal, 2014. **107**(6): p. 1393-1402.
153. Tagliazucchi, M., et al., *Effect of charge, hydrophobicity, and sequence of nucleoporins on the translocation of model particles through the nuclear pore complex.* Proceedings of the National Academy of Sciences of the United States of America, 2013. **110**(9): p. 3363-3368.
154. Gamini, R., et al., *Assembly of Nsp1 nucleoporins provides insight into nuclear pore complex gating.* Plos Computational Biology, 2014. **10**(3): p. e1003488.
155. Mincer, J.S. and S.M. Simon, *Simulations of nuclear pore transport yield mechanistic insights and quantitative predictions.* Proceedings of the National Academy of Sciences of the United States of America, 2011. **108**: p. E351-E358.
156. Peyro, M., et al., *Nucleoporin's like charge regions are major regulators of FG coverage and dynamics inside the nuclear pore complex.* Plos One, 2015. **10**(12): p. e0143745.
157. Ando, T., *High-speed atomic force microscopy.* Microscopy, 2013. **62**(1): p. 81-93.
158. Schmidt, H.B. and D. Görlich, *Transport selectivity of nuclear pores, phase separation, and membraneless organelles.* Trends in Biochemical Sciences, 2016. **41**(1): p. 46-61.
159. Hough, L.E., et al., *The molecular mechanism of nuclear transport revealed by atomic-scale measurements.* eLife, 2015. **4**: p. e10027.
160. Fuxreiter, M., et al., *Disordered proteinaceous machines.* Chem Rev, 2014. **114**(13): p. 6806-6843.
161. Hoh, J.H., *Functional protein domains from the thermally driven motion of polypeptide chains: A proposal.* Proteins-Structure Function and Genetics, 1998. **32**(2): p. 223-228.

162. *Python Software Foundation, Python Language Reference, version 2.7*, in *Python Software Foundation, Python Language Reference, version 2.7*.
163. Hunter, J.D., *Matplotlib: A 2D graphics environment.* Computing in Science & Engineering, 2007. **9**(3): p. 90-95.
164. Lowekamp, B.C., et al., *The Design of SimpleITK.* Frontiers in Neuroinformatics, 2013. **7**: p. 45.
165. van der Walt, S., S.C. Colbert, and G. Varoquaux, *The NumPy Array: A Structure for Efficient Numerical Computation.* Computing in Science & Engineering, 2011. **13**(2): p. 22-30.
166. van der Walt, S., et al., *scikit-image: image processing in Python.* Peerj, 2014. **2**: p. e453.
167. Schindelin, J., et al., *Fiji: an open-source platform for biological-image analysis.* Nature Methods, 2012. **9**(7): p. 676-682.
168. Kramer, A., et al., *Apoptosis leads to a degradation of vital components of active nuclear transport and a dissociation of the nuclear lamina.* Proceedings of the National Academy of Sciences of the United States of America, 2008. **105**(32): p. 11236-11241.
169. Hou, X. and L. Jiang, *Learning from nature: building bio-inspired smart nanochannels.* ACS Nano, 2009. **3**(11): p. 3339-42.
170. Siwy, Z.S. and M. Davenport, *Graphene opens up to DNA.* Nature Nanotechnology, 2010. **5**: p. 697.
171. Vlassiouk, I., et al., *Versatile ultrathin nanoporous silicon nitride membranes.* Proc Natl Acad Sci U S A, 2009. **106**(50): p. 21039-44.
172. van der Heyden, F.H.J., et al., *Power Generation by Pressure-Driven Transport of Ions in Nanofluidic Channels.* Nano Letters, 2007. **7**(4): p. 1022-1025.
173. Goodman, B.E., *Channels active in the excitability of nerves and skeletal muscles across the neuromuscular junction: basic function and pathophysiology.* Adv Physiol Educ, 2008. **32**(2): p. 127-35.
174. Sheng, M. and D.T.S. Pak, *Ligand-Gated Ion Channel Interactions with Cytoskeletal and Signaling Proteins.* Annual Review of Physiology, 2000. **62**(1): p. 755-778.
175. Catterall, W.A., *Structure and Function of Voltage-Gated Ion Channels.* Annual Review of Biochemistry, 1995. **64**(1): p. 493-531.
176. Fernandez, L. and R.E. Hancock, *Adaptive and mutational resistance: role of porins and efflux pumps in drug resistance.* Clin Microbiol Rev, 2012. **25**(4): p. 661-81.
177. Alcaraz, A., et al., *A pH-Tunable Nanofluidic Diode: Electrochemical Rectification in a Reconstituted Single Ion Channel.* The Journal of Physical Chemistry B, 2006. **110**(42): p. 21205-21209.

178. Siwy, Z., et al., *Ion transport through asymmetric nanopores prepared by ion track etching.* Nuclear Instruments and Methods in Physics Research Section B: Beam Interactions with Materials and Atoms, 2003. **208**: p. 143-148.
179. Hou, X., et al., *A pH-gating ionic transport nanodevice: Asymmetric chemical modification of single nanochannels.* Adv Mater, 2010. **22**(22): p. 2440-3.
180. Yameen, B., et al., *Synthetic Proton-Gated Ion Channels via Single Solid-State Nanochannels Modified with Responsive Polymer Brushes.* Nano Letters, 2009. **9**(7): p. 2788-2793.
181. Schepelina, O. and I. Zharov, *PNIPAAM-modified nanoporous colloidal films with positive and negative temperature gating.* Langmuir, 2007. **23**(25): p. 12704-9.
182. Reber, N., et al., *Transport properties of thermo-responsive ion track membranes.* Journal of Membrane Science, 2001. **193**(1): p. 49-58.
183. Caspi, Y., et al., *Synthetic Mimic of Selective Transport Through the Nuclear Pore Complex.* Nano Letters, 2008. **8**(11): p. 3728-3734.
184. Jovanovic-Talisman, T., et al., *Artificial nanopores that mimic the transport selectivity of the nuclear pore complex.* Nature, 2009. **457**(7232): p. 1023-7.
185. Kowalczyk, S.W., et al., *Single-molecule transport across an individual biomimetic nuclear pore complex.* Nat Nanotechnol, 2011. **6**(7): p. 433-8.
186. Heng, J.B., et al., *The electromechanics of DNA in a synthetic nanopore.* Biophys J, 2006. **90**(3): p. 1098-106.
187. Siwy, Z., et al., *Rectification and voltage gating of ion currents in a nanofabricated pore.* Europhys. Lett., 2002. **60**(3): p. 349-355.
188. Ketterer, P., et al., *DNA origami scaffold for studying intrinsically disordered proteins of the nuclear pore complex.* Nat Commun, 2018. **9**(1): p. 902.
189. Fisher, P.D.E., et al., *A Programmable DNA Origami Platform for Organizing Intrinsically Disordered Nucleoporins within Nanopore Confinement.* ACS Nano, 2018. **12**(2): p. 1508-1518.
190. Vovk, A., et al., *Simple biophysics underpins collective conformations of the intrinsically disordered proteins of the Nuclear Pore Complex.* eLife, 2016. **5**: p. e10785.
191. Colby, M.R.a.R.H., *Polymer Physics.* OUP Oxford, 2003.
192. Moh, L.C.H., M.D. Losego, and P.V. Braun, *Solvent Quality Effects on Scaling Behavior of Poly(methyl methacrylate) Brushes in the Moderate- and High-Density Regimes.* Langmuir, 2011. **27**(7): p. 3698-3702.
193. de Gennes, P.G., *Polymers at an interface; a simplified view.* Advances in Colloid and Interface Science, 1987. **27**(3): p. 189-209.
194. Emilsson, G., et al., *Polymer brushes in solid-state nanopores form an impenetrable entropic barrier for proteins.* Nanoscale, 2018. **10**(10): p. 4663-4669.

195. Xiong, K., G. Emilsson, and A.B. Dahlin, *Biosensing using plasmonic nanohole arrays with small, homogenous and tunable aperture diameters.* Analyst, 2016. **141**(12): p. 3803-10.
196. Malekian, B., et al., *Fabrication and Characterization of Plasmonic Nanopores with Cavities in the Solid Support.* Sensors (Basel), 2017. **17**(6).
197. Dekker, C., *Solid-state nanopores.* Nat Nanotechnol, 2007. **2**(4): p. 209-15.
198. Crocker, J.C. and D.G. Grier, *Methods of digital video microscopy for colloidal studies.* Journal of colloid and interface science, 1996. **179**(1): p. 298-310.

Appendix

Appendix
Appendix Chapter 2

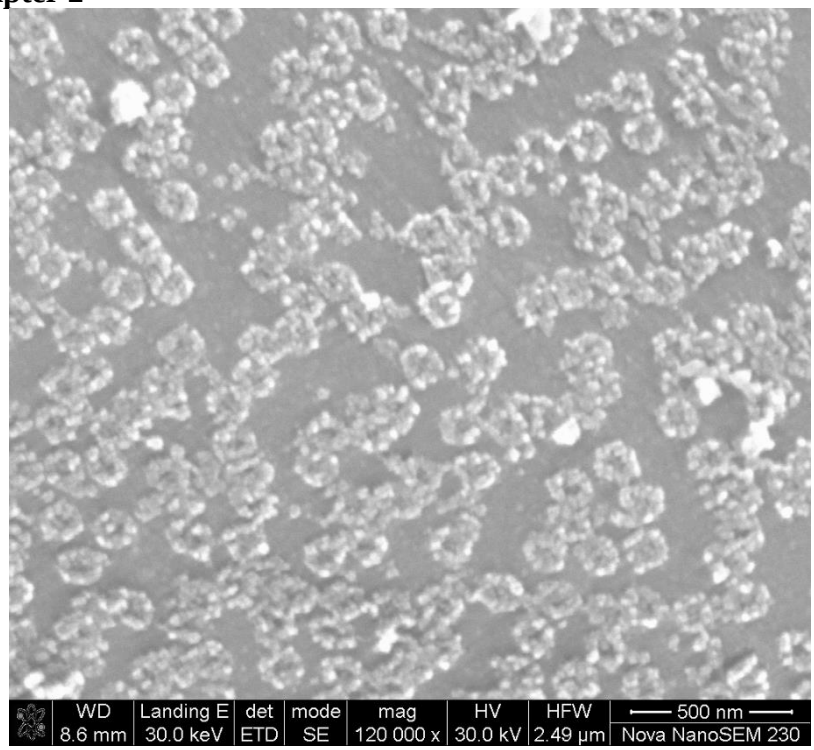

Cytoplasmic side

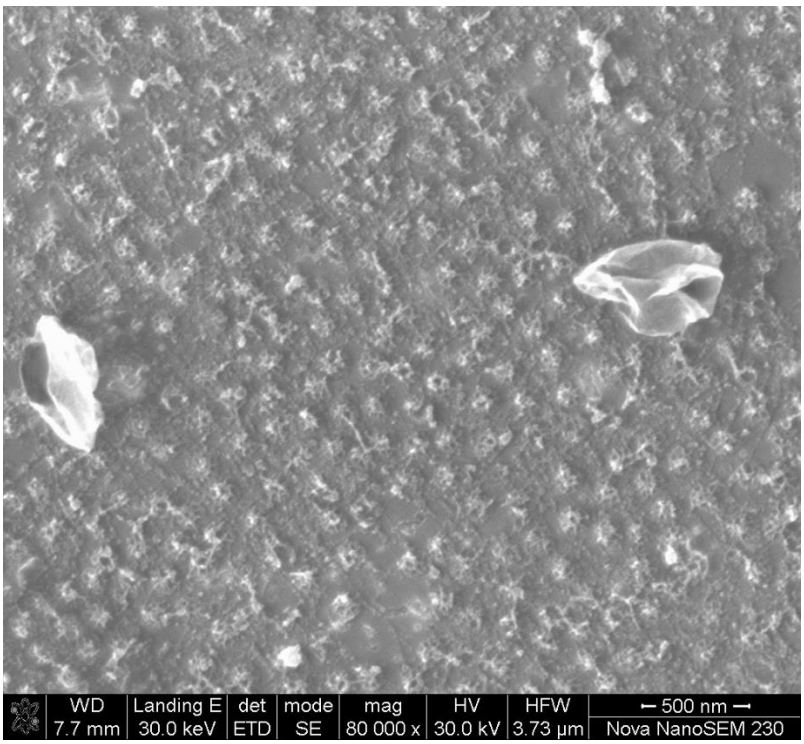

Nucleoplasmic side

Fig 6.1: Negative stained SEM image of spread *X.l.* oocyte NE.

Appendix of Chapter 4

Python code to cut drift in Z axis

```
def z_drift_cut(afm, name):
    n = afm.shape[0]
    one_matrix = np.ones(afm[1].shape)
```

```
    hsafm = []
    for i in range(n):
        minimum = np.min(afm[i])
        afm[i] = afm[i] - np.multiply(minimum, one_matrix)
        hsafm.append(afm[i])
    #print(hsafm)
    #plt.imshow(hsafm[1])
    hsafm_array = np.array(hsafm)
    plt.gcf()
    plt.show()
```

Code to calculate Mean Square Displacement in Z axis

```
import tempfile as TemporaryFile
import tifffile as tf
import matplotlib.pyplot as plt
import numpy as np
from scipy.optimize import least_squares
from scipy.ndimage.filters import median_filter
def compute_msd_center(x, name):
    '''
    Calculate MSD for 1d-array
    '''

    n = x.shape[0]
    xpix = np.around(x.shape[1]/2)
    ypix = np.around(x.shape[2]/2)
    msds = np.zeros(n)
    msdp = []
    for tau in range(1, n):
        diffs = x[tau:, xpix:xpix+3, ypix:ypix+3] - x[:n - tau, xpix:xpix+3, ypix:ypix+3]
        sqdist = np.square(diffs)
        msds[tau] = sqdist.mean()
        #msdp.append(msds[tau])
    plt.show()
```

Code for fitting

```
def msd_fit_center(afm, name):
    msd = np.load(
    msd.shape

    from scipy.optimize import curve_fit
    N = afm.shape[0]
    x = np.linspace(0, N, N)
    n = np.around(afm.shape[0])
    popt, pcov = curve_fit(func, x, msd)
    print('Lz_center',popt)
    fig, ax = plt.subplots(figsize = (12,7.5))
    font = {'family':'normal',
          'weight':'normal',
          'size':22}
    plt.rc('font', **font)
    ax.set(ylabel=r'MSD (nm)', xlabel = 'lag time (frames))')
    plt.suptitle('center')
    plt.plot(x, func(x, *popt),'r-' )
    plt.plot(x, msd, 'b-')
    plt.gcf()
    plt.show()
```

Appendix of outlook

Kapβ diffusion is too fast for HS-AFM to capture therefore Total Internal Reflection Fluorescence Microscopy (TIRFM) was employed. Kapβ were tagged by Alexa647 and their dynamics are observed (highlited by red circle). Experiment set up is same to outlook, 100 pM Kapβ–Alexa647 were used in this experiment. Area imaged is focused on 90 nm above the lipid bilayer. Recorded images showed Kapβ-Alexa647 diffusing on the FGNups brush layer. Surface chamber was thoroughly washed to get rid of unbound Kapβ-Alexa647 to Nsp1 brushes in solution prior to measurements.

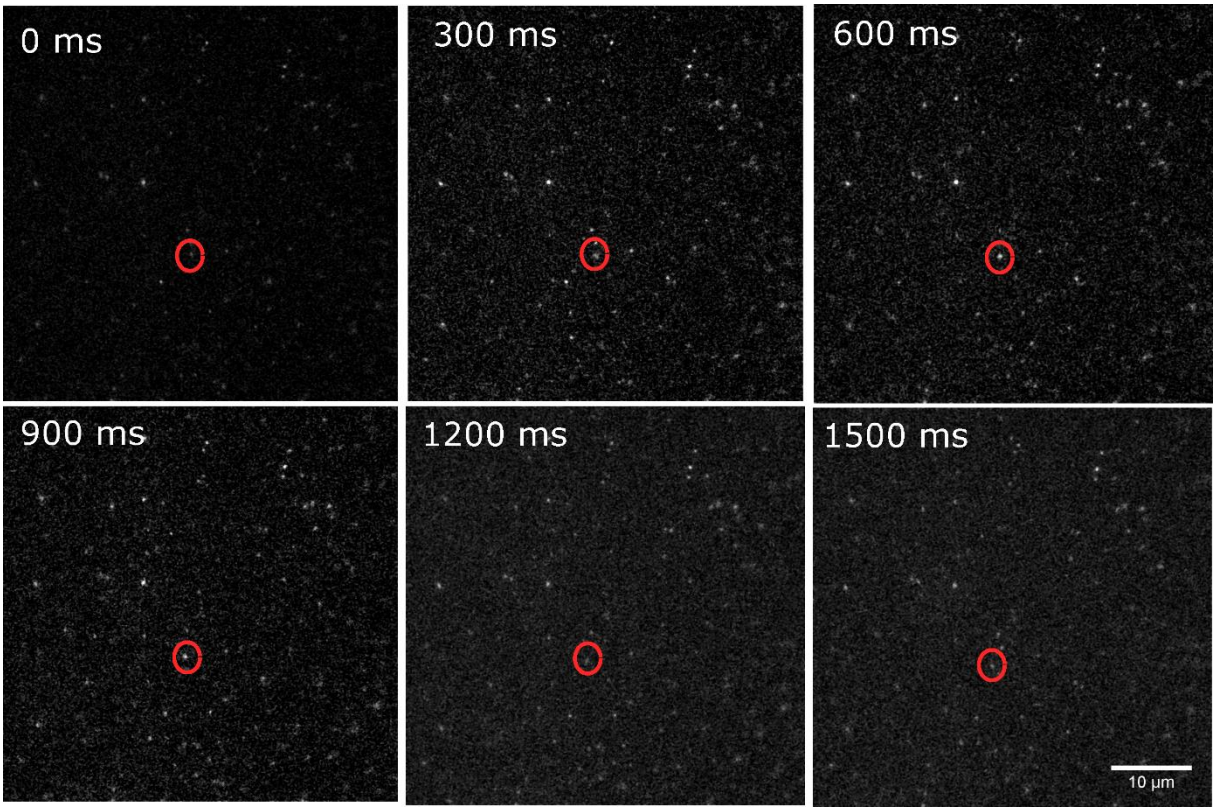

Fig 6.2: Blight spots are Alexa647 tagged Kapβ. Moving spot is highlighted by red circle.

Python code for calculating trajectories and plotting. Open source library Track.py is used for picking up particles.

```
def main(imagenumber, frame_begin, frame_end, condition_n, diameter):
    import sys
    sys.path.append(r
    from asd import readASD
    imagenumber_n = str(imagenumber)
    data = readASD(imagenumber_n +'.asd')
    area = data['x_nm']
    pixel = data['x_size']
    rate = data['framerate_ms']
    scanrate = 1000/data['framerate_ms']
    frame_begin_n = str(frame_begin)
    frame_end_n = str(frame_end)
    frame_end1 = frame_end - 1
    frame_sub =  frame_end1 - frame_begin -1
    frame_sub_n = str(frame_sub)
    import trackpy as tp
    import matplotlib.pyplot as plt
    from scipy.ndimage.filters import median_filter
```

```
f = tp.batch(median_filter(data['frames'][frame_begin:frame_end], 3), diameter, minmass=5, invert = False)
t = tp.link_df(f, diameter, memory = 2)
plt.figure(figsize = (10,10))
tp.plot_traj(t)
#plt.gcf()
#plt.savefig('Nsp1f-s_trajectry.tiff')
plt.show()
#t['x']
d = compute_drift(t)
tm = tp.subtract_drift(t.copy(),d)
plt.figure(figsize = (10,10))
#plt.plot()
tp.plot_traj(tm)
im = tp.imsd(tm, area/pixel, scanrate, max_lagtime = frame_sub)

#im.count()
#im.count()
idx = im.count().idxmin(axis=0)
imct = im.count()
im_drop2=im[idx]
im_drop = im[idx]
im_drop1 = im[idx]
im_drop0 = im[idx]
im_sum=len(imct.index.values)
import pandas as pd
import numpy as np
dvg = 0
cvg = 0
mean = 0
mean1 =0
area1 = 3
area2 = 30
area3 = 100
#im_ind = pd.DataFrame(im.index)
#print(im_ind)
a = pd.DataFrame
for i in imct.index.values.astype(int):
    if area1 < im.count()[i] < area2:
        im_drop = pd.concat([im_drop, im[i]], axis=1)
        mean = mean +1.00
    elif area2 <= im.count()[i] < area3:
        im_drop1 = pd.concat([im_drop1, im[i]], axis=1)
        mean1 = mean1 +1.00
    elif area3 <= im.count()[i]:
        im_drop2 = pd.concat([im_drop2, im[i]], axis=1)
        cvg = cvg +1.00
    else:
        im_drop0 = pd.concat([im_drop0, im[i]], axis=1)
        dvg = dvg +1.00

mean_ratio = np.divide(mean,im_sum)*100
mean1_ratio = np.divide(mean1, im_sum)*100
dvg_ratio = np.divide(dvg, im_sum)*100
cvg_ratio = np.divide(cvg, im_sum)*100

im.to_pickle(imagenumber_n+'_'+condition_n+'_'+frame_begin_n+'-'+frame_end_n+'_all'+'.txt')


im_drop_ave = im_drop.mean(axis=1)
im_drop1_ave = im_drop1.mean(axis=1)
im_drop2_ave = im_drop2.mean(axis=1)
im_drop0_ave = im_drop0.mean(axis=1)
#im_drop2

fig, ax = plt.subplots(figsize = (16, 10))
ax.plot(im_drop0.index, im_drop0, 'k-', alpha = 1)
font = {'family':'normal',
  'weight':'normal',
  'size':22}
plt.rc('font', **font)
ax.set(ylabel=r'$\langle \Delta r^2 \rangle$ [$n$m$^2$]', xlabel = 'lag time $s$')
ax.set_xscale('linear')
ax.set_yscale('linear')
#plt.savefig(condition_n+'_'+frame_sub_n+'_1s')
#np.savetxt('NSP1FF12_Impbeta_impalpha_MSD.txt', im, delimiter =' ')
plt.show()
```

```
    #im = tp.imsd(tm, 1.5/1, 6.67)
    #print(im)
    fig, ax = plt.subplots(figsize = (16, 10))
    ax.plot(im_drop.index, im_drop, 'k-', alpha = 1)
    font = {'family':'normal',
      'weight':'normal',
      'size':22}
    plt.rc('font', **font)
    ax.set(ylabel=r'$\langle \Delta r^2 \rangle$ [$n$m$^2$]', xlabel = 'lag time $s$')
    ax.set_xscale('linear')
    ax.set_yscale('linear')
    #plt.savefig(condition_n+'_'+frame_sub_n+'_7s')
    #np.savetxt('NSP1FF12_Impbeta_impalpha_MSD.txt', im, delimiter =' ')
    plt.show()

    #im = tp.imsd(tm, 1.5/1, 6.67)
    #print(im)
    fig, ax = plt.subplots(figsize = (16, 10))
    ax.plot(im_drop1.index, im_drop1, 'k-', alpha = 1)
    font = {'family':'normal',
      'weight':'normal',
      'size':22}
    plt.rc('font', **font)
    ax.set(ylabel=r'$\langle \Delta r^2 \rangle$ [$n$m$^2$]', xlabel = 'lag time $s$')
    ax.set_xscale('linear')
    ax.set_yscale('linear')
    plt.show()

    #im = tp.imsd(tm, 1.5/1, 6.67)
    fig, ax = plt.subplots(figsize = (16, 10))
    ax.plot(im_drop2.index, im_drop2, 'k-', alpha = 1)
    font = {'family':'normal',
      'weight':'normal',
      'size':22}
    plt.rc('font', **font)
    ax.set(ylabel=r'$\langle \Delta r^2 \rangle$ [$n$m$^2$]', xlabel = 'lag time $s$')
    ax.set_xscale('linear')
    ax.set_yscale('linear')
    plt.show()


    import numpy as np
    y = np.arange(0, 0.15*frame_sub, 0.15)
    x = np.arange(0, 0.15*frame_sub, 0.15)
    x0 = 0
    x1 = area1*rate/1000
    x2 = area2*rate/1000
    x3 = area3*rate/1000
    fig, ax = plt.subplots(figsize = (16, 10))
    ax.plot(im_drop_ave.index, im_drop_ave,im_drop1_ave.index, im_drop1_ave, im_drop2_ave.index, im_drop2_ave,im_drop0_ave.index,
im_drop0_ave,alpha = 1)
    ax.set(ylabel=r'$\langle \Delta r^2 \rangle$ [$n$m$^2$]', xlabel = 'lag time $s$')
    ax.set_xscale('linear')
    ax.set_yscale('linear')

    if im_drop_ave.max(axis=0) > im_drop1_ave.max(axis=0):
        ax.fill_between(x,0,im_drop_ave.max(axis=0),where=x<=x1, facecolor='blue', alpha=0.2,interpolate=False)
        ax.fill_between(x,0,im_drop_ave.max(axis=0),where=x<=x2, facecolor='y', alpha=0.2,interpolate=False)
        ax.fill_between(x,0,im_drop_ave.max(axis=0),where=x<=x3, facecolor='green', alpha=0.2,interpolate=False)
        ax.fill_between(x,0,im_drop_ave.max(axis=0),where=x>=x3, facecolor='red', alpha=0.2,interpolate=False)
    else:
        ax.fill_between(x,0,im_drop1_ave.max(axis=0),where=x<=x1, facecolor='blue', alpha=0.2,interpolate=False)
        ax.fill_between(x,0,im_drop1_ave.max(axis=0),where=x<=x2, facecolor='y', alpha=0.2,interpolate=False)
        ax.fill_between(x,0,im_drop1_ave.max(axis=0),where=x<=x3, facecolor='green', alpha=0.2,interpolate=False)
        ax.fill_between(x,0,im_drop1_ave.max(axis=0),where=x>=x3, facecolor='red', alpha=0.2,interpolate=False)

    #ax.axvspan(x1,x2, color='b',  alpha=0.3)
    plt.show()

    fig, ax = plt.subplots(figsize = (16, 10))
    font = {'family':'normal',
      'weight':'normal',
      'size':22}
    plt.rc('font', **font)
    ax.plot(im.index, im, 'k-', alpha = 0.1)
    ax.set(ylabel=r'$\langle \Delta r^2 \rangle$ [$n$m$^2$]', xlabel = 'lag time $s$')
    ax.set_xscale('linear')
```

```
    ax.set_yscale('linear')
    plt.show()

    labels = 'divergence','mean','mean1','convergence'
    fracs = [dvg_ratio,mean_ratio,mean1_ratio,  cvg_ratio]
    patches, texts, autotexts = plt.pie(fracs, labels=labels,colors=('blue', 'y','green','red'),
                                        autopct='%.0f%%',
                                        shadow=True, radius=1)
    #the_grid = GridSpec(2, 2)
    #plt.subplot()
    #plt.pie(fracs, labels=labels, shadow=True)
    plt.show()
```

Python code for automated protein length measurement: Tilt compensation, threshold, skelton and pixel count are used.

```
import numpy as np

import matplotlib.pyplot as plt

from matplotlib import rcParams
rcParams['figure.figsize'] = (10, 6)
rcParams['legend.fontsize'] = 16
rcParams['axes.labelsize'] = 16

from scipy.optimize import least_squares
from scipy.ndimage.filters import median_filter
from skimage.filters import threshold_otsu
from skimage.morphology import skeletonize
from skimage.morphology import remove_small_objects
data = readASD('201707140011.asd')
def model_fun(p, afm_frame):
    a, b, c = p
    plane = np.zeros(afm_frame.shape)
    for idx, v in np.ndenumerate(afm_frame):
        i, j =idx
        plane[i,j] = a*i + b*j + c
    return plane


p0 = [1,1,1]
test = model_fun(p0, AFMdata)
#plt.imshow(test)

def residuals(p, afm_frame):
    clc_plane = model_fun(p, afm_frame)
    rsd = afm_frame - clc_plane
    return rsd.flatten()
hist = []
for k in range(0,20,1):

    rsd = residuals(p0, data['frames'][k])
    rsd.shape
    fig, axes = plt.subplots(ncols=2, figsize=(15,15))
    ax = axes.ravel()
    p1 = least_squares(residuals, p0, loss = 'soft_l1', args=(data['frames'][k],))
    tilt = model_fun(p1.x, data['frames'][k])
    image = data['frames'][k]
    tilt2 = data['frames'][k] - tilt
    tilt3 = median_filter(tilt2, 3)
    thresh = threshold_otsu(tilt3)
    binary = tilt3 > thresh
    skeleton = skeletonize(binary)
    #contour = perimeter(skeleton) *2
    ax[0].imshow(skeleton)
    #ax[0].set_title(contour)
    ax[1].imshow(image)
    plt.show()
```

List of Publications

1. **Y. Sakiyama**, A. Mazur, L.E. Kapinos, R.Y.H. Lim, *Spatiotemporal dynamics of the nuclear pore complex transport barrier resolved by high-speed atomic force microscopy.* Nature Nanotechnology, 2016. **11**(8): p. 719-23.
2. **Y. Sakiyama**, R. Panatala, R.Y.H Lim, *Structural dynamics of the nuclear pore complex.* Semin Cell Dev Biol, 2017. **68**: p. 27-33.
3. G. Emilsson, K. Xiong, **Y. Sakiyama**, B. Malekian, V. Ahlberg Gagner, R.L. Schoch, R. Y.H. Lim, A. B. Dahlin, *Polymer brushes in solid-state nanopores form an impenetrable entropic barrier for proteins.* Nanoscale, 2018. **10**(10): p. 4663-4669.
4. F. M. C. Benning, **Y. Sakiyama**, A. Mazur, H. S. T. Bukhari, R. Y. H. Lim, T. Maier, *High-Speed Atomic Force Microscopy Visualization of the Dynamics of the Multienzyme Fatty Acid Synthase.* ACS Nano, 2017. **11**(11): p. 10852-10859.